Enhancement of the performances of an electromagnetic device for vibration energy harvesting by nonlinear dynamics and energy localization

Kaouthar AOUALI[1,2,*], Najib KACEM[1], Elyes MRABET[2], Noureddine BOUHADDI[1] and Mohamed HADDAR[2]

[1] *Univ. Bourgogne Franche-Comté, FEMTO-ST Institute, CNRS/UFC/ENSMM/UTBM, Department of Applied Mechanics, 25000 Besançon, France*

[2] *National Engineering School of Sfax, Research Laboratory of Mechanics Modeling and Production, Sfax, Tunisia*

*corresponding author e-mail: aouali.kaouthar@gmail.com

***Abstract*—A nonlinear vibration energy harvester (VEH) based on electromagnetic transduction in a quasi-periodic system is proposed. The quasi-periodic system is obtained by varying the mass of one of the moving magnets which leads to the vibration energy localization. The mechanical nonlinearity is introduced by considering large displacements of the beams. It is shown that the introduction of the nonlinearity and the functionalization of the energy localization phenomenon lead to the enlargement of the bandwidth and the increase of the vibration amplitudes.**

Keywords: ***Vibration energy harvesting, energy localization, nonlinearity, quasi-periodic structure*.**

I. INTRODUCTION

Over the past few years, the diversity of ambient sources of energy arouses researchers to make its scavenging a focus of interest [1]. Therefore, various techniques based on different conversion mechanisms have been developed. Although the evolution in this domain is continuous, most devices operate on a narrow frequency band, which limits their application in areas where energy prevails over a large frequency band [2]. To overcome this problem, several approaches have been proposed such as the introduction of nonlinearities [3] and the energy localization [4], etc.

In this context, a multimodal vibration energy harvester (VEH) is proposed. While focusing on the performances' improvement, introducing nonlinearity by considering large displacements of beams and perturbing the structure by changing mass of one of the moving magnets [5] is investigated. The nonlinearities and the mistuning introduced in the model allow enlarging the bandwidth and increasing the average harvested power.

II. SYSTEM MODELLING

A. Design

The harvester proposed, inspired from the work of Mahmoudi and al [4] and depicted in FIGURE 1, is based on magnetic transduction. It is composed of two weakly coupled magnets guided by elastic beams. The magnetic forces lead to "nonlinear magnetic stiffness". Wire-wound copper coils are wrapped around the moving magnets. When the device is subjected to a harmonic base excitation, each moving magnet oscillates around its equilibrium position and a current is induced in each coil.

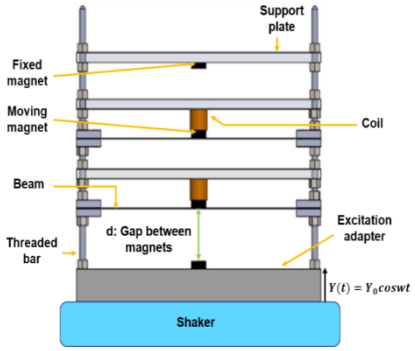

FIGURE 1. DESIGN OF THE PROPOSED VEH

B. Governing equations

In the case of mass mistuning, the system governing the proposed VEH can be expressed as follows:

$$\begin{cases} \ddot{a}_1 + c\,\dot{a}_1 + \omega_0^2[(1+2\beta)a_1 - \beta a_2] + f_{nl}a_1^3 = (1+\gamma)\ddot{Y} \\ \alpha\ddot{a}_2 + c\,\dot{a}_2 + \omega_0^2[(1+2\beta)a_2 - \beta a_1] + f_{nl}a_2^3 = (\alpha+\gamma)\ddot{Y} \end{cases} \quad (1)$$

Where a_1 and a_2 are the generalized coordinates, α is the mass mistuning coefficient, c is the total damping factor, ω_0 is the eigenfrequency of each decoupled dof, m is the equivalent mass, β is the coupling coefficient, k_{mec}^{l} is the linear mechanical stiffness, k_{mec}^{nl} is the nonlinear mechanical stiffness, f_{nl} is the nonlinear term, γ is the mass ratio and $\ddot{Y}$ is the acceleration of the basis excitation.

III. RESULTS AND DISCUSSION

The average power, harvested from the two moving magnets, is expressed as follows:

$$P = R_{load}\left(\frac{\delta\,\omega_0}{R_{load}+R_{int}}\right)^2 [a_{1max}^2 + a_{2max}^2] \quad (2)$$

Where δ is the electromagnetic coefficient and R_{load} and R_{int} are respectively the load and internal resistances of the coil used in the electrical circuit for energy harvesting.

In order to highlight the effects of introducing nonlinearity and energy localization on the performances of the device, we will consider in this study, three distinct configurations. The configuration 1 consists of harvesting energy from the periodic system. The configuration 2 corresponds to a harvested energy from both the perturbed and non-perturbed magnets. As for the third configuration, it consists of harvesting energy from only the perturbed moving magnet. The effect of the introduction of these phenomenons is studied numerically and validated experimentally. We illustrate in the FIGURE 2, the experimental setup used for a sinusoidal excitation.

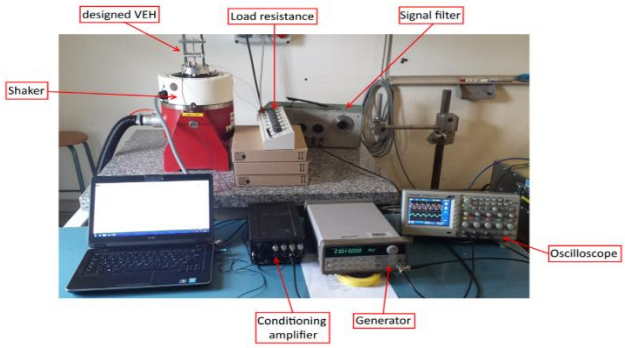

FIGURE 2. TEST BENCH

For the configuration 1, the numerical results and their confrontation are shown in FIGURE 3. Simulations are performed with an acceleration equal to 1 g.

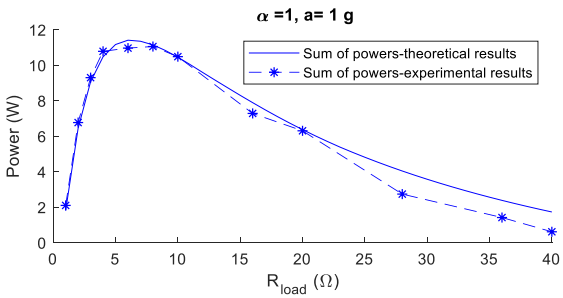

FIGURE 3. RESULTS OF CONFIGURATION 1

In order to study the quasi-periodic system, we should determine the optimal mistuning value, giving the maximum of the harvested power. This mistuning which gives the maximum amplitudes is equal to $\alpha = 1.06$.

The results of the configurations 2 and 3 are illustrated respectively in the FIGURES 4 and 5.

It is show that the harvested power from the configuration 2 is enhanced by 15.87%. Configurations 1 and 3, show that the harvested powers are nearly identical. We can, then, conclude that the introduction of the localization phenomenon offers the opportunity of harvesting energy from one perturbed magnet and having one electric system of harvesting instead of two. Focusing on the effect of the nonlinearity and comparing the results of the best configuration (3) and the configuration 1, we notice from FIGURE 6 that the bandwidth is enhanced by 29%.

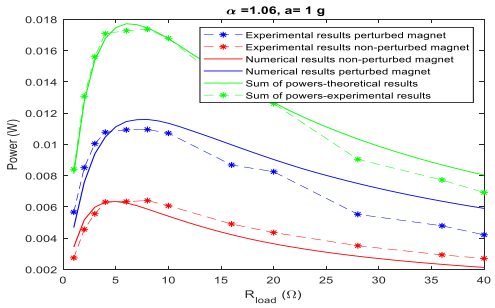

FIGURE 4. RESULTS OF CONFIGURATION 1

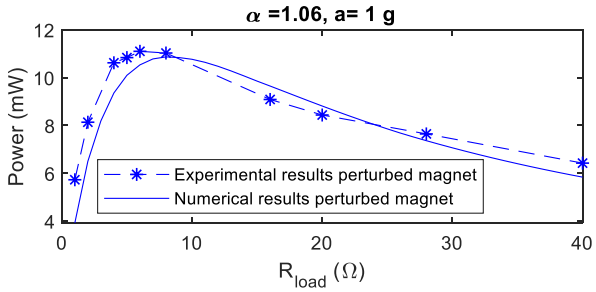

FIGURE 5. RESULTS OF CONFIGURATION 1

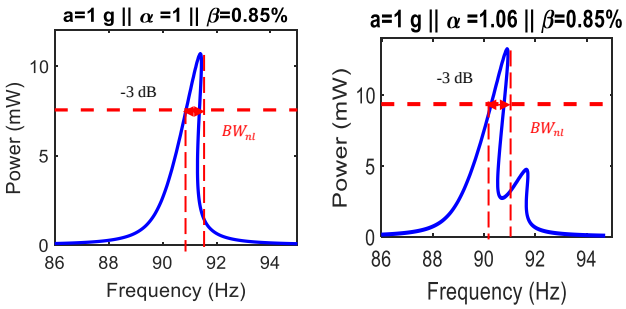

FIGURE 6. BANDWIDTH OF CONFIGURATION 1 (A) AND 3 (B)

IV. CONCLUSION

In this paper, a new concept combining the benefits of dynamic nonlinearities and energy localization is proposed. It has been proved that the mechanical nonlinearity introduced in the periodic system enlarges the bandwidth, while the energy localization by the mass mistuning enhances the average power.

REFERENCES

[1] B. Yang, G. Lee, W. Xiang, J. Xie, J. Han He, Electromagnetic energy harvesting from vibrations of multiple frequencies. *Journal of Micromechanics and Microengineering*, 19(3): 035001, 2009.
[2] B.P. Mann, N.D. Sims, Energy harvesting from the nonlinear oscillations of magnetic levitation, *J. Sound Vib,319, 515530, 2009.*
[3] S. Mahmoudi, N. Kacem and N.Bouhaddi, Enhancement of the performance of a hybrid nonlinear vibration energy harvester based on piezoelectric and electromagnetic transductions, *Smart Materials and Structures, 2014.*
[4] PV. Malaji and S.F. Ali Energy harvesting from near periodic structures, *Vib. Eng. Technol. Mach., 2015.*
[5] Z. Zergoune, N. Kacem and N. Bouhaddi, Vibration energy localization from nonlinear quasi-periodic coupled magnets, *Advances in Acoustics and Vibration II.ICAV 2018.* Applied condition Monitoring vol 13. Springer, Cham.

RF Dickson Voltage Multiplier with Dynamic Back Gate Bias

Mohamad Awad[1,*], Philippe Benech[2] and Jean-Marc Duchamp[2]
[1] Univ. Grenoble Alpes, CNRS,Grenoble INP*, IMEP-LaHC, F-38000 Grenoble
[2] Univ. Grenoble Alpes, CNRS,Grenoble INP*, G2Elab, F-38000 Grenoble
*mohamad.awad@imep.grenoble-inp.fr

***Abstract*—In this paper, a performance comparison of two Dickson voltage multipliers realized with two different technologies: FDSOI 28 nm and BiCMOS 55 nm is presented. The I-V characteristics measurement of diodes in both technologies reveals that FDSOI has a threshold voltage and leakage current smaller than that of BiCMOS. It is also ascertained through the measurement results that the efficiency of the two stages rectifier realized with the FDSOI is better than that of rectifier obtained using BiCMOS. Power conversion efficiency (*PCE*) of 44 % is achieved in FDSOI, whereas, a *PCE* of 37 % is observed in BiCMOS. Furthermore, the effect of increasing the number of stages is presented.**

I. Introduction

The next internet revolution already on the way, will be Internet of Things (IoT) with a large number of wireless micro sensors spread in our environment to monitor our "life" in a more cleverly way (health, security, transportation, energy…) [1-2]. The drawback of IoT is their power requirement: "How supply these without spreading pollution around us due to dispersion of heavy metal in their battery?" Although, thanks to recent improvements in last microelectronic technologies new circuits are now able to consume very low electrical power level. For example, a 32 bits, 50 MHz, ultra-low voltage microcontroller can be powered by only 0.37 V and requires a sleep power around 50 nW [3]. In the same time, average RF power density of Wireless Local Area Network (WLAN) or Global System for Mobile Communications (GSM) can now reach up to 10 nW/cm^2 as shown in [4]. Moreover, in wireless circuit, antenna occupies a large volume of the IoT for a small time of use (less than one minute per day). The idea is to reuse the antenna to harvest the ambient RF energy and relieve the battery. The lifetime of the battery of IoTs could be reinforced.

To convert RF to DC non-linear elements need to be used, usually Schottky diodes, but a sensitivity of -40 dBm at 2.45 GHz has been obtained with tunnel diodes [5]. Howbeit, these types of diodes are still difficult to integrate in microelectronic technologies and circuits. Recently a three stages voltage multiplier, designed in 0.18 µm CMOS technology that can achieve 1 V output voltage for an input power of -27 dBm [6].

In this paper, we compare measured performances of one and two RF-DC converters design with two technologies: one is one of the latest bulk BiCMOS 55 nm technology and the second one is the FDSOI 28 nm described as well adapted to low power applications.

II. Rectifier Principle

RF-DC Dickson voltage multiplier is widely used for RF energy harvesting. Each stage of Dickson rectifier is realized with two diodes and two transistors. This architecture can rectify both part of the signal, negative and positive parts. By increasing the number of stages, the output voltage increases until reaching a limit value where leakage currents and threshold voltages become dominant. A two stage Dickson voltage rectifier is presented in Fig. 1. The power conversion efficiency (*PCE*) is the key parameter and it is defined by:

$$PCE = \frac{V_{Out}^2}{R_{Load}} . \frac{1}{P_{RF,abs}}$$

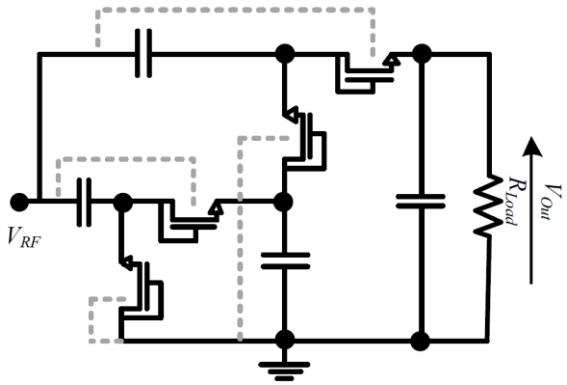

Fig. 1: Two stages Dickson voltage multiplier with dynamic back gate bias.

III. Rectifier Design

To design integrated RF-DC rectifiers, it is necessary to replace Schottky by transistors, configured as a diode (gate connected to the drain). Classical bulk microelectronic as BiCMOS technology is widely used in the integrated circuit. However, it suffers from parasitic and leakage currents in substrate due to the reduction of transistor size. FD-SOI is a promising alternative. In FD-SOI technology, a buried oxide layer (BOX) is placed between the active area and the bulk to reduce leakage currents. Moreover, thanks to the BOX a back gate is obtained which allow to control leakage current and the threshold voltage. One and two-stages rectifiers are realized in

BiCMOS 55 nm and FD-SOI 28 nm technology. The transistors are chosen to reduce losses in the circuit by decreasing series resistance. To reduce the series resistance, transistors with interdigit fingers are used. On the other hand, the (W, L) ratio is conserved for transistors in both technologies.

IV. FDSOI AND BICMOS STATIC COMPARISON

Fig. 2 shows the absolute value of I-V characteristics of the two transistors in both technologies. The simulation and the measurement results are in coherence with each other. The FDSOI transistor has a smaller threshold voltage compared to BiCMOS transistor.

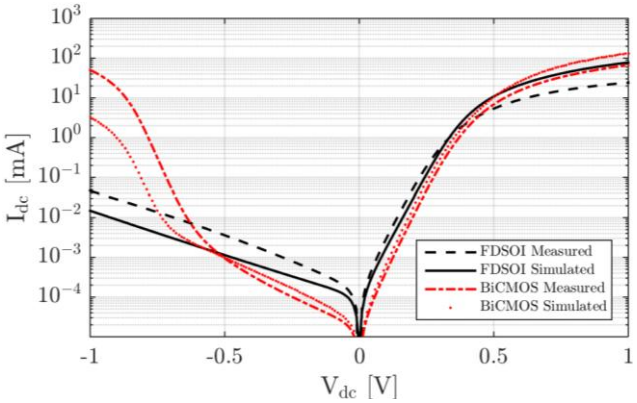

Fig. 1. I-V characteristics in FDSOI and BiCMOS technology for a N-type transistor connected as a diode

Furthermore, for small reverse polarizations (<0.6 V), the leakage currents of BiCMOS are slightly smaller than those of the FDSOI. Nevertheless, beyond this reverse bias voltage, the leakage current of the FDSOI becomes considerably smaller than that of BiCMOS.

V. RECTIFIERS COMPARISON

In this section, a comparison between one and two-stages rectifiers is performed. The transistors used have the same *W/L* for both rectifiers. Figure 3 represents the *PCE* measured for both technologies as a function of the load resistance for same input power (0 dBm). The maximum *PCE* achieved with two stages is 35 % and 28 % with an R_{Load} of 10 kΩ and 7 kΩ for FDSOI and BiCMOS, respectively.

As shown in Figure 5, the maximum *PCE* for two-stage rectifier is obtained for load resistances that are bigger than those of a single stage. This shift is due to the fact that the two-stage voltage converter, can deliver an output voltage bigger than that of one stage, for higher load resistance. In addition, for a single stage, the *PCE* is slightly higher than that of two stages. This degradation is due to the fact that the output voltage is not exactly the double of that of a single stage, because of the voltage drop across the two transistors added for the second stage, and also because of leakage currents. So, by increasing the number of stages, the maximum of the *PCE* cover higher load resistance, but the maximum value of the *PCE* will decrease because of the voltage drop and leakage current.

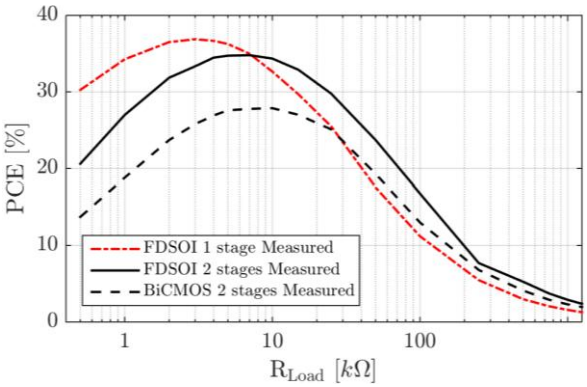

Fig. 2: comparison of the *PCE* vs. R_{Load} for two stages Dickson rectifier designed in FDSOI and BiCMOS technology

VI. CONCLUSION

This paper describes the design of one and two stages of RF rectifiers for energy harvesting. One has been designed in the bulk technology, BiCMOS 55 nm, and the other one SOI technology, FDSOI 28 nm. These rectifiers have been optimized to reduce losses, especially for transistor equivalent series resistance. Static I-V diode measurements represent a lower threshold voltage and less leakage current for FDSOI technology compared to that of BiCMOS. On the other hand, a *PCE* of 35 % is obtained in FDSOI rectifier against a *PCE* of 28 % for BiCMOS rectifier for the same conditions (an input RF power 0 dBm @ 2.45 GHz with an R_{Load} of 10 kΩ and 7 kΩ respectively). Furthermore, by increasing the number of stages of a rectifier, the maximum *PCE* is obtained with higher load resistances, since the output voltage of the rectifier can reach higher values. In addition, FDSOI is an appropriate technology for energy harvesting due to the low threshold voltage, less leakage currents and an appropriate use of the thanks to the Back Gate which can improve the *PCE*.

ACKNOWLEDGMENT

This project has received funding from the European project" ENIAC project Things2DO" and the FLAG-ERA JTC 2016 Convergence. A special acknowledge ST-Microelectronics-France for circuits in BiCMOS 55 nm.

REFERENCES

[1] *J. A. Stankovic, Research directions for the internet of things, IEEE Internet Things J., vol. 1, no. 1, pp. 39, Feb. 2014.*

[2] *L. Da Xu, W. He, and S. Li, Internet of things in industries: A survey, IEEE Trans. Ind. Informat., vol. 10, no. 4, pp. 22332243, Nov. 2014.*

[3] *F. Botman, et al., "Bellevue: A 50MHz variable-width SIMD 32bit microcontroller at 0.37V for processing-intensive wireless sensor nodes," ISCAS, Melbourne VIC, 2014, pp. 1207-1210.*

[4] *H. J. Visser et al, "Ambient RF Energy Scavenging: GSM and WLAN Power Density Measurements," EuMC, Amsterdam, 2008, pp. 721-724*

[5] *C. H. P. Lorenz et al., "Breaking the Efficiency Barrier for Ambient Microwave Power Harvesting With Heterojunction Backward Tunnel Diodes", in IEEE MTT, vol. 63, no. 12, pp. 4544-4555, 2015.*

[6] *M. A. Abouzied et al., "Low-Input Power-Level CMOS RF EnergyHarvesting Front End", in IEEE MTT, vol. 63, no. 11, pp. 3794-3805, 2015.*

[7] *Dickson, J. F. (1976). On-chip high-voltage generation in MNOS integrated circuits using an improved voltage multiplier technique. IEEE Journal of solid-state circuits, 11(3), 374-378.*

Synergistic effects of BaTiO3/MWCNT as fillers on the electrical performance of triboelectric generator based on PDMS composite films

Shan FENG[1], Hanlu ZHANG[1], Delong HE[1]*, Yiguo XU[1], Anne ZHANG[1], Yu LIU[1], Jinbo BAI[1]*

[1] *Laboratoire Mécanique des Sols, Structures et Matériaux (MSSMat), CNRS UMR 8579, Ecole CentraleSupélec, Université Paris-Saclay, 8-10 rue Joliot-Curie, 91190 Gif-sur-Yvette, France*

*Corresponding author E-mail: delong.he@centralesupelec.fr; jinbo.bai@centralesupelec.fr

***Abstract*—The polydimethylsiloxane (PDMS) composite films containing of $BaTiO_3$ particles with average size of 70 nm and 500 nm are prepared and characterized, respectively. Then Triboelectric nanogenerators (TENG) are designed at different $BaTiO_3$ size and mass ratio. In addition, multi-wall carbon nanotubes (MWCNT) are also used for uniform dispersion of $BaTiO_3$ particles in composite films for TENG device. With the synergistic effects of $BaTiO_3$/MWCNT fillers, discrete conductive micro-networks surrounded by $BaTiO_3$ particles form and then the effective filler-matrix interface effect in the three-phase composite is enhanced leading to superior triboelectric output performance. Moreover, triboelectric output performance of TENG changes with different sized $BaTiO_3$ particles. As to BT-70-MWCNT/PDMS composites, with the same mass ratio of BT, the peak output current is always higher than that of BT-500-MWCNT/PDMS.**

I. INTRODUCTION

The increasing energy crisis and environmental pollution stimulate the development of renewable energies, which contribute to reducing the greenhouse effect and the consumption on traditional fossil fuels.[1] As a new type of renewable energy harvesting system, TENG has been proved as an alternative and promising tool to harvest renewable energy in recent years.[2] Due to inherent capacitive characteristic of TENG,[3] it is highly desired to achieve higher output power by increasing the relative capacitance (effective ε/d value, in which ε is the relative permittivity and d is the film thickness). For triboelectric application, more research attention has been given to choosing different types of ceramic or conductive fillers, filler loading and surface structure design, rather than considering the filler-matrix interface effect.[4-6] Thus, it is desired to clarify the effect of filler size and filler-matrix interface on the triboelectric performance of $BaTiO_3$/polymer composite based TENG.

II. EXPERIMENT

Two kinds of tetragonal $BaTiO_3$ nanoparticles (BT NPs) were chosen: 70 nm and 500 nm in average. BT NPs were dispersed in PDMS elastomer. After degassing, the mixture was cast onto a petri dish and cured at 80 □ for 2 h. For BT-MWCNT/PDMS composites, MWCNT with weight ratio of 1 wt% was chosen, using the same process. The film thickness was 300 μm in average. For TENG device, an aluminum foil was prepared as top electrode and positive triboelectric material. The composite film acts as the negative triboelectric material with a bottom electrode. A linear motor system was setup as mechanical source.

III. RESULT AND DISCUSSION

Figure 1 shows the mechanism of a TENG using composite film and Al foil as negative and positive triboelectric materials, respectively. In brief, the TENG works thanks to the coupling effect between triboelectrification and electrostatic induction: i.e., electrification furnishes static polarized charges while the later one converts mechanical energy to electricity during periodic motion.

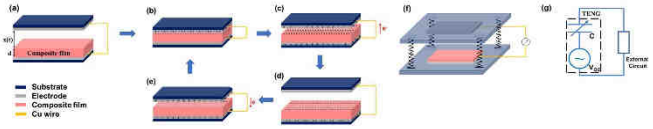

Figure 1(a-e) Mechanism of TENG under an external force; (f) Schematic structure of TENG; (g) Equivalent circuit model.

Figure 1(f) displays the equivalent circuit model of an arbitrary TENG.[7] For contact-mode TENG, the output voltage equation can be written as Eq. (1):

$$V = -\frac{Q}{S\varepsilon_0}\left(\frac{d}{\varepsilon_r} + x\right) + \frac{\sigma x}{\varepsilon_0} \quad (1)$$

where ε_0, ε_r, σ, Q, S, x and d are vacuum permittivity, relative permittivity of the composite film, triboelectric charge density on the film, transferred charges at a certain x, surface area of the film, gap between the composite surface and aluminum, and thickness of the film, respectively. The capacitance between the two electrodes at a certain x(t) for the TENG can be obtained by Eq. (2):

$$C(x) = \frac{\varepsilon_0 S}{x(t) + \frac{d}{\varepsilon_r}} \quad (2)$$

On the basis of this mechanism, output performance increases with the increase of relative permittivity ε_r or with the decrease of the effective thickness of composite film.

Figure 2 shows the V_{oc} (open-circuit voltage) and I_{sc} (short-circuit current) of the TENG using films filled with two different sizes of BT NPs under a periodic compression under frequency of 2.8 Hz. Clearly, both V_{oc} and I_{sc} are enhanced for TENG based on PDMS filled by both sizes of NPs. For TENG with pure PDMS, the I_{sc} and V_{oc} are ~6.9 mA m^{-2} and ~71 V. Output performance is gradually enhanced as wt% of BT NPs

increases to 13 wt% for both samples. At 13 wt%, the I_{sc} and V_{oc} for both sizes of BT NPs are almost the same. However, for BT-500-MWCNTs/PDMS, in Figure 3, the output performance is gradually enhanced as the mass ratio of BT-500 is increased to 20 wt%. As to BT-70-MWCNT/PDMS, with the same mass ratio of BT-70 at 20 wt%, the I_{sc} and V_{oc} are much higher than the values of BT-500-MWCNT/PDMS. Furthermore, the optimum BT mass ratio for BT-70-MWCNT/PDMS is 25 wt%, the corresponding I_{sc} and V_{oc} are 93 mA m^{-2} and 170 V, respectively, and the surface charge density is ~160 uC m^{-2}. It is noted that output signals increase firstly and then decrease as function of the filling content. As mass ratio of BT NPs further increases, I_{sc} and V_{oc} decrease probably for the reason of exposed NPs on the PDMS surface,[4] thus effective contact surface area is decreased for high BT content. From these results, it can be concluded MWCNT enhanced the size effect of BT NPs and showed better synergetic effect with smaller BT NPs on the triboelectric output performance.

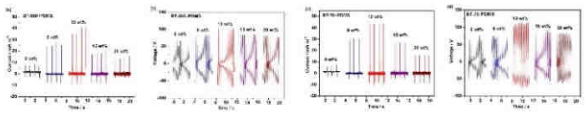

Figure 2 The output current(a, c), voltage(b, d) of TENG using the BT/PDMS.

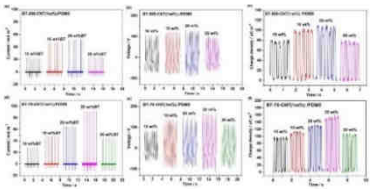

Figure 3 The output current (a, d), voltage (b, e) and charge density (c, f) of TENG using the BT-MWCNT/PDMS.

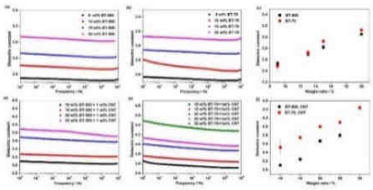

Figure 4 Dielectric constant of the composite films with different filler contents.

The surface area of BT NPs in both sizes increases with BT content. Compared with BT-500, BT-70 changes dramatically leading to much larger surface area. It has been reported that it exists a macroscopic region between the nanoparticle and the matrix, which is different from the fillers and the matrix in character.[8] Smaller particles can afford larger total interfacial region and cause interface overlapping more easily with nearest neighbors, which can significantly enhance the electric displacement D of the composite. Dielectric properties of composites have been investigated. As shown in Figure 4(a-c), dielectric constant of both composites increases with BT NPs. When BT content is lower than 13 wt%, the difference of dielectric constant is not obvious. After adding MWCNT, from Figure 4(d-f), the dielectric constants for both composites are improved. With the same amount of MWCNT, the dielectric constant of BT-70-MWCNT/PDMS is always much larger than that of BT-500-MWCNT /PDMS. This explains why the current density of BT-70-MWCNT/PDMS based device is higher than that of BT-500-MWCNT /PDMS.

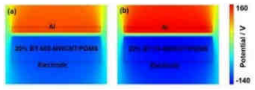

Figure 5 COMSOL simulation.

COMSOL Multiphysics simulation for electrical performance of TENG has also been performed, in Figure 5. Electrical output performance of TENG with optimized BT-70-MWCNT/PDMS has been measured after connecting different resistances. The maximum output power attains 204 µW cm^{-2} under load resistance of 20 MΩ. The output power of TENG was sufficient to light up 60 LEDs when it was connected to a rectifying bridge circuit and 20 MΩ load resistance actuated by slight hand tapping.

IV. Conclusion

In conclusion, the triboelectric output performance of TENG, based on BT-MWCNT/PDMS with two different sizes of BT, was investigated. Results showed that for BT-MWCNT/PDMS, BT size has an influence on the electrical performance of TENG. Composites with smaller size BT contributed to higher interfacial area and larger electric displacement result in better triboelectric output performance of TENG. The optimal output current and voltage were 93 mA m^{-2} and 170 V, respectively, when the mass ratio of BT-70 was 25 wt% (with 1 wt% MWCNT), and the maximum charge density was around 160 µC m^{-2}. The highest output power density was 204 µW cm^{-2} when the load resistance was 20 MΩ.

References

[1] N. L. Panwar, S. C. Kaushik, S. Kothari, "Role of renewable energy sources in environmental protection: A review," Renew. Sust. Energ. Rev., 15, 1513-1524, 2011.

[2] F. R. Fan, Z. Q. Tian, Z. L. Wang, "Flexible triboelectric generator," Nano Energy, 1, 328-334, 2012.

[3] S. Niu, Z. L. Wang, "Theoretical systems of triboelectric nanogenerators," Nano Energy, 14, 161-192, 2015.

[4] J. Chen, H. Guo, X. He, G. Liu, Y. Xi, H. Shi, C. Hu, "Enhancing Performance of Triboelectric Nanogenerator by Filling High Dielectric Nanoparticles into Sponge PDMS Film," ACS Appl. Mater. Inter., 8, 736-744, 2016.

[5] Z. Fang, K. H. Chan, X. Lu, C. F. Tan, G. W. Ho, "Surface texturing and dielectric property tuning toward boosting of triboelectric nanogenerator performance," J. Mater. Chem. A, 6, 52-57, 2018.

[6] X. He, H. Guo, X. Yue, J. Gao, Y. Xi, C. Hu, "Improving energy conversion efficiency for triboelectric nanogenerator with capacitor structure by maximizing surface charge density," Nanoscale, 7, 1896-1903, 2015.

[7] S. Niu, S. Wang, L. Lin, Y. Liu, Y. S. Zhou, Y. Hu, Z. L. Wang, "Theoretical study of contact-mode triboelectric nanogenerators as an effective power source," Energ. Environ. Sci., 6, 3576, 2013.

[8] T. Tanaka, M. Kozako, N. Fuse, Y. Ohki, "Proposal of a multi-core model for polymer nanocomposite dielectrics," IEEE T. Dielect. El. In., 12, 669-681, 2005.

Acoustic power transfer through metal walls : an efficient characterization method based on impedance matrix determination

Olivier FREYCHET*, François FRASSATI, Sébastien BOISSEAU and Ghislain DESPESSE
Univ. Grenoble Alpes, CEA, LETI, MINATEC, F-38000 Grenoble, France
*olivier.freychet@cea.fr

***Abstract* — We present an efficient measurement method, which allows a fast, complete and simple determination of transmitted power across a metal wall using piezoelectric transducers and the evaluation of the power transmission efficiency. Contrary to previously-proposed techniques, using S-parameters, our method exploits the impedance matrix, which is more familiar to the electronic community and is more adequate at our frequencies of interest (around 0.5-2MHz).**

I. INTRODUCTION

Powering sensors behind metal walls without drilling holes to pass wires is of great interests for harsh environments (submarines, aeronautics…) or for tightness issues (food, liquids, fuel tanks). Electromagnetic techniques are ineffective as Faraday shielding occurs. Another solution consists in transmitting energy and data across walls by using ultrasonic waves generated by piezoelectric actuators [2]. Using OFDM techniques some laboratories claim up to 700 Mb/s of throughput [3]. Other research teams [1] have proven that it is possible, with a single piezoelectric disk, to transmit dozens of watts. In this paper, we focus on the energy transfer characterization, to determine power transmission efficiencies and the best frequencies to use to maximize this efficiency.

Originally, the transferred power was characterized by measuring the voltage on an output load connected to the receiving piezoelectric element [5]. This technique is not very efficient as many loads must be tested to find the optimal value. A more efficient technique based on S-parameters determination has been proposed in [1]. This technique allows a full description of the system's variable of interests with only one sweep in frequency.

In this paper, we present an alternative using the impedance matrix, which is more familiar to electronic engineers and more adequate at our frequencies of interest (around 0.5-2MHz).

II. EFFICIENCY AND OUTPUT POWER FOR ANY LOAD

The schematic of the acoustic power transmission (APT) system through metal walls is presented in Figure 1. The impedance matrix describes the electrical variables of interest of this system:

$$\begin{pmatrix} U_1 \\ U_2 \end{pmatrix} = \begin{pmatrix} Z_{11} & Z_{12} \\ Z_{21} & Z_{22} \end{pmatrix} \begin{pmatrix} I_1 \\ I_2 \end{pmatrix} \quad (1)$$

With U_1, U_2 the voltages, I_1, I_2 the currents, and Z_{ij} the terms of the impedance matrix of the APT system. These values are complex and frequency-dependent.

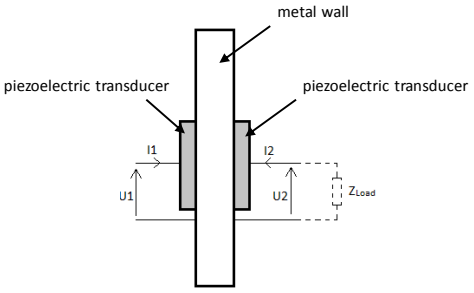

FIGURE 1 : Schematic of the Acoustic Power Transmission (APT) system through a metal wall. The dash impedance is not taken into account in the impedance matrix measurement.

From the impedance matrix, we can determine the transferred power and the transmission efficiency for any output load (Z_{Load}) since:

$$U_2 = -Z_{Load} \times I_2 \quad (2)$$

The minus sign comes from the convention used in FIGURE *1*.

Input and output powers are determined by:

$$P_{in} = Re\left(\frac{U_1 I_1^*}{2}\right) \quad (3)$$

$$P_{out} = Re\left(\frac{-U_2 I_2^*}{2}\right) \quad (4)$$

From equations (1) to (4), input and output powers of the APT system, normalized by the input voltage, can be calculated for any load (Z_{Load}) by:

$$\frac{P_{in}}{|U_1|^2} = \frac{1}{2} Re\left(\left(Z_{11} - \frac{Z_{12} \times Z_{21}}{(Z_{Load} + Z_{22})}\right)^{-1}\right) \quad (5)$$

$$\frac{P_{out}}{|U_1|^2} = \frac{1}{2} Re(Z_{Load}^{-1}) \left| \frac{Z_{21}}{(1 + \frac{Z_{22}}{R})} \times \frac{1}{(Z_{11} - \frac{Z_{12} \times Z_{21}}{(R + Z_{22})})} \right|^2 \quad (6)$$

The power transmission efficiency can be derived from (5) and (6) and is defined as:

$$\eta = \frac{P_{in}}{P_{out}} \tag{7}$$

III. Experimental Validation of the Proposed Characterization Method

The method has been qualified by experimental measurements performed on a squared steel block (300x300x55 mm) with aligned piezoelectric disks (diameter 40 mm, 5 mm thick) on both side (FIGURE 2).

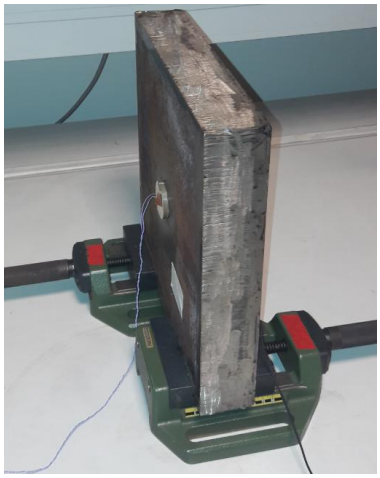

FIGURE 2 : Experimental test bench

In particular, the output power P_{out} computed by our method is compared to the output power obtained by a direct measurement of U_2.

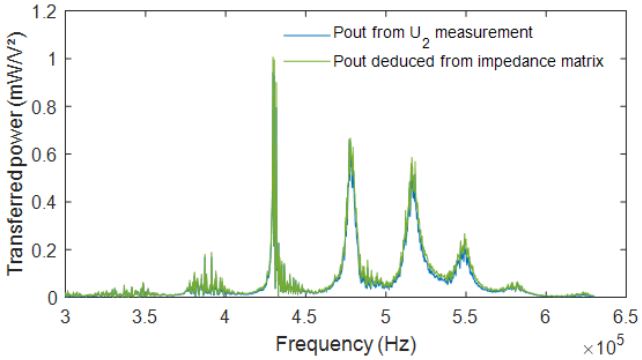

FIGURE 3 : Comparison of output power for a 500 Ω output load.

We can see from *FIGURE 3* that our method with an impedance matrix measurement is equivalent to the direct measurement of the output voltage (U_2).

It is to be noted that one measurement of the impedance matrix over frequency allows to fully-characterize the variables of interests. Using equations (5) to (7), we can calculate the output power and the efficiency for any resistor values and optimize the parameters to optimize the power transmission efficiency. For example, *FIGURE 4* gives the efficiency as a function of the output resistor and the frequency, clearly showing optimums both for the frequency and for the output load.

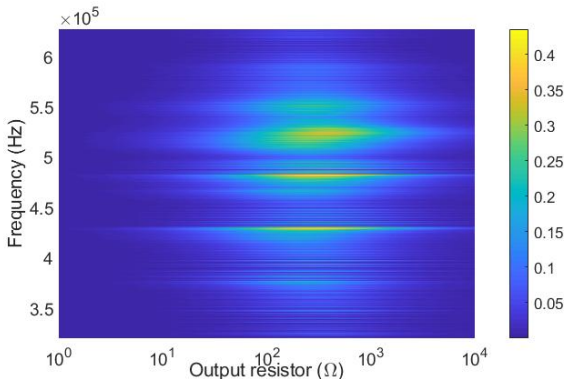

FIGURE 4 : Efficiency of the acoustic power transfer (the colorbar gives the magnitude of the efficiency).

IV. Conclusion

In this paper, a characterization method allowing to get the efficiency and the power transferred through a metal wall using a pair of aligned piezoelectric has been presented. Measurements have shown the validity of this method compared to standard direct measurements.

Research will now be focusing on the analytical determination of optimal transmission frequency and output loads to maximize the power transmission efficiency.

Acknowledgment

This study is part of a PhD Thesis under fundings from the French MoD (Direction Générale de l'Armement). The authors would like to thank AID/DGA for their support.

References

[1] T. J. Lawry *et al.*, « Electrical optimization of power delivery through thick steel barriers using piezoelectric transducers », in *Energy Harvesting and Storage: Materials, Devices, and Applications*, 2010.

[2] J. D. Ashdown *et al.*, « A full-duplex ultrasonic through-wall communication and power delivery system », *IEEE Trans. Ultrason. Ferroelectr. Freq. Control*, 2013.

[3] J. D. Ashdown, L. Liu, G. J. Saulnier, et K. R. Wilt, « High-Rate Ultrasonic Through-Wall Communications Using MIMO-OFDM », *IEEE Trans. Commun.*, 2018.

[4] H. Yang, M. Wu, Z. Yu, et J. Yang, « An Ultrasonic Through-Metal-Wall Power Transfer System with Regulated DC Output », 2018.

[5] X. Bao *et al.*, « High-power piezoelectric acoustic-electric power feedthru for metal walls », in *Industrial and Commercial Applications of Smart Structures Technologies 2008*.

Preparation of 3D electrodes for micro-supercapacitors by spin-coating based on pseudo-faradic materials

Marie GABARD[1-2,*], David CHOUTEAU[3], Virginie GRIMAL[3], Rachelle OMNEE[2], Encarnacion RAYMUNDO-PINERO[2] and Nathalie POIROT[1]

[1] *GREMAN, UMR 7347, CNRS/Université François Rabelais, IUT de Blois, 15 rue de la Chocolaterie, 41000, Blois, France*
[2] *CNRS, CEMHTI UPR3079, Univ. Orléans, 1D avenue de la Recherche Scientfique, 45071, Orléans, France*
[3] *GREMAN, UMR 7347, CNRS/Université François Rabelais, Site STMicroelectronics, 16 rue Pierre et Marie Curie, 37071, Tours, France*

*marie.gabard@cnrs-orleans.fr

***Abstract*—The present study describes a novel strategy for preparing thin Silicon 2D and 3D electrodes for supercapacitors by a spin coating method. A homogeneous solution of TiO_2 was prepared by sol-gel technique and a stable suspension of WO_3 was obtained by dispersing the tungsten chloride in alcohol. This proposed methodology was successfully employed to prepare 2D and 3D with different aspect ratios electrodes. The electrochemical properties of both 2D and 3D materials were evaluated. The 3D TiO_2 and WO_3 electrode show a higher intensity during cyclic voltammograms and a better stability under galvanostatic cycling than the 2D electrode.**

I. INTRODUCTION

With the increasing need of miniaturized energy storage components enabling sustained and autonomous operation of electronic devices for applications such as wearable gadgets or wireless sensor networks, micro-supercapacitors are required. To increase the energy density, which is dependent from the specific surface, new advanced concepts are proposed based on 3D micro-supercapacitors [1]. The present study describes a strategy to prepare 3D electrodes for micro-supercapacitors. The 3D structures, composed of trenches or pillars, were created by Deep Reactive Ionic Etching (DRIE) after photolithography standard processes. Trenches with an opening of 5 µm and a depth of 120 µm having a footprint area of 1 cm^2 can develop 30 cm^2 of useful surface area. In this work, the active materials are metallic oxides such as TiO_2 which has been uniformly deposited over the 3D substrates. To prepare these oxides, in the last few years, synthetic routes as chemical vapor deposition, spray pyrolysis, pulsed laser deposition and radio frequency magnetron sputtering has been reported to control the crystallite size, shape and assembly behavior. Among these techniques, sol-gel synthesis emerged as a promising method as this process is simple, facile and low cost due to the requirement of less equipment. Another advantage of this method is the ability to control the microstructure of the deposited film. Here, we demonstrate also the possibility of using the spin-coating technique to prepare 3D nanotextured electrodes. Conformal thin films coating 3D micro-structured substrates can be obtained as the active materials penetrate inside the 3D structures and uniformly cover the walls [2], [3]. Beyond this, the electrochemical performance of the electrodes has been optimized by controlling microstructure and the thickness of the active layer and by developing substrates with trenches or pillars of high aspect ratio.

II. MATERIALS AND METHODS

A. Preparation of 3D substrate materials

A 150 mm diameter, p-type, (100) silicon wafer (Sil'tronix®, Archamps, France) with a thickness of 600–700 µm was used in our experiments. The standard photolithography technique followed by the deep etching by cryogenic process or by Bosch process are performed.

B. Electrodes preparation and coating procedure

For TiO_2 preparation, the procedure based on Li's work [4] was a sol-gel method. 2.86 mL of tetrabutyl titane (Acros Organics®), 0.86 mL of acetyl acetone (Merck®, purity: 99%) and 1.14 mL of water were mixed. Propanol (solvent, Honeywell®, purity ≥ 99,8 %) was added to obtain 20 mL of sol and to achieve 0.42 M Ti concentration. Two other mixed sols were prepared as below (0.21 M and 0.105 M). These sols were kept under magnetic stirring a few minutes. For WO_3 preparation, tungsten hexachloride precursor (Sigma Aldrich®) was dissolved in methoxyethanol (Prolabo®) to achieve 0.42 M concentration. This dispersion was kept under magnetic stirring for six hours.

The layers were deposited by spin coating method. Each conformal thin film coating on 2D and 3D micro-structured substrate was obtained by following a similar protocol to that described by Vincent *et al.* [2], by adding a polyester resin (PE-NORSODYNE® S 2010 V) to the as-prepared solution with the alcohol solvent in a 4:1 mass ratio. Each resin/dispersion mixture was then deposited on a 2x2cm^2 silicon substrate using a spin coater (SPS-Europe Spin150). This deposition was followed by thermal treatments on hot plates to remove the resin and the solvent. To ensure good electrical contact during the electrochemical characterizations, a Ti layer (200 nm) was deposited by physical vapor deposition (PVD Plassys MP650s) on the backside of the samples. This procedure was repeated several time to obtained 2D and 3D electrodes of different thicknesses.

For electrochemical measurements, half-cells were prepared in an argon-filled glove box within the form of two electrodes Swagelok® type cell. The counter electrodes were lithium foils. These two electrodes were separated with two glass microfiber membranes (Whatman® GF/C) impregnated with 1 mol.L^{-1} lithium hexafluorophosphate ($LiPF_6$) dissolved in a 1:1:3 mixture of ethylene carbonate (EC, Sigma Aldrich®, purity 99%), propylene carbonate (PC, Sigma Aldrich®, purity 99.7%) and dimethyl carbonate (DMC, Sigma Aldrich®, purity >99%) by mass. Electrochemical measurements were made with a Biologic® VMP or solartron. Cyclic voltammograms (CVs) were recorded at a scan rate of 1 mV.s^{-1}. Galvanostatic charge/discharge cycling was performed at different current densities.

III. RESULTS AND DISCUSSION

By increasing the film thickness per coating layer or per varying the solution concentration, the 2D and 3D obtained TiO_2 and WO_3 films composed of small and interconnected nanoparticles have been obtained. The figure 1 show the 3D pillar (of depth 144 µm) and trench (of depth 117 µm) structures after etching. The aspect ratio (AR) was the trench depth divided by the trench width. Based on the formula defined in the literature [5]-[6], the silicon micropillars and microtrenches fabricated allows to reach a high area enlargement factor. As a result, for trenches with an aspect ratio of 29, a footprint area of 1 cm^2 is developed into 34 cm^2 of useful surface area.

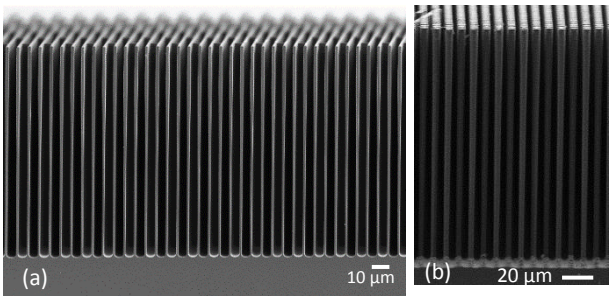

FIGURE 1. SEM image of trench (a) and pillar (b) structures of aspect ratio 29

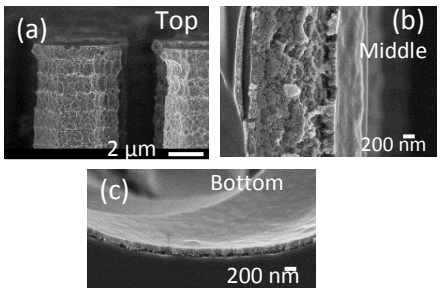

FIGURE 2. SEM images of pillar structures with TiO_2 films

The cross-sectional views after TiO_2 deposition (Figure 2) show that the active materials penetrate inside the 3D structures and uniformly cover the walls. Different locations (figure 2 (a) top, (b) middle and (c) bottom) inside the pillars were inspected at higher magnifications. Conformal thin films coating 3D micro-structured substrates can be obtained. The figure 3 shows CVs of 90 nm TiO_2 deposited on 2D Si and on 3D AR 29 Si µtrenches. We showed the increase of the cathodic peak during CV cycling of the 3D electrode with trenches with an aspect ratio of 29 by a factor of about 31, compared to planar electrode, due to its higher specific surface area (34 cm^2).

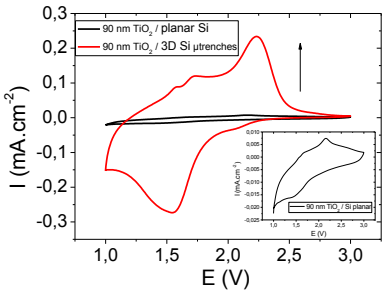

FIGURE 3. Cyclic voltammograms of 90 nm TiO_2 onto 2D Si (in black) and on 3D AR 29 Si µtrenches (in red)

IV. CONCLUSION

A novel approach to deposit TiO_2 and WO_3 layers driven by a liquid route onto a 2D and 3D Si substrate with different aspect ratios has been developed using a spin coating technique. This method was selected mainly because it is relatively easily, fast, and cheap, and in fact could be potentially used in industrial applications. The electrochemical characterization of the 2D and 3D materials as electrodes for supercapacitors proves the positive effect of increasing surface area on the performance.

ACKNOWLEDGMENT

The authors would like to thank Pierre-Yvan Raynal (PPF ASB Tours) for performing SEM observations and Mohamed Boufnichel and Morgane Dutour (STMicroelectronics Tours) for performing the deep etching by Bosch process. The authors are also grateful to the SCAP3D project supported by the Région Centre, France, for its financial support.

REFERENCES

[1] C. Lethien, J. Le Bideau and T. Brousse, « Challenges and prospects of 3D micro-supercapacitors for powering the internet of things », *Energy Environ. Sci.* (2019).

[2] A. Vincent, N. Poirot, « Method of depositing an inorganic material on a substrate, in particular a micron- or submicron- scale textured substrate », International patent No. WO 2015\044582 Al (2015).

[3] M. Gabard, M. Zaghrioui, D. Chouteau, V. Grimal, T. Tillocher, F. Ghamouss, N. Poirot, « Novel Method Based on Spin-Coating for the Preparation of 2D and 3D Si-Based Anodes for Lithium Ion Batteries », ChemEngineering 1(1), 5 (2017).

[4] L. Li, W. Zhu, P. Zhang, Z. Chen, et W. Han, « Photocatalytic oxidation and ozonation of catechol over carbon-black-modified nano-TiO2 thin films supported on Al sheet. », *Water Res.*, vol. 37, n° 15, p. 3646‑3651, sept. 2003.

[5] L. Baggetto, R. A. H. Niessen, F. Roozeboom, et P. H. L. Notten, « High Energy Density All-Solid-State Batteries: A Challenging Concept Towards 3D Integration », *Adv. Funct. Mater.*, vol. 18, n° 7, p. 1057‑1066, 2008.

[6] E. Eustache, P. Tilmant, L. Morgenroth, P. Roussel, G. Patriarche, D. Troadec, N. Rolland, T. Brousse and C. Lethien, « Silicon-Microtube Scaffold Decorated with Anatase TiO2 as a Negative Electrode for a 3D Litium-Ion Microbattery », *Adv. Energy Mater.*, vol. 4, n° 8, juin 2014.

Energy Harvesting for TPMS from an Energy Point of View

Maxim Germer[1,*] and Uwe Marschner[1]
[1] Technical University of Dresden, Chair of Microsystems, Nöthnitzer Str. 64, 01187 Dresden, Germany
*maxim.germer@tu-dresden.de

***Abstract*—This document presents an analysis of the state of the art of energy harvesting systems for tyre pressure monitoring systems (TPMS) from an energy perspective. The work introduces the main energy sources inside a tyre. Then, estimations of the required amount of energy are derived from three different approaches. A comparison between these estimations and the provided energy of the state of the art harvesters reveals a significant better performance of strain-based systems in contrast to widely investigated shock harvesters over a wide range of vehicle velocities. Finally, this paper justifies these characteristics.**

I. Introduction

Since 2008 and 2014 car companies are obliged to integrate tyre pressure monitoring systems (TPMS) in newly registered vehicles in the United States and European Union, respectively. Besides the most important fact of improved safety, the TPMS detects underinflated and overinflated tyres and helps reducing tyre wear and fuel consumption. [1; 2]. More accurate direct TPMS use an energy source to measure and transfer relevant data from the tyre to a receiver unit. Nowadays, button cell batteries are widely spread as energy supply, but due to the high requirements in a car tyre, they are hermetically encapsulated. The method of harvesting energy from ambient sources has demonstrated to be a promising alternative to overcome the detriment of limited battery lifetime and to allow more functionality in today's TPMS. Different ways, transforming a part of the tyre energy into electrical energy, have been investigated, mainly tyre deformations (strain-based harvesters) [3; 4], the change of radial acceleration (shock harvesters) [5; 6; 7; 8; 9; 10] and the change of gravity from +1 g to -1 g [11] are periodically available while driving.

Nevertheless the harsh tyre conditions, namely radial accelerations of a few thousand g, a temperature range from - 40°C to 125°C and more than 25 million cycles during one tyre life affect negatively the development of an energy harvester for TPMS. The majority of investigated harvesters for TPMS uses the change of radial acceleration. In general, those works conclude that the stored energy is enough to send a signal every minute and only if the velocity is higher than 20 or 30 km/h. Only a few tests at velocities of 200 km/h and above were demonstrated, resulting in system destruction. [12]

From an energy point of view and by comparison of experimentally validated TPMS harvesters, this work gives an estimation of the amount of energy to satisfy current TPMS requirements from OEMs supposing an empty energy storage.

II. Energy Estimations

A TPMS has to inform instantaneously the driver about the pressure state, when the vehicle starts rolling. One challenging scenario for energy harvesters is that the tyre pressure has reached a critical state while parking. The TPMS has to send a warning as soon as possible, even if the energy storage is entirely discharged. Therefore, the storage has to be charged to the minimal required voltage of the TPMS. The TPMS needs a current for a certain amount of time (a charge) at a specific voltage, which is supposed to be 1.8 V, the voltage of modern ASICs. For the following energy estimation of a harvester, the authors consider a linear voltage regulator connected between capacitor and ASIC, because it requires few components, surface and it operates passively. The required energy to charge a capacitor with the capacitance C to the voltage V_0 is

$$E_0 = \frac{1}{2} \cdot C \cdot V_0^2 \tag{1}$$

with the required charge Q_{cyc} for one transmission cycle, the total energy E_{tot} equals

$$E_{tot} = \frac{1}{2} \cdot \left(C \cdot V_0^2 + \frac{Q_{cyc}^2}{C} \right). \tag{2}$$

In order to charge the capacitance as quick as possible, the minimal amount of energy has to be calculated as function of the storage capacitance. It suffices to solve the extremum problem $\partial E_{tot}/\partial C = 0$, which results in

$$C_{min} = \frac{Q_{cyc}}{V_0} \tag{3}$$

$$E_{min} = 2 \cdot Q_{cyc} \cdot V_0. \tag{4}$$

FIGURE 1 illustrates the relation between required energy as function of capacitance for different charges, assuming that the minimal voltage V_0 equals 1.8 V. Supposing a required charge of 100 µC, the minimal energy is 360 µJ with an optimal capacitance of 56 µF.

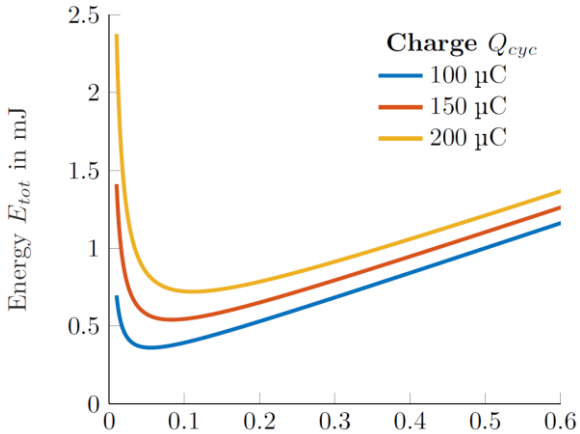

FIGURE 1: Required energy as function of capacitance for different charges and $V_0 = 1.8\ V$

For calculation of the average energy per tyre revolution as function of velocity, two cases are studied: First, the TPMS must have sent the first pressure signal at the latest after a specific time and second, after a specific distance. A third case, taking a battery as initial point ends up in similar results.

A. Time Constraint

Let E_0 be the required amount of energy and T_0 the maximal acceptable transmission period, then the energy per tyre revolution E_{rev} is the quotient of required energy and number of tyre revolutions n, which can be rewritten as function of velocity v

$$E_{rev} = \frac{E_0}{n} = \frac{E_0 \cdot p}{T_0} \cdot \frac{1}{v} \quad , \tag{5}$$

whereas p is the tyre perimeter which supposed to be 2 m. EQUATION (5) indicates, that a velocities increase reduces the requirements on the energy per revolution.

B. Distance Constraint

Let x_0 be the maximal permissible distance in which a signal must have been transmitted after the start, then the energy per revolution E_{rev} can be calculated as

$$E_{rev} = \frac{E_0}{n} = \frac{E_0 \cdot p}{x_0}. \tag{6}$$

Assuming an energy of 360 µJ, the required energy per revolution equals 7.2 µJ and 3.6 µJ for a distance of 100 m and 200 m, respectively.

III. System Comparison

Based on the deduced time and distance constraints, FIGURE 2 illustrates quantified values from past works (coloured dots) in contrast to the constraints (blue lines). For an easier differentiation, the published values are categorised according to their energy source: Red, green and grey represent strain-based, gravitational based and shock energy harvesters, respectively. From this illustration, a significantly better performance of strain-based systems can be concluded. These systems fulfil generally the energy requirements, followed by gravitational valve based harvesters. No presented linear shock energy harvester is able to provide enough energy within the first 100 m. If the constraint is loosened to 200 m, only the systems from Jousimaa et al. and from Keck fulfil the energy requirements. Regarding the weakest constraint (time), there are still two experimentally validated studies which do not achieve this energy boundary. Furthermore, the presented boundaries suppose net energy values. Losses due to rectification and storage are not considered and have to be added. Hence, the required energy is even higher than the boundaries represent. It can be demonstrated that shock energy harvesters, specifically linear mass-spring-damping systems are not made to compensate a quadratically increasing force with a linear spring. In contrast to the increasing radial force, the tyre strain is approximately constant along the entire velocity range. That is why strain-based harvester produces a velocity independent energy per tyre revolution.

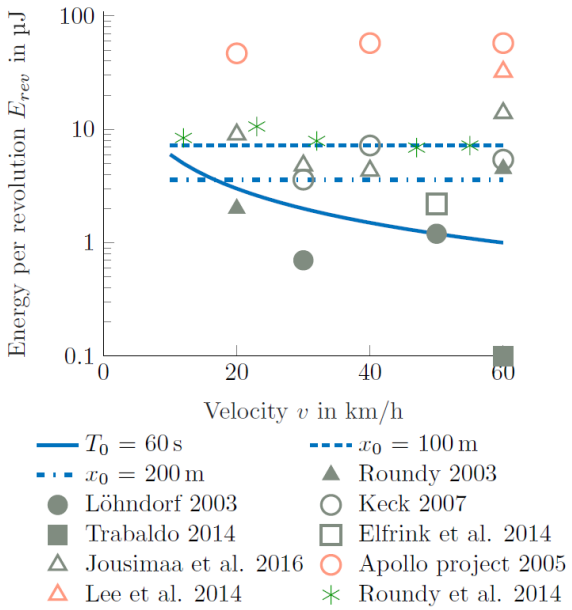

FIGURE 2: Energy per revolution - comparison of different constraints and published experimental works

IV. Conclusion

The presented study evaluated typical energy harvesting systems from an energy point of view. The amount of energy, necessary for TPMS was estimated with two different approaches and further compared with the state of the art of TPMS energy harvesters. As an outlook, this work justified why strain-based harvesters are more promising for a successful industrialisation than other systems.

References

1. Barron, Paul, et al.: Tire Pressure Monitoring Systems Special Study, User's Coding Manual. Techreport, 2011
2. Council of the European Union. Regulation (EC) No 661/2009 of the European Parliament 2009. p. 1-24.
3. *Development of a piezoelectric energy harvesting system for implementing wireless sensors on the tires.* Lee, Jaeyun und Choi, Bumkyoo : Energy Conversion and Management, vol. 78, p. 32-38, 2014.
4. *Intelligent Tyre for Accident-free Traffic (Apollo project).* VTT Technical report IST-2001–34372. Techreport, 2005.
5. Roundy, Shadrach Joseph. *Energy scavenging for wireless sensor nodes with a focus on vibration to electricity conversion.* University of California, Berkeley, Dissertation, p. 129-154,2003.
6. *System modeling of a piezoelectric energy harvesting module for environments with high dynamic forces.* Frey, Alexander, et al., Proceedings of SPIE Smart Sensors, Actuators, and MEMS V, Vol. 8066, p. 80661P, 2011.
7. Löhndorf, M. und Lange, T. MEMS for automotive tire pressure monitoring systems. [Ed.] Michael Kraft und Neil M. White. *MEMS for Automotive and Aerospace Applications.* 2013, p. 54-77.
8. *Energy harvesting system for intelligent tyre sensors.* Jousimaa, Otso J., et al.: IEEE Intelligent Vehicles Symposium (IV), p. 578-583, 2016.
9. *A new approach of a piezoelectric vibration-based power generator to supply next generation tire sensor systems.* Keck, Marian: IEEE Sensors, p. 1299-1302, 2007.
10. *Simulation of a Novel Bridge MEMS-PZT Energy Harvester for Tire Pressure System.* Trabaldo, Edoardo, et al.:Journal of Physics: Conference Series, vol. 557, p. 012041.
11. *An energy harvester for rotating environments using offset pendulum dynamics.* Roundy, S. J. und Tola, J.: Transducers & Eurosensors XXVII, p. 689-692, 2013.
12. *Shock reliability analysis and improvement of MEMS electret-based vibration energy harvesters.* Renaud, M., et al. : Journal of Micromechanics and Microengineering, vol. 25, p. 104010, 2013.

Highly-coupled PZT-based vibration energy harvester for broadband applications

David GIBUS[12*], Pierre GASNIER[1], Adrien MOREL[12] , Sebastien BOISSEAU[1] and Adrien BADEL[2]
[1] *Univ. Grenoble Alpes, CEA, LETI, MINATEC, F-38000 Grenoble, France*
[2] *Univ. Savoie Mont Blanc, SYMME, 74000 Annecy, France*
* david.gibus@cea.fr

***Abstract*— This paper reports on the design and experiment of a highly-coupled piezoelectric energy harvester. Such a device is necessary to benefit from non-linear electrical techniques to improve the frequency bandwidth. A previously developed 2-degree of freedom (2-DOF) analytical model is improved with the Rayleigh method and is used to understand electromechanical interactions and for a preliminary design. As a result, we built a PZT-5A cantilever embedding a long proof mass. The tests demonstrate a strong electromechanical coupling coefficient (k^2=10.2% for the 1st mode), which represents $k^2/k_{31}^2 = 67\%$ of the material coupling.**

I. Introduction

Highly coupled generators are a relevant solution for broadband vibration harvesting. When associated with electrical methods that influence the mechanical resonator dynamics, their harvesting bandwidth can be enlarged thanks to the strong electromechanical coupling of the system [1-2]. Thus, harvesters embedding single crystals have been designed in order to maximize the global coupling. In a previous work [3], we explained the benefits of long proof mass systems to homogenize the strain distribution in the piezoelectric material. We also presented a PMN-PT prototype exhibiting a global electromechanical coupling coefficient $k^2 = 17\%$.

Here, we propose to take benefit of long proof mass systems to design a highly coupled PZT-5A based cantilever. This material is widely used for energy harvesting as it has a high Curie temperature ($T_c° = 360°C$) and a lower cost than single crystal materials [4].

In section II, we present the Rayleigh method applied on the mode shape computed from the 2 degree of freedom (2-DOF) model presented in [3]. A design methodology is described in section III and the modelling, simulations and measurement results are presented and compared in section IV.

II. Analytical model

The studied system is a bimorph piezoelectric cantilever whose electrodes are connected in parallel as shown in FIGURE 1. We firstly neglect the beam mass, as for the 2-DOF model presented in [3]. We consider the proof mass M_t as well as its rotary inertia I_t and the distance D_t of its center of gravity with the end of the bending beam.

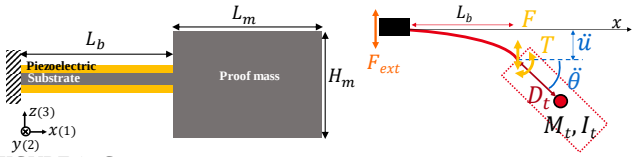

FIGURE 1 : CLAMPED-FREE BEAM SYSTEM ON THE LEFT AND BEAM DURING BENDING ON THE RIGHT

Thereafter, we propose to take the kinetic influence of the beam mass into account thanks to the Rayleigh Method. This method has been extensively detailed for long proof mass systems in [5] where the mode shape were determined with the continuous beam model. By considering energy conversion law, we deduce a single degree of freedom system for each resonant mode:

$$\begin{cases} M_j\ddot{r} + K_j r - \Theta_j v = -B_{f_j}\ddot{w}_B \\ \Theta_j\dot{r} + C_p\dot{v} + i = 0 \end{cases} \quad (1)$$

Where M_j, K_j, Θ_j, B_{f_j} and C_p are the equivalent inertial mass, stiffness, coupling term, forcing vector and clamped capacitance respectively. $\ddot{w}_b$ is the base acceleration, v is the voltage across the electrodes and i is the current flowing through the electrodes. r denotes the displacement at the beam end, while the subscript $j \in [1, N]$ represents the resonant mode of interest.

By considering the mode shapes given by the 2-DOF model, we can analytically express the system coefficients (1) as well as the resonant frequencies and coupling for both first and second flexural resonant modes. This simplifies both the understanding of the electromechanical interactions and the design.

For instance, we can prove that the proof mass density does not affect the global coupling once the proof mass is much heavier than the beam. Only the proof mass shape has an influence on the strain distribution. Furthermore, to increase the first mode electromechanical coupling, it can be shown that the rotary inertia to mass ratio I_t/M_t and the distance D_t should be maximized.

III. Design proposition

The proposed methodology consists in designing a cantilever offering the same expected power as the prototype presented in [3] and the best possible coupling for the first resonant mode. We expect the quality factor to be the same for both systems. The PZT-5A from Noliac company is selected

(Table 1) and we use steel as the substrate and proof mass material.

TABLE 1: MATERIAL COEFFICIENTS FROM NOLIAC NCE51 (PZT-5A)

d_{31}	s_{11}^E	ϵ_{33}^T	k_{31}^2
-208 pm.V^{-1}	17×10^{-12} Pa^{-1}	1900 F.m^{-1}	15.13%

Optimal geometrical parameters have been determined thanks to the proposed 2D model with plane stress assumption and 3D FEM simulations were performed for an accurate estimation of the theoretical electromechanical coefficient. The system has been assembled with epoxy glue (FIGURE 2). The substrate and PZT patches thicknesses are equal to 0.4mm and 0.3mm respectively. We performed admittance measurement to experimentally determine the system parameters (FIGURE 3).

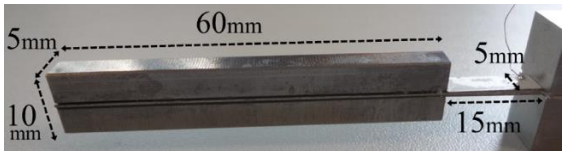

FIGURE 2 : PROTOTYPE WITH PZT-5A

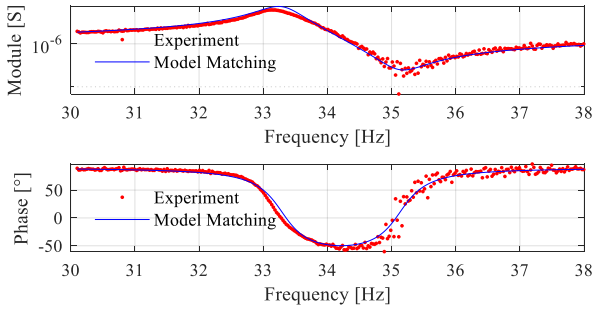

FIGURE 3 : MEASURED ADMITTANCE OF THE PROTOTYPE AND MATCHING WITH THE MODEL PRESENTED IN [1].

IV. DISCUSSIONS

The assembled prototype shows a large electromechanical coupling coefficient ($k^2 = 10.2\%$) which is, as far as we know, the best value obtained for a vibration energy harvester made with PZT-5A material. The quality factor Q_m and the figure of merit $k_e^2 Q_m = k^2 Q_m/(1-k^2)$ are equal to 50 and 5.6 respectively.

We can notice a difference between the simulation and modelling results (Table 2). Since the length-to-width ratio of the beam is equal to 3, neither plane stress nor plane strain assumption are fully respected for our cantilever. Even though experimental results seem close to our 2D analytical model, this cannot prove an exact validation of beam modelling. When we take the imperfectly clamped end and the glue into account in 3D simulations, the resulting global electromechanical coupling coefficient k² decreases. This is explained by losses of elastic energy in non-piezoelectric material. As an example, we reach a coupling of 10.5% if we consider that the piezoelectric patches are at a distance of 50µm from the clamped-end block and the proof mass and if the glue thickness is equal to 5µm (the epoxy Young modulus is estimated to be 4GPa).

On the one hand, the relatively high width-to-length ratio and the clamping end effect on lateral strain artificially increase the coupling between model and simulations. On the other hand, the fabrication process decreases the coupling between simulations and experiment. As a result, a model fitting the experimental data cannot guarantee the model validation and can be explained by a combination of several errors that vanish. The 2D model is however a relevant tool for the design of highly coupled generators. 3D FEM including glue thicknesses and unperfected clamping must be used to have a good performance prediction.

TABLE 2: COUPLING AND RESONANT FREQUENCY OBTAINED WITH THE MODEL, 3D FEM AND EXPERIMENT

	f_{sc}	k^2
Proposed modelling	34.2 Hz	11.8%
3D FEM with perfect clamping	34.8 Hz	14.2%
3D FEM with glue and imperfect clamping	30.8 Hz	10.5%
Experiment	33.3 Hz	10.2%

V. CONCLUSION

In this paper, we propose a design methodology in order to maximize the coupling of linear piezoelectric energy harvesters. The proposed methodology, based on the resolution of a 2DOF model coupled with the Rayleigh method and 3D simulations, is applied to design PZT-5A-based energy harvester. We have been able to obtain experimentally a coupling of 10.2%, which represents $k^2/k_{31}^2 = 67\%$ of the material coupling. Differences between model, simulations and experiment are explained by the influence of the clamped-end imperfections and the glue.

Future work will focus on improving the fabrication and the understanding of the clamping condition influence.

REFERENCES

[1] A. Badel and E. Lefeuvre, "Wideband Piezoelectric Energy Harvester Tuned Through its Electronic Interface Circuit," *J. Phys. Conf. Ser.*, vol. 557, p. 012115, Nov. 2014.

[2] A. Morel, G. Pillonnet, P. Gasnier, E. Lefeuvre, and A. Badel, "Frequency tuning of piezoelectric energy harvesters thanks to a short-circuit synchronous electric charge extraction," *Smart Mater. Struct.*, vol. 28, no. 2, p. 025009, Dec. 2018.

[3] D. Gibus, P. Gasnier, A. Morel, S. Boisseau, and A. Badel, "Modelling and design of highly coupled piezoelectric energy harvesters for broadband applications," *J. Phys. Conf. Ser.*

[4] Z. Yang and J. Zu, "Comparison of PZN-PT, PMN-PT single crystals and PZT ceramic for vibration energy harvesting," *Energy Convers. Manag.*, vol. 122, pp. 321–329, Aug. 2016.

[5] M. Kim, M. Hoegen, J. Dugundji, and B. L. Wardle, "Modeling and experimental verification of proof mass effects on vibration energy harvester performance," *Smart Mater. Struct.*, vol. 19, no. 4, p. 045023, Apr. 2010.

Numerical and experimental study of thinned-bulk piezoelectric harvesters

Thien Hoang[1,2], Maxime Bavencoffe[2], Guillaume Ferin[1], Franck Levassort[2], Claire Bantignies[1], An Nguyen-Dinh[1], Marc Lethiecq[2], Guylaine Poulin-Vittrant[2]

1) *Advanced Research dept., VERMON S.A.,*Tours, France
2) *Université de Tours, INSA Centre Val de Loire, GREMAN, UMR 7347 CNRS,* Blois, France

***Abstract*— Bulk piezoelectric cantilever beam are mostly assembled under serial bimorph topologies where the piezoelectric material is laminated around an inner shim material. The two PZT skins exhibit an individual thickness ranging from few tens to hundreds of micrometers according to the targeted application and its miniaturization requests. Designing such devices become a challenge and one needs FEM (finite element model) to properly define material thicknesses and overall piezoelectric energy harvester geometries. Unfortunately, bulk piezoelectric material are characterized using thicker samples which provide results slightly different of the actual characteristics of thinned-bulk piezoelectric materials. Previous works have addressed an approach to study the thin piezoelectric material layer relying on the electrical admittance analysis. Then, the effective coefficients of thinned-bulk piezoelectric material are identified and entered in a 3D FEM of the PZT layer. The electrical admittance is calculated, showing a good agreement with the experimental measurements.**

I. INTRODUCTION

The two main piezoelectric structures used in vibration energy harvesting are the unimorph, constituted of one piezoelectric layer bonded on an elastic layer, and the bimorph, made of two piezoelectric layers separated with an inner elastic shim material [1]. Thinned-bulk piezoelectric energy harvesters show the capability to address lower frequencies (<200Hz) required for most ambient vibration applications [2-3]. To understand and predict the behavior of such cantilever-based mechanical energy harvesters, numerical models have to be developed and compared to experimental measurements. This objective first requires an accurate set of material properties.

To this aim, an original method has been proposed in a previous work [4], based on the only electrical impedance measurement of the piezoelectric layer in free-free mechanical boundary conditions: the effective values of the electrical, mechanical and piezoelectric tensors are identified using successively a one-dimensional analytical model and a three-dimensional finite element (FE) model of the electrical impedance.

Firstly, the fabrication process of thinned-bulk piezoelectric harvesters is presented. Secondly, the means of numerical and experimental investigation are detailed. Thirdly, the numerical results are compared and discussed with respect to experimental electrical measurements.

II. FABRICATION PROCESS OF PIEZOELECTRIC HARVESTERS

Fig. 1 shows the manufacturing process flow of thinned-bulk piezoelectric energy harvesters. Firstly, a PZT subtrate of 500µm thickness is bonded on a thin brass foil using a conductive epoxy resin at room temperature to shape an unimorph structure, a 2nd PZT layer is bonded to shape a bimorph structure. Secondly, the PZT layers are grinded down and polished to their desired thickness. Then, the sample is metallized with chromium and gold electrodes. Finally, the unimorph/bimorph is cut into its final dimensions.

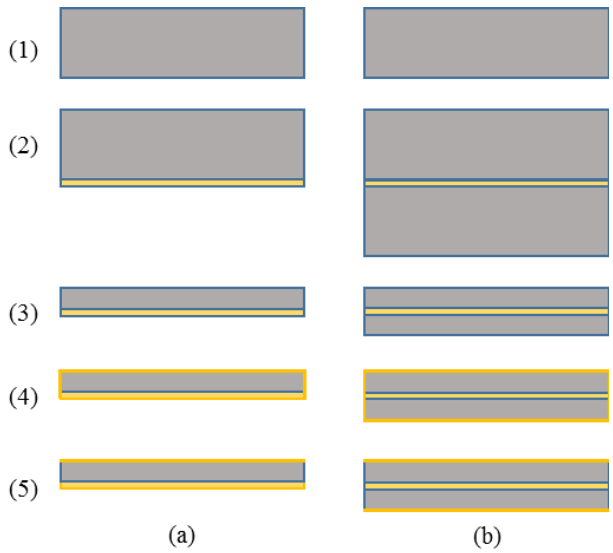

Fig. 1. Fabrication process of bulk piezoelectric energy harvester: (a) unimorph structure, (b) bimorph structure. (1) Flat PZT substrate 0.5mm; (2) Bonding of elastic material layer to form (a) and 2nd PZT layer to form (b); (3) Grinding/polishing of PZT layer; (4) Top & bottom layer plating; (5) Trimming to final dimension.

III. MEANS OF INVESTIGATION

A. Experimental approach

A unimorph of 4mm x 39mm area, 12/150µm brass/PZT layers thickness and a bimorph of 4mm x 39mm area, 150/12/150µm PZT/brass/PZT layers thickness are manufactured using our process flow described previously. The electrical impedance of each sample is measured by using an impedance analyzer HIOKI© IM3570 in the frequency range of 40 kHz – 100 kHz with 0.1V sinusoidal electrical solicitation. The experimental set-up is presented in Fig. 2.

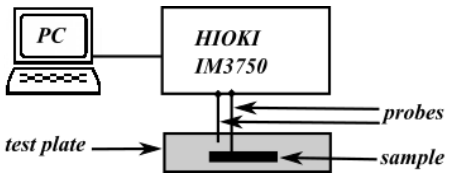

Fig. 2. Scheme of the experimental set-up.

B. Numerical modelling

For each structure, the elastic, dielectric, piezoelectric tensors of thinned PZT layer have been identified (see Table II) using the method developed in [8] with mechanical and dielectric losses taken into account. The material properties of brass foil have been obtained from the manufacturer.

TABLE I. IDENTIFIED MATERIAL PARAMETERS OF THINNED-PZT LAYER

s_{11}^E [m^2/N]	θs_{11}^E	$\varepsilon_{33}^T/\varepsilon_0$	$\theta\varepsilon_{33}^T$	d_{31} [pC/N]
1.14e-11	1.9E-3	1244	4E-3	-124

Then, a numerical study based on the FE method has been carried out with COMSOL Multiphysics® FEA software. The unimorph structure was meshed with 1000 hexahedral elements and the bimorph structure was meshed with 1500 hexahedral elements. It should be noted that the epoxy adhesive layers and the metallized layers are not taken into account in the 3D FE models because their thicknesses are negligible compared to those of PZT layers and shim. A frequency domain study has been then performed to model the electrical response of each structure in free mechanical boundary conditions.

IV. RESULTS AND DISCUSSION

A. Unimorph cantilever beam

Fig. 3 shows the comparison between the FE model and the measurement of the impedance modulus of the unimorph in free-free mechanical boundary conditions. A good agreement is observed between model and experiment. This qualitative assessment is reinforced by a coefficient of determination of 71%. More precisely, the computational model has correctly predicted the electrical impedance modulus with a maximum variation of about 23% in terms of impedance value at the resonance peak. In the same way, less than 1% deviation is observed in terms of resonance and anti-resonance frequencies.

B. Bimorph cantilever beam

Fig. 4 shows the comparison between the FE simulation and the measured value of the impedance modulus of the bimorph in free-free mechanical boundary conditions. The shape of the simulated impedance is relatively similar to the measured one: all the peaks observed on the experimental curve appear in the simulated one. However, the coefficient of determination is quite low: almost 42%. The computational model predicts the electrical impedance with a maximum deviation of about 35% in terms of electrical impedance value at resonance peak. However, less than 2% deviation is observed in terms of resonance frequencies.

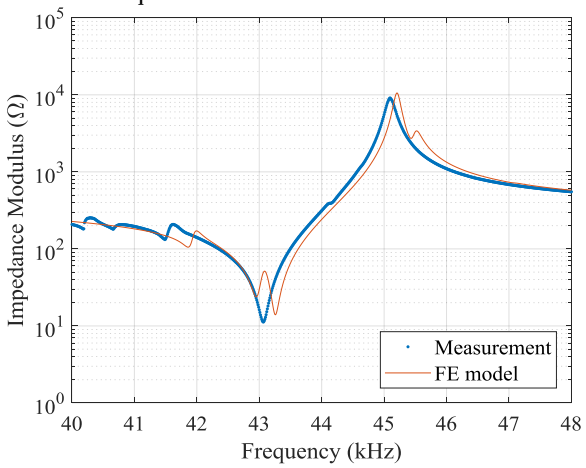

Fig. 3. Impedance modulus versus frequency for the unimorph.

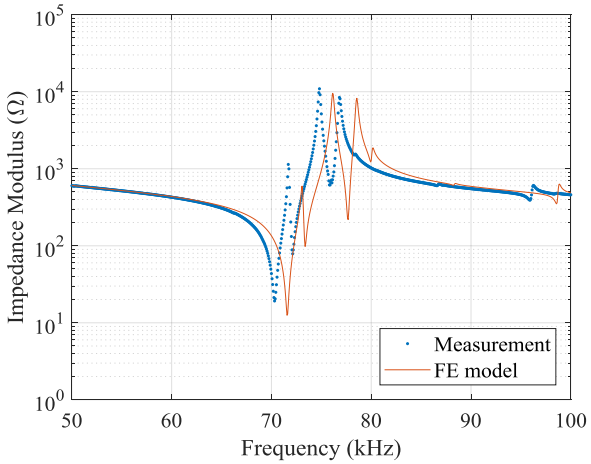

Fig. 4. Impedance modulus versus frequency for the bimorph.

V. CONCLUSION AND FUTURE WORKS

The 3D FE modelling of different energy harvesters was successfully carried out and compared to experimental measurements: the discrepancy between modelling and experiment is less than 2% in frequency. This shows the good accuracy of our modelling tool to predict the electrical behavior of energy harvesters in free-free mechanical boundary conditions. In our work, the goal is to build an efficient 3D FE model for the design of a cantilever-based mechanical energy harvester in vibration. The next steps are to include the clamping fixture in the 3D FE model and to study the response of the harvester when a vibration is applied to the device in order to predict the electrical power delivered by our harvesters.

REFERENCES

[1] H. Li *et al.*, *Appl. Phys. Rev.*, vol. 1, no. 4, p. 41301, 2014.
[2] E. E. Aktakka *et al.*, *IEEE J. Solid-State Circuits*, vol. 49, no. 9, pp. 2017–2029, 2014.
[3] K. A. Cook-Chennault *et al.*, *Smart Mater. Struct.*, vol. 17, no. 4, p. 43001, 2008.
[4] T. Hoang *et al.*, *Adv. Appl. Ceram.*, vol. 0, no. 0, pp. 1–6, 2017.

Works at AS2M department of FEMTO-ST on optimization for piezoelectric energy harvesting

Abbas HOMAYOUNI-AMLASHI*, Thomas SCHLINQUER, Neetu KUMARI,
Abdenbi MOHAND-OUSAID and Micky RAKOTONDRABE
Automatic Control and MicroMechatronic Systems (AS2M) department, FEMTO-ST Institute,
Université Bourgogne Franche-Comté, UFC, ENSMM, UTBM, CNRS
24 Rue Alain Savary, 25000 Besançon - France

*corresponding author e-mail: abbas.homayouni@femto-st.fr

***Abstract*—This paper reviews the activities carried-out on piezoelectric energy harvesting based optimization at the Automatic Control and MicroMechatronic Systems (AS2M) department of FEMTO-ST institute. Seeking for a best compromise between the size and the harvested energy, three main approaches were investigated: parametric optimization, hybrid approach and topology optimization. This paper will highlight the principle of each approach.**

I. INTRODUCTION

The literature exhibits an amount of works regarding piezoelectric energy harvesting topics. These works can be classified into five categories, all of which have the target to provide better performance in terms of output energy, power density, output voltage or ratio between output electrical energy and input mechanical energy. They are: i) materials improvement and new materials synthesis, ii) multilayered piezoelectric harvesters, iii) hybrid harvesters which combine piezoelectric harvesting with other transduction, iv) multi-frequency (or broadband) piezoelectric harvesters, and v) electrical circuits studies. Since few years, a sixth category has been raising in order to complement with the above five categories: optimization of the harvester structure itself. Our works at the AS2M department mainly deal with optimization of piezoelectric energy harvesting systems for various applications, including animal tracking devices powering [1], sensors powering [2]. Whilst the explored optimization itself falls in parametric and topology optimization approaches, though we also study hybrid harvesting technique. This paper presents these past and ongoing works at AS2M regarding piezoelectric energy harvesting.

II. PARAMETRIC OPTIMIZATION

This approach focuses on the optimization of the geometrical parameters of the energy harvesting devices. It is widely used when piezoelectric beams are used to harvest energy. It can be applied to optimize the thickness or the number of layers.

A. Thickness optimization

The energy harvester investigated in [3] is based on layers thickness optimization (see Fig.1). Considering a bilayer unimorph piezoelectric cantilever which is composed of two elements: a passive layer and an active PZT layer. A parametric optimization approach is applied to seek for the optimal ratio between these two thicknesses in order to maximize the output charge at the electrodes. For that, a theoretical model of the device, which links the external excitation to the furnished energy, is derived. Then a gradient-based optimization is carried-out to find the optimal thickness ratio (h_1/h_2) that increases the output charge. As a result, the device transmittance is maximized and it allows producing more charge for a given total thickness. Comparison with existing mechanical piezoelectric harvester structure is made which clearly demonstrates that the proposed structure permits to gain up to five times in terms of the output charge and a significant gain in terms of output electrical power for the same condition. Note that interval techniques [4] are also being used in order to find a set of dimensional parameters (thickness, length, width…) that would provide in a guaranteed way a desired quantity of output charge. For e.g. these interval techniques have been used to find such parameters for actuators which would provide desired resonance frequency and displacement [5].

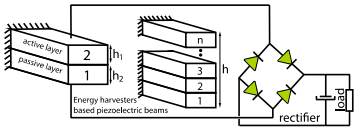

FIGURE 1: Unimorph piezoelectric energy harvester.

B. Layer number optimization

In [6], another energy harvester is investigated (see Fig.1). Unlike the previous one, it studies the effect of number of piezoelectric layers on the output charge. Various conditions were used for the study: fixed total thickness, fixed individual thickness, varying length, varying surface… It comes out that the bimorph structure, i.e. a bilayered cantilever all based on piezoelectric materials, would be the best compromise between output charge and sizes.

III. HYBRID APPROACH

In this work, we study structures that can recuperate energy from ambient vibrations and ambient varying temperature nearby cars engines. Based on piezoelectric materials, one major challenge in this work is when the temperature does not vary anymore and, for instance, stays at high value. To reach the target, we endeavor in studying a structure that can harvest as maximal energy as possible during the temperature

variation through pyroelectric effect, and that could also exhibit sustained vibration when the temperature is constant and high such that piezoelectric effect could still be exploited.

IV. Topology optimization

In topology optimization based piezoelectric energy harvester the goal is to optimize the electrical output of the harvester regarding the mechanical input while respecting constraints on weight, volume and size of the harvester. In this case, we have a design space with predefined boundary condition and loading configuration without any prior knowledge of piezoelectric optimized structure within the design space.

In [7], The algorithm which has been written to optimize the topology of piezoelectric material within the design space, is an extension of 99 line topology optimization MATLAB code written by Sigmund for compliance problems. This code is based on a method called Solid Isotropic Material with Penalization (SIMP) in which design space is discretized by finite number of elements while density of each element is an optimization variable. In SIMP approach, there is a relation between element's density and young's modulus of elasticity of isotropic material. Therefore, optimization algorithm updates the density of each element in each iteration of optimization to find the optimized structure within the designed space to minimize the deflection of the structure due to mechanical force with respect to volume constraint.

The algorithm of Sigmund, solves compliance problem which considers only the mechanical behavior of the system. However, for piezoelectric energy harvesters, electromechanical coupling of piezoelectric material should also be considered in order to optimize the electrical output of the harvester. To do so, first, electrical and mechanical energy of the piezoelectric material due to mechanical input is defined with the help of the piezoelectric constitutive equation. Then, the ratio of the electrical to mechanical energy is defined as objective function to be optimized. Since the piezoelectric materials are not isotropic, SIMP method is modified to relate the density of each element with the piezoelectric stiffness, coupling and dielectric matrices. With the new topology optimization algorithm written for piezoelectric material, it is possible to optimize the structure of piezoelectric energy harvester for different configuration of loads and boundary condition. For example, in Fig.2, the optimized structure under the harmonic force, produced more voltage in comparison to full plate while it has less volume. This is due to the fact that the optimized structure has better strain distribution and displacement in comparison to full plate. Furthermore, the full plate suffers more from charge cancelation due to simultaneous compression and tension in different parts of the plate which is less likely to happen in optimized structure.

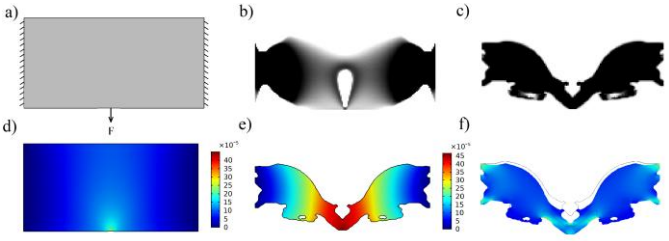

FIGURE 2: a) Design with load and boundary condition b) first iteration of topology optimization c) Finial result of topology optimization d) full plate displacement spectrum e) Optimized structure displacement spectrum f) Strain distribution in optimized structure[7]

The future perspective of topology optimization approach on the piezoelectric energy harvester is to obtain a multi degree of freedom structure that can harvest the energy from different directions.

V. Conclusion

This paper gives the approaches carried out at the AS2M department of FEMTO-ST regarding the piezoelectric enegry harvesting. Principally based on optimization of the harvesting structures, the works can be classified into parametric optimization, hybrid structures, and topology optimization. While they are ongoing, some preliminary results mainly on topology optimization was given.

Acknowledgment

This work has been supported by the national CODE-TRACK project (ANR-17-CE05-0014-01, Control theory tools for optimal design of piezoelectric energy harvesters devoted to birds tracking devices).

References

[1] ANR CODE-Track project: Control theory tools for Optimal Design of piezoelectric Energy harvesters devoted to birds Tracking devices.

[2] European ITN ENHANCE project: Piezoelectric Energy Harvesters for Self-Powered Automotive Sensors: from Advanced Lead-Free Materials to Smart Systems.

[3] Thomas Schlinquer, Abdenbi Mohand-Ousaid and Micky Rakotondrabe, 'Optimal design of a unimorph piezoelectric cantilever devoted to energy harvesting to supply animal tracking devices', IFAC - WC , (World Congress), pp.15165-15170, Toulouse France, July 2017.

[4] Micky Rakotondrabe, 'Performances inclusion for stable interval systems', ACC, (American Control Conference), pp.4367-4372, San Francisco CA USA, June-July 2011.

[5] Sofiane Khadraoui, Micky Rakotondrabe and Philippe Lutz, ' Optimal design of piezoelectric cantilevered actuators with guaranteed performances by using interval techniques', IEEE/ASME Transactions on Mechatronics, Volume 19, Issue 5, Page 1660-1668, October 2014.

[6] Kanty Rabenorosoa and Micky Rakotondrabe, 'Performances analysis of piezoelectric cantilever based energy harvester devoted to mesoscale intra-body robot', SPIE - Sensing Technology+Applications; Sensors for Next Generation Robots conference , 9494-28,, Baltimore Maryland USA, April 2015.

[7] Abbas Homayouni-Amlashi, Abdenbi Mohand-Ousaid and Micky Rakotondrabe, Topology Optimization of Piezoelectric Plate Energy Harvester Under External In-Plan Force Considering Different Boundary Conditions', MARRSS- International Conference on Manipulation Automation and Robotics at Small Scales, (Paper is accepted and is in Press), Helsinki Finland, July 2019.

Design of a Low Power Energy Harvester for RF Wireless Power Transfer Systems at 5.8 GHz

Mariem Kanoun[1,2,*], David Cordeau[1], Jean-Marie Paillot[1], Hassene Mnif[2], Mourad Loulou[2]

[1]CNRS, Univ. Poitiers, XLIM, UMR 7252, F-16000 Angoulême, France
[2] Univ. Sfax, National Engineering School of Sfax, LETI, LR99ES3, 3038, Sfax, Tunisia

* mariem.kanoun@univ-poitiers.fr

***Abstract*— This paper presents the design and implementation of an RF energy harvester system at 5.8 GHz for low power wireless transmission applications. A rectenna is combined to a commercial power management circuit and a load which emulates the behaviour of a sensor. The complete system is experimentally tested and excellent performances are demonstrated. The energy harvester is able to extract 4.62 mJ in 40 s and 192 s for -6 dBm and -10 dBm input power respectively allowing us to power wirelessly low power electronic devices.**

I. INTRODUCTION

Researches in energy harvesting technology to power sensor nodes with a green and a renewable energy from ambient environment sources is in great development due to the need of autonomous sensor networks toward the expansion of the concept of Internet Of Things "IOT" in our human life. However, such power sources like solar, vibration and thermal are not always available and electronic devices can operate in inconvenient conditions where it is impossible to power them directly. WPT "Wireless Power Transfer" is well aware to provide energy for ultra-low power electronic devices and involves the proliferation of WSNs "Wireless Sensor Networks". The harvesting node is then powered through an RF source that spreads energy in a dedicated way to an energy conversion circuit "rectenna". A rectenna "rectifying antenna" captures an RF electromagnetic wave via an antenna and convert it into a DC power by a rectifying circuit. Different kinds of rectennas have been developed for wireless power applications at 2.45 GHz. Recently, research in WPT focuses on the design of RF energy harvester to extract energy from a low power RF dedicated source at high frequencies. In fact, energy beamforming technique focuses on unlicensed 5.8 GHz ISM band due to a smaller component size of antenna and devices. On the other hand, in order to efficiently acquire and manage the output DC voltage generated by the rectenna at low RF input power levels, a Power Management Unit (PMU) is introduced between the rectenna and the sensor. In this context, the aim of this paper is to present the design and measurement results of an RF energy harvester at 5.8 GHz and low input power level.

II. RF WIRELESS POWER TRANSFER SYSTEM

The block diagram of the WPT system is illustrated in Fig. 1. A dedicated RF source focuses the energy toward the sensor node. The RF energy harvester system is based on:

- A rectenna formed by a 5.8 GHz patch antenna and a rectifier designed and optimised at 5.8 GHz and -5 dBm RF input power,
- A commercially PMU BQ25570 from Texas Instrument [1],
- A 700 Ω DC load which emulates the behaviour of the ultra-low power sensor CC2650 from Texas Instrument [2]. The sensor needs at least 1.8 V supply voltage and consumes 2.5 mJ.

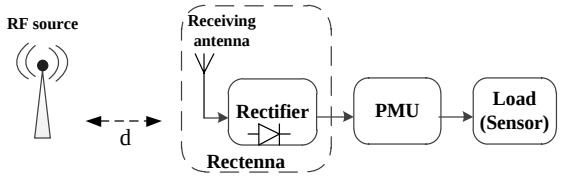

Fig. 1. WPT system building blocks

A. Measurement results of the rectifier combined to a PMU and a load

First, a rectifier circuit with a single series diode is designed and optimised at 5.8 GHz and -5 dBm RF input power in microstrip technology. A design methodology is followed in order to achieve a high conversion efficiency [3]. A HSMS286B commercial Schottky diode is used and the circuit is implemented on a Teflon substrate with a thickness of 0.508 mm and a Dielectric constant of 2.2 (Fig.2). After that, the rectifier circuit is combined with the PMU TI BQ25570 and the load. In this first setup, the receiving antenna is replaced by an RF signal generator, so that the RF harvester is accurately characterized. The PMU is used in order to efficiently extract power from the rectifier and to boost the output DC voltage to the level required by the sensor. The energy is stored in a super capacitor Cbat. As an example, Fig. 3 illustrates the steady state operation waveforms of the PMU at -5 dBm RF input power after overcoming the cold start phase. The output DC voltage V_{out} is set to 1.8 V for a 1 s period of time "T_p" when the capacitor voltage V_{bat} reaches a programmable threshold voltage. For a C_{bat} constant value, the recharge time "T_r" and the average DC output power P_{out} are plotted versus the RF input power in Fig.4. P_{out} is calculated by the following equation:

$$P_{out} = \frac{T_p}{T_p + T_r} P_p \quad (29)$$

Where P_p is the DC power drawn by the load (P_p = 4.62 mW) during the period T_p= 1 s.
As shown in Fig.4, when the received RF input power increases, the average DC output power increases and the recharge time decreases. The efficiency η_G of the complete system "rectifier+ PMU + load" is expressed by:

$$\eta_G = \frac{P_{out}}{P_{in}} \quad (28)$$

Where P_{in} is the RF input power.
The measured efficiency η_G against RF power is plotted in Fig.5. At an input power level of -10 dBm, the efficiency is 24 % and reaches a maximum of 58 % at 2 dBm. The lowest operational input power level of the system is -12 dBm.

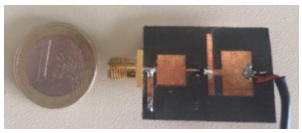

Fig.2. Photograph of the rectifier

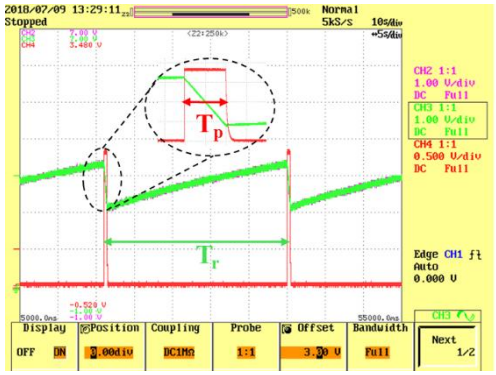

Fig. 3. (V_{out}) "red" and (V_{bat}) "green" waveforms at -5 dBm

B. Complete WPT system Measurement Results

As shown in Fig. 1, the receiving part is formed by a 50 Ω patch antenna, a rectifier, a PMU and a load. The dedicated RF source is formed by a horn antenna presenting a gain of 19 dB and connected to an RF power generator. The Equivalent Isotropically Radiated Power (EIRP) is fixed at 39 dBm. In order to be placed in the far-field region, the patch antenna is kept away at a minimum distance of 1.2 m from the horn antenna. The measured received power is then around -6 dBm at 5.8 GHz. At this input power level, according to Fig. 4, the required recharge time T_r is equal to 40 s in order to recharge the C_{bat} capacitor to 111 µW. The WPT system performances are summarized in Table 1. The RF power sensitivity, referred as the minimum power necessary to enable harvesting, is -12 dBm. This value define the maximum operative distance "d" of the system. In fact, the system is able to maintain a stable output DC voltage while the RF power decreases until -12 dBm and the distance increase to 2.2 m. The DC output voltage is set to 1.8 V during 1 s as the RF input level is varied from -12 dBm to -6.1 dBm with different recharge times.

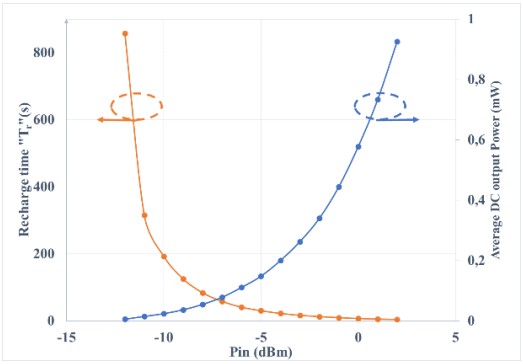

Fig. 4. Average DC output power and recharge time versus RF input power

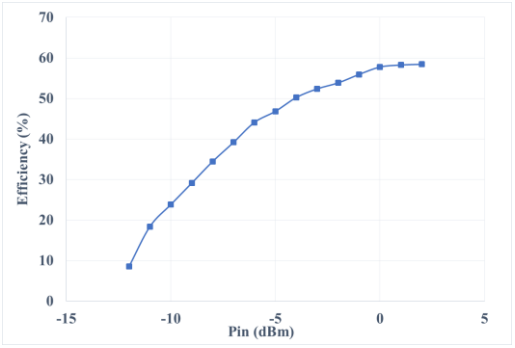

Fig. 5. Global system efficiency versus RF input power

TABLE 1. SUMMARY OF THE WPT SYSTEM PERFORMANCES

Frequency	5.8 GHz
Equivalent Isotropically Radiated Power (EIRP)	39 dBm
Distance transmitter-receiver (d)	1.2 m→2.2 m
RF power received by the rectenna (Pin)	-6.1dBm→-12 dBm
System DC output voltage for a period of 1 s	1.8 V
System average DC output power (Pout)	111 µW→5.4 µW
Recharge time (Tr)	40 s→857 s

III. CONCLUSION

A low power RF harvester system was presented in this paper. It is made of a patch antenna, a single diode rectifier, a commercially available power management circuit TI BQ25570, a 1 mF storage capacitor and a load. The complete system operating at 5.8 GHz was experimentally tested and excellent performances were achieved at an input power level as low as -12 dBm. This means that, for example, 4.62 mW of DC power can be drawn for 1 s every 857 s at a distance of about 2 m from a 39 dBm EIRP source at 5.8 GHz using a 7 dB gain receiving antenna.

REFERENCES

[1] Texas Instruments, bq25570 Nano Power Boost Charger and Buck Converter for Energy Harvester Powered Applications (2018), http://www.ti.com/lit/ds/symlink/bq25570.pdf

[2] Texas Instruments, CC2650 Simple Link Multistandard Wireless MCU (2016), http://www.ti.com/lit/ds/symlink/cc2650.pdf.

[3] M. Kanoun, D. Cordeau, J. M. Paillot, H. Mnif, and M. Loulou, A 5.9 GHz RF rectifier for wireless power transmission applications, Proc. 24th IEEE Int. Conf. on Electronics, Circuits and Systems, 2017, pp. 385-388.

System-level parameter estimation of magnetoelectric transducers for wireless power transfer

Ali KOTEICHE[1,2,*], Alexis BRENES[2], Kevin MALLERON[2] and Gerard SOU[1]

[1] Sorbonne-Université, Univ Paris 06, UR2, L2E Campus Jussieu Ailes 65-66, 1er et 2ème étages 75252 Paris CEDEX 05

[2] ISEP, LISITE, 28 Rue Notre Dame des Champs, 75006 Paris

*ali.koteiche@isep.fr, ali.koteiche@upmc.fr

***Abstract*—This paper presents a system-level electromechanical model of a magnetoelectric transducer for wireless power transfer. Based on a single-degree-of-freedom (SDOF) model, we estimate the equivalent parameters of a lumped-mass model. Impedance measurements at several actuation levels allow us to quantify the evolution of the main parameters of interest and the figure of merit (FOM) for the future optimization of the electrical interface between the transducer and the circuit to supply.**

Keywords: magnetoelectric transducers, wireless power transfer, single-degree-of-freedom model (SDOF), admittance measurements.

I. INTRODUCTION

Magnetoelectric (ME) transducers have proven to be a good candidate to power an embedded biomedical device wirelessly [1,2]. These composite materials use a magnetostrictive (MS) layer - to transform a magnetic energy into a mechanical motion – bonded to a piezoelectric layer, which create the electric energy. An optimization of the electrical interface between the transducer and the load (either an electrical circuit or a battery) is then required. Though very useful when optimizing the ME transducer itself, elaborate finite-element models [3] are hard to use when trying to optimize the power transfer from an electromagnetic source to an electrical load because of their computational complexity. For that reason, very few works have studied how realistic electrical interfaces [4,5,6] affect the power transfer of ME transducers. To that purpose, system-level models are required.

In this paper, we focus on the system-level electromechanical parameters of a ME transducer in the absence of an electromagnetic field. We show how the addition of a MS layer to a piezoelectric resonator modifies the quality factor and the coupling coefficient of the generator and, all in all, the figure-of-merit that one must optimize to design the power transfer interface.

II. MODEL OF AN ELECTROMECHANICAL TRANSDUCER

Even though piezoelectric elements sometimes exhibit nonlinear behaviors [7], they are usually modelled as a coupled single-degree-of-freedom mechanical resonator, when operated at low levels close to one of their resonance frequencies. Such a model (see Figure 1) is made of an effective mass M suspended by a spring of stiffness K. The factor α (N.V^{-1}) accounts for the bidirectional coupling between the mechanical and the electrical domains. The capacitor C_p represents the capacitance of the piezoelectric element. The damper c models the mechanical losses of the system.

In the absence of a magnetic field, we assume that the model of a single-degree electromechanical resonator (Figure 1) remains valid when the MS layer is bonded to the piezoelectric element.

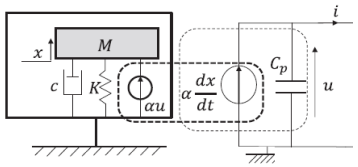

FIGURE 1. ELECTROMECHANICAL MODEL OF A LINEAR ELECTROMECHANICAL RESONATOR.

The MS layer is supposed to modify the equivalent coefficients M, K, c, α and C_p. The validity of this assumption will be verified in section III. The equations governing the systems behavior are the following:

$$\begin{cases} M\dfrac{d^2x}{dt^2} + c\dfrac{dx}{dt} + Kx + \alpha u = 0 \\ i = \alpha\dfrac{dx}{dt} - C_p\dfrac{du}{dt} \end{cases} \quad (1)$$

For the study, we also define the quality factor $Q = M\omega_0/c$ and the modified electromechanical coupling coefficient $k_m^2 = \alpha^2/KC_p$. The natural (short-circuit) angular frequency is written $\omega_0 = \sqrt{K/M}$. Based on this model, a parameter identification procedure can be performed.

III. EXPERIMENTAL VALIDATION OF THE MODEL

A. Experimental setup

Our first sample is composed of a 7mm-width PZT-5H piezoelectric plate which is put into oscillation in the in-plane direction by applying a voltage with an impedance analyzer. A frequency sweep is performed close to its resonance frequency. Similar measurements are then performed on the same sample after gluing a MS layer (Terfenol-D) with insulating epoxy glue. A picture of the composite transducer obtained after the bonding process is reported in Figure 2. In the following paragraphs, the piezoelectric sample will be denoted “P” and “P-T” will be the magnetoelectric composite obtained with the Terfenol D.

The measurements were taken using a sample holder prototype fabricated with a 3D printer (see Figure 3). Apart from the electrical contacts, the whole holder prototype is made of plastic to avoid the use of electromagnetic-sensitive materials for future applications in medical implants. All the measurements were taken with an HP 4194A impedance analyzer.

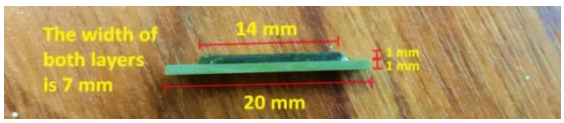

FIGURE 2. P-T SAMPLE: MAGNETOELECTRIC COMPOSITE TRANSDUCER (LIGHT GREEN : PIEZOELECTRIC LAYER - DARCK: MAGNETOSTRICTIVE LAYER)

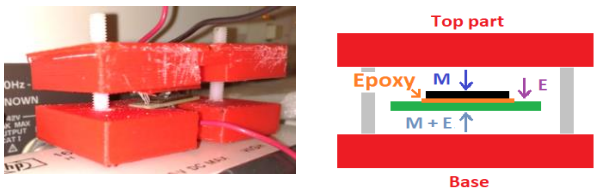

FIGURE 3. THE SAMPLE HOLDER (LEFT: PICTURE, RIGHT: SCHEMATIC) "M" DENOTES A MECHANICAL CONTACT AND "E" AN ELECTRICAL CONTACT.

B. *Experimental results*

1) Model validation

Admittance curves measured on the "P sample" and "P-T sample" are reported in Figure 4. For both samples, the linear SDOF model fits very well with the measurements, for each actuation level.

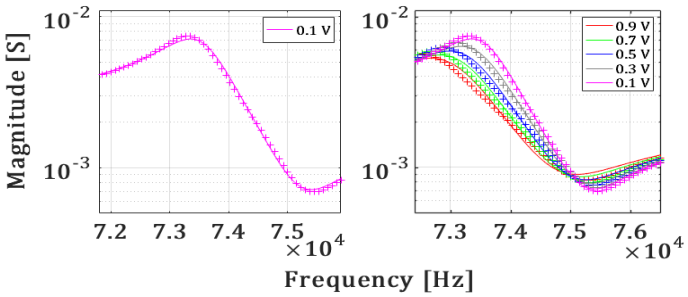

FIGURE 2. ADMITTANCE MEASUREMENTS AND FIT FOR THE "P SAMPLE" (LEFT) AND "P-T SAMPLE"(RIGHT) FOR DIFFERENT ACTUATION LEVELS.

2) Equivalent electromecanical parameters

Based on the admittance measurements of section B.1, we report, in Figure 5, the parameters obtained at different actuation voltages. As one can expect from a linear model, all the parameters estimated on the P-sample are constant. On the contrary, significant variations of the estimated parameters are observed on the P-T sample. The addition of a MS layer strongly impacts the electromechanical behavior. The results show clearly that, on the P-T sample, all the parameters are function of the voltage level. In particular, the quality factor of the P-T sample decreases by around 50% between 0.1V and 1V.

One of the most important characteristic when trying to optimize a power transfer system is the figure-of-merit (FOM) $k_m^2 Q$ (see Figure 6). Due to the sharp decrease of the quality factor, the FOM of the P-T composite also decreases strongly (28%).

IV. CONCLUSION

In this paper, we have estimated system-level parameters of a ME transducer for wireless power transfer. Contrary to the piezoelectric element alone, we have shown that the coupling coefficient and the quality factor of the composite strongly depend on the voltage. In particular, the quality factor of the composite decreases sharply with the voltage level (more than 50% between 0.1V and 1V) which has a strong consequence of the figure-of-merit $k_m^2 Q$.

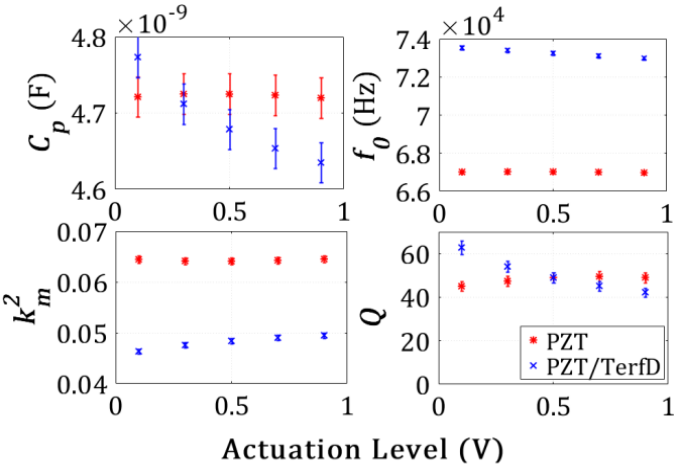

FIGURE 3. PARAMETERS ESTIMATED FROM THE ELECTROMECHANICAL MODEL

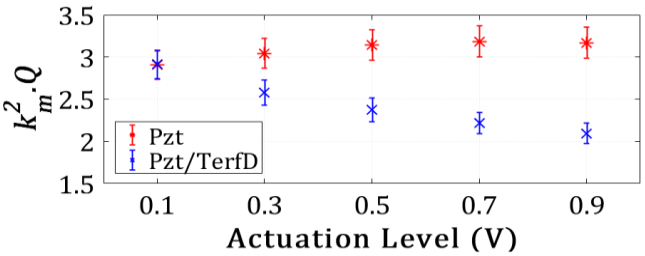

FIGURE 4. EVOLUTION OF THE FOM.

The origin of such a variation is still unsure but it may be related to losses such as eddy currents in the MS layer. System-level conclusions can readily be used for the design of an optimized electrical interface for power transfer. Further work will aim at quantifying the impact of adding an electromagnetic field on the overall behavior.

REFERENCES

[1] T. Rupp, BD. Truong, S. Williams, S. Roundy, Materials (Basel). 2019;12(3):512, 2019.

[2] K. Malleron, A. Gensbittel, H. Talleb and Z.Ren, Microelectronics Journal, 2018, , ISSN 0026-2692.

[3] H. Talleb, Z. Ren, IEEE Transactions on Magnetics, 2015, 51(3), 1-5.

[4] A. Badel and E. Lefeuvre, Nonlinearity in Energy Harvesting Systems, E. Blokhina, A. E. Aroudi, E. Alarcon and D. Galayko, Eds., Cham, Springer, 2016, pp. 353-357.

[5] Y. C. Shu and I. C. Lien, Smart Materials and Structures, vol. 15, pp. 1499-1512, 2006.

[6] H. A. Sodano, D. J. Inman and G. Park, Shock and Vibration Digest, vol. 36, no. 3, pp. 197-206, 2004.

[7] D. A. Hall, Journal of Material Science, vol. 36, no. 19, p. 4575–4601, October 2001.

A self-powered integrated solution for frequency tuning of piezoelectric energy harvesters

Adrien MOREL1[1,2*], Anthony QUELEN2[1], David GIBUS3[1,2], Gaël Pillonnet4[1] and Adrien BADEL5[2]
[1] Univ. Grenoble Alpes, CEA, LETI, MINATEC, F-38000 Grenoble, France
[2] Univ. Savoie Mont Blanc, SYMME, F-74000 Annecy, France
*adrien.morel@cea.fr

***Abstract*—This paper presents the integrated design of a tunable interface for wideband energy harvesting, the Short-Circuit Synchronous Electric Charges Extraction (SC-SECE). By tuning both the phase of the energy harvesting event, ϕ_S, and the angular duration of the short-circuit phase, $\Delta\phi$, this interface maximizes both the harvested energy while tuning the dynamics of the energy harvester. The proposed ASIC is self-powered, includes a cold start, and only consumes less than $1\mu W$, which is a very small percentage of the harvested energy. It includes as well a low-power ($24nW$) gradient algorithm which controls the value of ($\phi_S, \Delta\phi$) and tries to maximizes the harvested power for any vibration's frequency and amplitude.**

I. Introduction

Wireless sensor nodes designed to ensure risk prevention and monitoring are more and more present in our day-to-day life. Most of these sensors only require a small amount of energy to sense, process and send data. This makes energy scavenging a good alternative to batteries, as it may lead to systems combining long lifetime, robustness, and compactness. In closed and confined environments, where the thermal gradients and solar radiations are weak, the major energy source can be found under the form of mechanical vibrations.

Among electromechanical transducers, piezoelectric materials are of interest because of their good trade-off between power density and technological maturity. In order to amplify the mechanical strain applied on such materials, they are usually deposited on a linear mechanical oscillator having high quality factor. The main drawback of such structure is the drastic decrease of power when there is a slight mismatch between the vibration frequency and the harvester resonant frequency. Mismatches may be caused by several reasons such as inaccuracy in the harvester fabrication leading to a shift of the resonant frequencies, aging of the mechanical oscillator, change in the ambient vibration spectrum, among others. In order to face this challenge, some electrical strategies have been proposed in order to electrically tune the dynamics of a highly coupled energy harvester [1-2]. Among them, it has been shown that the Short-Circuit Synchronous Electrical Charge Extraction (SC-SECE) interface allows to drastically enlarge the energy bandwidth while maximizing the harvested power [2]. However, a self-powered implementation of the SC-SECE has yet to be designed.

In this paper, we propose an integrated ASIC implementing the SC-SECE in $0.6\mu m$ XFAB. The proposed design is self-powered, includes a cold-start system, and is able to tune the harvester dynamics in order to work at resonance on a relatively large frequency band.

II. Proposed integrated system

The proposed integrated circuit implements the SC-SECE strategy, a non-linear extraction technique that alternates energy harvesting times and short-circuits times. Two tunable parameters are used: $\phi_S \in [0, \pi]$ and $\Delta\phi \in [0, \pi]$. As depicted in Figure 1, ϕ_S represents the angle between the mechanical displacement extremum and the energy harvesting event, and $\Delta\phi$ represents the angular duration of the short-circuit. These two parameters allow to electrically tune the resonant frequency of the harvester as well as its damping [2]. The system power path is shown in Figure 2, and the MOS are controlled in order to obtain the SC-SECE waveforms shown in Fig.1. A detailed sequencing of the proposed interface is given in [3], in the standard SECE case ($\phi_S = \pi$ and $\Delta\phi = 0$).

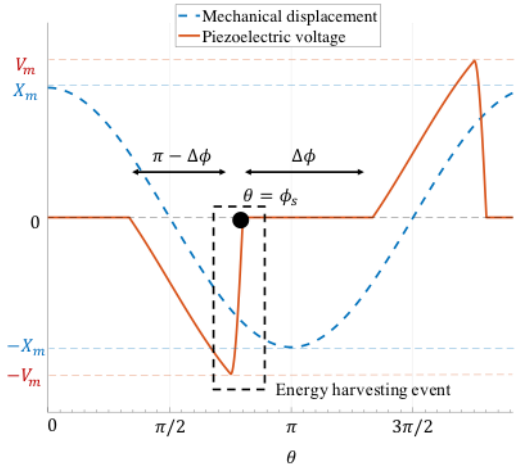

FIGURE 1. Mechanical displacement and piezoelectric voltage waveforms of the SC-SECE [3]

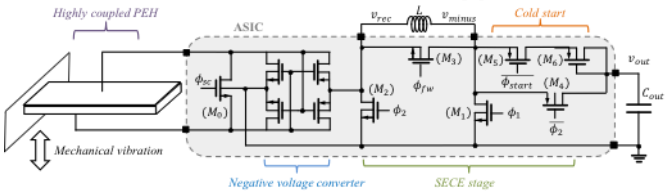

FIGURE 2. Power path of the proposed SC-SECE interface

III. IMPLEMENTATION AND INTEGRATION CHALLENGES

A. Consumption of the self-powered interface

In order to control the various power MOS shown in Fig. 2, many analog senses and a low-power MPPT algorithm have been designed. The main constraint we had, while designing these circuits, was their energy consumption which should not be greater than a small percent of the harvested energy. Figure 3 shows the main analog and digital functions of the control interface, as well as their respective energy consumptions. The total power consumption of the senses does not exceed $1\mu W$, which is much smaller than the harvested energy in most case $(100\mu W - 1mW)$.

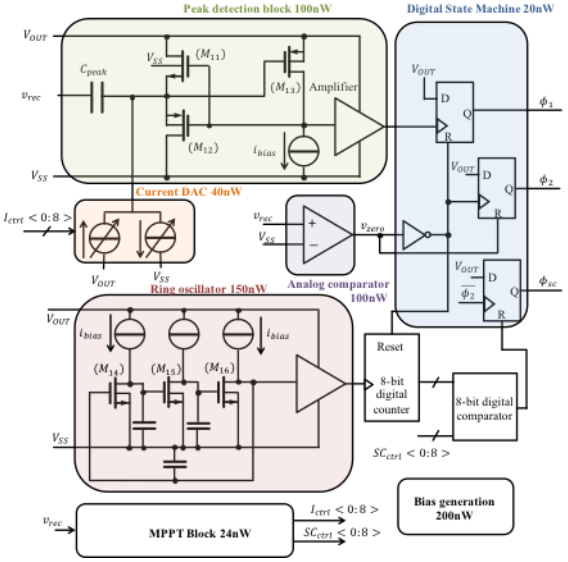

FIGURE 3. SIMPLIFIED VIEW OF VARIOUS ANALOG SENSES

The MPPT algorithm itself does not consume much power $(24nW)$, and proves that designing a self-powered algorithm is feasible and not a major constrain.

B. Losses in the harvesting interface

The other losses in the interface are not linked with the senses shown in Figure 3, but with the power path itself (Figure 2). The total losses in the harvesting interface can be expressed as the sum of switching losses P_{sw}, conduction losses P_{cond}, and transfer losses P_{trans}:

$$P_{loss} = P_{sw} + P_{cond} + P_{trans} \quad (1)$$

$$P_{loss} = f_{vib} V_{out}^2 \sum \lambda_{C_{in_i}} W_i + \frac{1}{2} I_0^2 \sum \frac{R_S L_i}{W_i} + I_0^2 R_L \quad (2)$$

Where (W_i, L_i) are the width and length of each transistor in the power path, f_{vib} the vibration frequency, $\lambda_{C_{in}}$ the gate capacitance per transistor unit length, R_S the sheet resistance of the MOS channel, I_0 the RMS current in the inductance, and R_L the inductance parasitic resistance. Since f_{vib} is usually relatively low $\approx 20 - 1000 H_z$, the switching losses are usually much lower than the conduction and transfer losses. For a particular technology, there are three possibilities to reduce those losses:

-Decreasing I_0. This can be done thanks to circuit techniques, such as the Multi Shot-SECE [4], or by making faster harvesting events with a harvester/inductance of smaller size.

-Increasing W_i. However, this increases the surface of silicon used for the interface. In our case, to obtain an efficiency of 90% we had to use a silicon surface of $5mm^2$.

-Decreasing R_L. However, this usually lead to an increase of the inductance size.

C. Power limits of the interface

One major limit of any SECE-based interface relies in both the interface breakdown voltage and saturation current of the inductance. Indeed, the maximum extracted power from the harvester is given by:

$$P_{max} = min\left(f_{vib} V_{lim}^2 C_p, f_{vib} I_{sat}^2 L\right) \quad (3)$$

With C_p the capacitance of the piezoelectric material, ,V_{lim} the limit voltage that may be supported by the electrical interface, and I_{sat} the saturation current of the inductance L. If we want to increase P_{max}, there are three possibilities:

-Increasing C_p by an appropriate harvester design. However, since C_p is proportional to the surface of the piezoelectric material, this increases the harvester size.

-Increasing V_{lim} thanks to the choice of high voltage transistors/technology. In our case, we chose to use high voltage transistors from XFAB whose maximum V_{DS} and V_{GS} are 20V. However, the higher the voltage limit of a transistor, the greater its L_i. Therefore, choosing high voltage transistors will both increase their size and their conduction losses.

-Increasing LI_{sat}^2 by choosing an appropriate inductance. This choice should be made carefully since there is a direct relation between the saturation current value of an inductance and its size. All these tradeoffs have been summarized in Table1.

TABLE 1. TRADEOFFS FACED DURING THE INTERFACE INTEGRATION

	System size	Switching losses	Conduction losses	Transfer losses	Maximum power
Increasing the transistors sizes	☹	☹	☺☺	=	=
Increasing the harvester size	☹	=	☹	☹	☺
Increasing the inductance size	☹	=	=	=	☺☺
Choosing higher voltage transistors	☹	☹	☹☹	=	☺☺
Adopting multishot techniques	=	☹	☺	☺	☺☺

IV. CONCLUSION

In this paper, we present the design of an ASIC implementing the SC-SECE strategy. Transient waveforms and power frequency responses obtained with this circuit will be presented during the conference.

REFERENCES

[1] A. Badel et al., 2014, *J. Phys.: Conf. Ser.* **557** 012115
[2] A. Morel et al., 2018, *Smart Mater. Struct.* **28** 025009
[3] A. Quelen et al., 2018, *ISSCC proc.* , pp. 150-152
[4] P. Gasnier et al., 2014, *J. Solid-State Circuits*, **49**, pp. 1561-1570

Charge compensation and ionic conductivity in the $(MgCoCuNiZn)_{1-x}Li_xO_{1-\delta}$ high entropy oxides

N. Osenciat[1], D. Bérardan[1]*, D. Dragoe[1], B. Léridon[2], S. Holé[2], A.K. Meena[1], S. Franger[1], N. Dragoe[1]*

[1]ICMMO (UMR CNRS 8182), Université Paris-Sud, Université Paris-Saclay, F-91405, Orsay, France

[2]LPEM (UMR CNRS 8213), ESPCI-Paris, PSL Université, Sorbonne Université, F-75005, Paris, France

*David Bérardan, david.berardan@u-psud.fr and Nita Dragoe, nita.dragoe@u-psud.fr

***Abstract*—Investigating the parameters controlling the ionic conductivity of Li^+ in (MgCoNiCuZn)O high entropy oxides, we will describe, the charge compensation mechanisms that occur when Li^+ substitutes a 2+ element. Thanks to thermogravimetric analysis and X-ray photoelectron spectroscopy, we found out that, for low fraction of Li^+, compensation involves a partial oxidation of Co^{2+} into Co^{3+} and then, for large fractions of Li^+, a combination of cobalt oxidation and a formation of oxygen vacancies.**

I. Introduction

A new class of materials has been discovered in 2015 [1], the high entropy oxides (HEOx, by analogy with the High Entropy Alloys - HEA). The particularity of these materials is their stabilisation by minimizing the total Gibbs Energy, given by Eq. (1), thanks to their configurational entropy at high (and reasonable) temperature.

$$\Delta_r G = \Delta_r H - T\Delta_r S \quad (1)$$

To obtain these compounds, by maximizing their configurational entropy, we need to mix, at least, 5 binary oxides in equimolar proportions and heat them (above 875°C for this composition), followed by quenching to froze the structure at room temperature. In these conditions, they form a solid metastable solution in a simple rocksalt structure where the cations are randomly dispersed on the cationic sublattice (see Fig. 1 below).

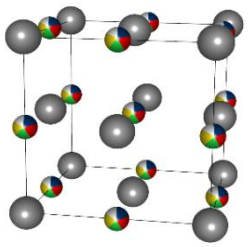

FIGURE 1. SCHEMATIC ROCKSALT STRUCTURE OF THE (MGCOCUNIZN)O HIGH ENTROPY OXIDE. IN GREY, THE ANIONIC SUBLATTICE OF OXYGEN, IN OTHER COLORS, THE CATIONIC SUBLATTICE OF RAMDOM ELEMENTS

First studies, performed in our lab, have shown the large possibilities of composition by substituting cations or modulating their ratio from the initial formula (MgCoNiCuZn)O when keeping the charge balance between cations and anions (M^{2+} and O^{2-}) [2] and their very promising properties such as their colossal dielectric constant [2], their alkali conductivity (Li^+ and Na^+) and their electronic insulation [3]. These specificities make them promising candidates for solid-state electrolytes.

With the ambition to improve the ionic conductivity of Li^+ in these compounds, currently 1 $mS.cm^{-1}$ at room temperature in $(MgCoNiCuZn)_{0.7}Li_{0.3}O$ [3], we have studied the $(MgCoNiCuZn)_{1-x}Li_xO$ series, x=0 to 0.30, to understand charge compensation mechanism of lithium insertion and its influence on Li^+ conductivity.

II. Experiemental methods

A. Synthesis

The $(MgCoNiCuZn)_{1-x}Li_xO$ series (x=0 to 0.30) were synthesized from mixed and ball milled oxides and carbonates precursors. The heating treatment, 950°C during 12h, were performed in a tubular furnace and the quenching process were realized by dropping the samples in liquid nitrogen.

In parallel, thermogravimetric analysis (TGA), under flowing oxygen, were performed to follow mass evolution during synthesis.

B. Structural characterisation

The structural information was determined by X-ray diffraction (XRD) measurements. The lattice parameters were obtained by refining diffraction patterns using FULLPROF software [4] and Le Bail fitting method [5].

C. Chemical characterization

X-ray photoelectron spectroscopy (XPS) analysis were used to investigate the chemical composition of several samples from the series and follow the chemical evolution with the lithium insertion.

D. Electrochemical properties analysis

Ionic conductivity was obtained by using electrochemical impedance spectroscopy (EIS) from 10 MHz to 10 mHz with a 100 mV AC perturbation. DC conductivity was estimated from the real part of the complex conductivity, at low frequencies (constant value on a large logarithmic range), using Eq. (2).

$$\sigma^*(f) = \frac{e}{S} \cdot \frac{1}{Z^*(f)} \quad (2)$$

III. Main results

With the study of the lattice parameter, we put forward two mechanisms occurring when adding lithium in the system. The lattice parameter decreases proportionally with the lithium concentration, up to about 20% of lithium. After this quantity, another linear trend appears with a smaller slope.

These two variations, below and above 20% of lithium, are consistent, respectively, with a charge compensation mechanism involving, at first, M^{2+} cations oxidation into M^{3+} (in our case, Ni^{2+} or Co^{2+}) and then, eventually, oxygen vacancies generation.

XPS analysis allowed us to identify the cation involved in the first charge compensation mechanism: the cobalt. Thus it was possible to follow the evolution of Co^{2+} and Co^{3+} compared to the lithium concentration. Conversely, Ni^{2+} concentration stay equal on each sample of the series.

However, by calculating weight loss during synthesis and proposing several scenarios of charge compensation, it appears that another element was oxidised between 16.67% and 21% of lithium fraction and then, the system starts generating oxygen vacancies.

The DC ionic conductivity of the different samples exhibit interesting performances in comparison with LiPON ones, 100 times more conductive at 80°C from 25% of lithium in the compound. However, we can also observe a slowdown of these properties from 20% lithium fraction. This fraction, as identified previously, is also the starting point where the system starts to create oxygen vacancies. Counterintuitively, these defects may trap the moving Li^{+} and play a negative role on the lithium mobility.

All the results established on this study carried out a recent paper [6] and the pictures are protected under copyright.

IV. Conclusion

The study of the $(MgCoNiCuZn)_{1-x}Li_xO$ high entropy oxides series allow us to highlight the different charge compensation mechanisms occurring when increasing the amount of lithium. First, the complete oxidation of Co^{2+} into Co^{3+} until 16,67% of lithium, then another unknown mechanism up to 20% of lithium, which have to be determined (with EPR, NMR for example) and finally the generation of oxygen vacancies. However, regarding the DC ionic conductivities, the presence of oxygen vacancies seems to have a negative impact on the lithium mobility. We propose to control their generation by properly adjusting the different cationic ratios (mainly the cobalt one) for the next steps of the study and will attempt to test this hypothesis.

Acknowledgment

We acknowledge the CNRS PEPS Energie 2017 program.

References

[1] C.M. Rost et al., Nature Commununications. 6, 8485, 2015

[2] D. Bérardan et al., Physical Status Solidi RRL 10, 328, 2016

[3] D. Bérardan et al., Journal of Materials Chemistry A 4, 9536, 2016

[4] J. Rodríguez-Carvajal, Commission on Powder Diffraction (IUCr). Newsletter, 26, 12-19, 2001

[5] A. Le Bail et al., Materials Research Bulletin 23, 447-452, 1988

[6] N. Osenciat et al., Journal of the American Ceramic Society (accepted and shortly published)

DC Voltage Improvement of a 2.4-GHz Rectifier using Multisine Signals

Viet-Duc PHAM[1,*], Hakim TAKHEDMIT[1] and Laurent CIRIO[1]
[1]Université Paris-Est. ESYCOM (FRE 2028) UPEM, ESIEE-Paris, CNAM. F.77454 Marne-la-Vallée, France
hakim.takhedmit@u-pem.fr

***Abstract*—This work reports the impact of using multisine signals in wireless power transmission (WPT) systems especially on the Cockcroft-Walton voltage multiplier developed for an electrostatic vibration energy harvester where the bias voltage has an important task to decrease the charging time of the capacitor plates. Several indicators such as peak-to-average power ratio (PAPR), instantaneous power variance (IPV) are calculated and used to predict the voltage gain of multisine signals compared to single tone signal. The measurement results show the improvement of DC voltage output with multisine signals where 8-tone signal's output is 1.6 V (2 dB voltage gain) higher than 1-tone signal at 0 dBm.**

***Key words*—Wireless Power Transmission, power optimized waveforms, voltage gain, PAPR, IPV.**

I. INTRODUCTION

Nowadays, the development of Internet of things, smart buildings, smart cities is leading our world to the new era in which millions of smart sensors and smart devices have to be powered up and connected together. For that reasons, WPT is one of the most effective ways we can rely on. In WPT, increasing the output dc voltage and/or the RF-to-dc conversion efficiency at low power input is one of the biggest challenges. The process of finding a better solution is underway. By considering some types of waveform such as multisine, OFDM, white noise and chaotic signal and their PAPR, the DC output (voltage and efficiency) is improved with higher PAPR at certain power levels [1]. Using multisine excitation, the N-tone sinusoidal signals with 0° phase difference between the tones, can significantly increase the voltage DC output and also the power gain [2-5].

In electrostatic vibration energy harvester, the mechanical vibrations are converted into electricity by a mechanical attraction force, which depends on the voltage supplied from the rectifier to the capacitor plate. Therefore, the voltage output of the rectifier is needed to be higher to reduce the time of charging the capacitor. With 2.4-GHz Cockcroft–Walton multistage rectifier [6,7], which is designed and optimized to operate at low power levels and provide high output DC voltage, the voltage output is notably improved.

In this paper, the measurements were performed in order to demonstrate the impact of multisine signals on the improvement of DC output of multistage rectifier.

II. MULTISINE SIGNALS

Multisine signals are considered as the most popular waveforms in WPT. Each multisine signal is a combination of several continuous sine waves with different frequencies, and/or different phases, amplitudes and frequencies spacing. The multisine signal's formula is as follow:

$$v(t) = \sum_{k=1}^{N} A_k . \sin\left\{\left[\omega - \frac{\Delta\omega}{2}(N-1) + \Delta\omega(k-1)\right]t + \varphi_k\right\} \quad (1)$$

Where A_k, φ_k, N are the amplitude, phase and the number of subcarriers; $\omega = 2.\pi.f$ where f is the center frequency; $\Delta\omega = 2.\pi.\Delta f$ where Δf is the frequency spacing between the carriers.

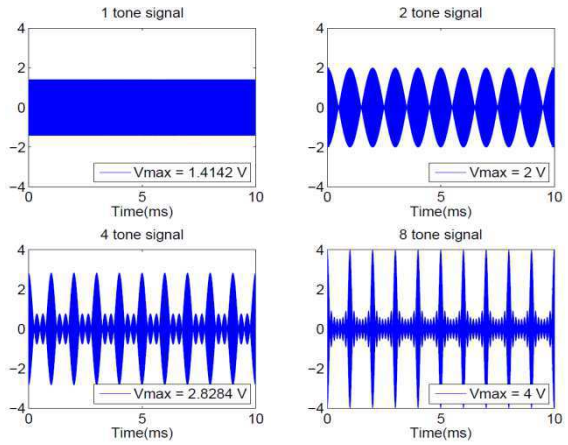

FIGURE 1. MULTISINE SIGNAL WAVEFORMS IN TIME DOMAIN

FIGURE 1 shows the multisine signal waveforms in time domain with different number of subcarriers. As can be seen, these multisine signals have different peaks even though having the same average power. Consequently, they acquire different PAPR values, which can be calculated by the following formula:

$$\mathrm{PAPR} = 10\log_{10}\frac{Max|x(t)^2|}{\langle x(t)^2\rangle} \quad (2)$$

Where x(t) is the time domain waveform of the signal; <x(t)> is the average value of x(t).

The PAPR of multisine signals is increased by 3 dB when the number of subcarriers is doubled. As the signals have a higher PAPR, higher peaks will be produced in the short period of time to overcome the threshold voltage of the Schottky diode used to build the RF-to-dc rectifier, which turns on the diode completely so that the higher DC output can be reached. The PAPR can be considered as a good indicator for low and medium input power levels, nevertheless, at high power input, other parameters should be regarded such as IPV [8,9], which can be calculated by the following formula:

$$\mathrm{IPV} = E[(P - P_A)^2] \quad (3)$$

Where P is the instantaneous power, P_A is the average power and E[ ] denotes the expectation [9].

IPV and PAPR of multisine signals are calculated and displayed in TABLE 1.

TABLE 1. PAPR AND IPV OF MULTISINE SIGNALS

Signals	Parameters	
	IPV	*PAPR (dB)*
1-tone signal	0.5	3
2-tone signal	1.25	6
4-tone signal	3.13	9
8-tone signal	7.06	12

III. MULTISTAGE RECTIFIER AND MEASUREMENT RESULTS

FIGURE 2a shows the prototype of the multistage rectifier optimized at the frequency of 2.4 GHz and at -15 dBm power input level. It contains 6 identical cascaded stages. Each stage consists of two Skyworks SMS 7630 Schottky diodes and two equal capacitors of 180 pF. The procedure of optimizing and simulating is completed by Advanced Device System (ADS).

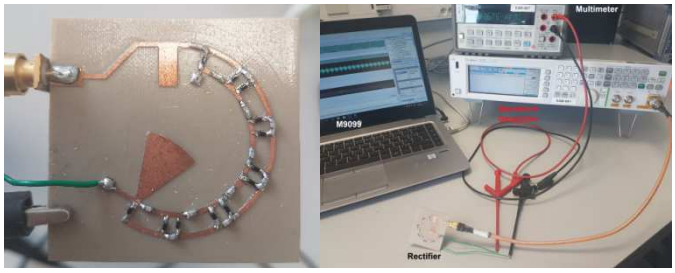

a) b)

FIGURE 2. RECTIFIER PROTOTYPE AND MEASUREMENT SETUP.

The measurement has been performed with the setup shown in the FIGURE 2b. To make the V_{DC} comparison clearer, the voltage gain is plotted using the formula:

$$\text{Voltage Gain} = 20\log_{10}\frac{V_{signal}}{V_{1-tone}} \qquad (4)$$

Where V_{signal} is the voltage output of the signal to compare with 1-tone signal's voltage output.

From FIGURE 3 and FIGURE 4, the maximum voltage output of 8-tone signal and 1-tone signal are 7.9 V and 6.3 V, respectively, at 0 dBm, which is a very good agreement with simulation results. The 8-tone signal gives the highest voltage output in all the input power range from -25 to 0 dBm. In terms of voltage gain, 8-tone signal has the highest gain of 2 dB, while 4-tone signal has the highest gain of 1.9 dB compared to 1-tone signal.

IV. CONCLUSION

This paper presents the effects of multisine signals on the voltage output of the multistage rectifier. The measurements were performed to show that multisine signals with higher PAPR tends to produce higher output DC voltage at low and medium power levels, which is important to improve the performance of electrostatic vibration energy harvester. The voltage gain of 8-tone signal is 1.6 times (2 dB) higher than 1-tone signal at 0 dBm.

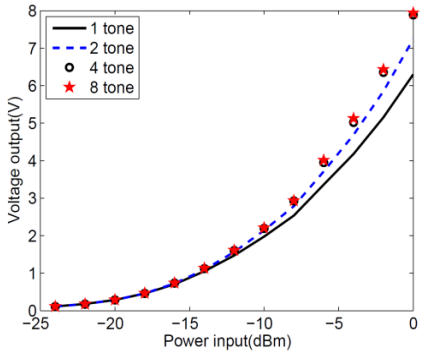

FIGURE 3. MEASURED OUTPUT DC VOLTAGE AGAINST INPUT RF POWER.

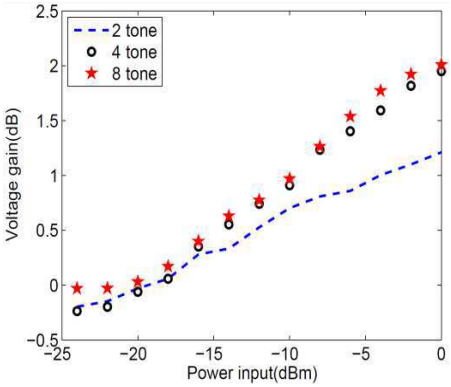

FIGURE 4. MEASURED VOLTAGE GAIN.

REFERENCES

[1] A. Collado, and A. Georgiadis "Optimal Waveforms for Efficient Wireless Power Transmission" *IEEE microwave and wireless components letters*, vol. 24, no. 5, May 2014

[2] Alírio Soares Boaventura and Nuno Borges Carvalho "Maximizing DC Power in Energy Harvesting Circuits Using Multisine Excitation" In Microwave Symposium Digest MTT - 2011 IEEE MTT-S International (pp. 1-4). IEEE.

[3] Trotter, M. S., Griffin, J. D., Durgin, G. D. (2009, April). "Poweroptimized waveforms for improving the range and reliability of RFID systems. In RFID, 2009 IEEE International Conference on (pp. 80-87). IEEE.

[4] Valenta, C. R., Durgin, G. D. (2013, April) "Rectenna performance under power-optimized waveform excitation,". In RFID (RFID), 2013 IEEE International Conference on (pp. 237-244). IEEE.

[5] H. Takhedmit, Z. Saddi, A. Karami, P. Basset, L. Cirio "Electrostatic vibration energy harvester with 2.4-GHz Cockcroft–Walton rectenna start-up" *Comptes Rendus Physique*, 18(2), 98-106.

[6] H. Takhedmit, L. Cirio, S. Bellal, D. Delcroix, O. Picon "Design and experiments of a 2.4 Ghz voltage multiplier for RF energy harvesting" *Proc. Power MEMS (2012): 448-451.*

[7] Boaventura, A., Belo, D., Fernandes, R., Collado, A., Georgiadis, A.,Carvalho, N. B. (2015) "Boosting the efficiency: Unconventional waveform design for efficient wireless power transfer,". IEEE Microwave Magazine, 16(3), 87-96.

[8] Viswanathan, M. (2013). "Simulation of digital communication systems using Matlab," [eBook]. Published: Feb, 18, 2013.

[9] Blanco, J., Bolos, F., Georgiadis, A. (2016) "Instantaneous power variance and radio frequency to dc conversion efficiency of wireless power transfer systems," IET Microwaves, Antennas and Propagation, 10(10), 1065-1070.

FDSOI 28 nm Rectifiers for RF Energy Harvesting

Edouard ROCHEFEUILLE[1,2,*], Tân-Phu VUONG[2], Frédéric ALICALAPA[1], Alexandre DOUYERE[1] and Pierre-Oliver LUCAS-DE-PESLOUAN[1]

[1] *LE2P Université de la Réunion, 15 Avenue René Cassin, CS92003, Saint Denis Cedex 9, Réunion*

[2] *IMEP-LAHC Grenoble-INP, 3 Parvis Louis Néel, CS50257, 38016 Grenoble Cedex 1, France*

*edouard.rochefeuille@univ-reunion.fr

***Abstract*—This paper presents simulation results on rectifying circuits in FDSOI 28 nm technology for RF Energy Harvesting at 2.45 GHz. First, it is showed that the dynamic back gate biasing of FDSOI diode-connected transistor improve by 14% the output voltage of a series rectifier compared to a standard ground biased transistor. Then a modified version of the voltage cancellation technique (VCT) structure is proposed and allows to produce 43% more output voltage than a series rectifier with no load. Finally, a possible technique to reduce the input impedance of FDSOI diode-connected transistor is showed by doing multistage VCT rectifier. Results show an input impedance reduced by 15 for a proposed VCT of 8 stages.**

I. INTRODUCTION

Nowadays, microelectronic field aims to focus more and more on systems miniaturization as the reduction of power consumption without compromises on the required performances. With these objectives, some studies have been realized on energy conversion applications in [1]. In addition to that, energy harvesting applications are considered to reduce the power consumption as in [2]. RF energy harvesting is also present in nanoelectronic scale, which is designed to power integrated Low-Energy devices and sensors. The primary features and challenges of the FDSOI compared to a standard technology are described in literature in [3]. On these facts, the aim of the present study is to show expected performances in FDSOI 28 nm technology for some energy harvesting circuits like rectifiers. In FDSOI 28 nm technology, there is no diode model. To accomplish the rectifying process we use a diode-connected transistor. It consists of connecting the gate directly to the drain of the transistor. However, FDSOI technology allows the polarization of the back gate, also known as the substrate access. This back gate biasing adds another degree of liberty on the transistor behavior such as its voltage threshold [4]. A proper back gate biasing decreases the threshold voltage and so increases the rectified voltage in the case of a rectifier with a diode-connected transistor. This performances are showed in the second section with a simple series rectifier. The work on integrated energy harvesting is still large and there are many optimized structures that offer better performances than the series rectifier. Among them, we present in the section 3 a promising structure which aims to cancel the consumed voltage threshold of the diode-connected transistor. Section 4 shows a technique to reduce the input impedance by doing multistage VCT rectifier.

II. BACK GATE BIASING OF DIODE-CONNECTED TRANSISTOR

The transistor back gate connection is also called substrate or bulk (B) connection. In this paper, only N channel-transistor is discussed. For example, for an N channel transistor in FDSOI, a negative back gate biasing increases the voltage threshold. The consequences are therefore bad circuit performances but lower current leakage. In the other hand, a positive back gate biasing decreases the voltage threshold and increases the performances so as increasing current leakage. In fact, by performing simulations, we see that the best performances in the case of RF rectifying circuits are obtained when the diode-connected transistor has its back gate biased directly connected to the drain. The transistor is therefore dynamically biased by the RF input. The corresponding schematic of the dynamic back gate biasing for a series rectifier is shown on FIGURE 1.

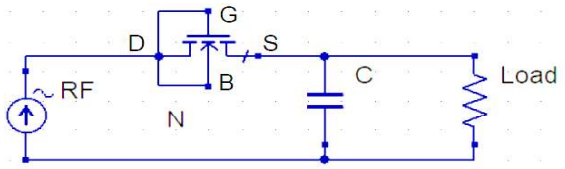

FIGURE 1. SCHEMATIC OF A SERIES RECTIFIER WITH DYNAMIC BACK BIASED DIODE-TRANSISTOR

The circuit on FIGURE 1 is simulated in FDSOI 28 nm technology using the minimal channel width and length of the Low Voltage Threshold (LVT) transistor. The LVT transistor has the lowest threshold voltage according to [4] and is the best transistor choice for energy harvesting at low power. The input power is set at 0 dBm at 50 Ω and the frequency is 2.45 GHz. The output capacitance is 100 pF in open circuit and transistor dimensions are W = 80 nm and L = 30 nm. FIGURE 3 shows output voltages of rectifiers depending on bulk connection and structure. Results show that the dynamic back gate biasing allow a 14% voltage improvement compared to a standard ground biasing diode connected transistor. Because the input impedance of the transistor is high and requires unacceptable large values of capacitor and inductance to match the 50 Ω, the simulation results presented in this paper doesn't include impedance matching. Section 4 discusses about a possible way to match input impedance.

III. VOLTAGE THRESHOLD CANCELLATION STRUCTURE

The principle of the voltage threshold cancellation technique is described in [5]. The structure is very close to a Dickson rectifier as in [1]. This paper proposes a modified version of the voltage cancellation technique (VCT) structure where the back gate of the second diode-connected transistor is directly connected to the source (the transistor is symmetrical,

drain and source are reversible). The equation Eq. (1) gives the theoretical output voltage depending of the transistor parameters:

$$Vout = 2 * N * (Vmax - Vth + Vbias) \quad (1)$$

FIGURE 2 shows circuit schematic of the proposed VCT.

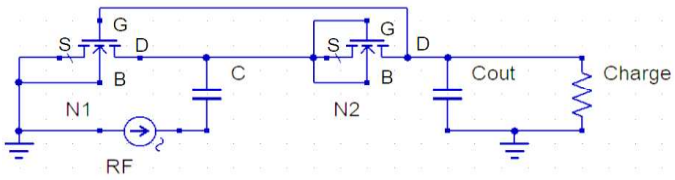

FIGURE 2. PROPOSED VCT STRUCTURE SCHEMATIC

The output rectified voltage obtained with the proposed modified VCT structure is compared with the original VCT and with the series rectifier on FIGURE 3. Simulations conditions are the same as in section one except that the VCT stage capacitor is set to 10 pF. Results shows a 7% output voltage improvement with the proposed structure compared to the original one and 43% compared the series rectifier.

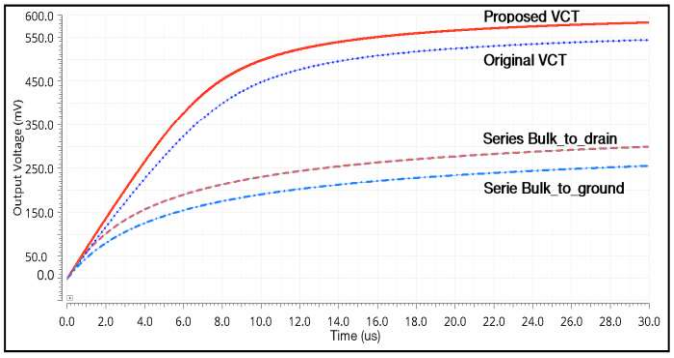

FIGURE 3. OUTPUT VOLTAGE OF PROPOSED VCT COMPARED TO ORIGINAL VCT AND SERIES RECTIFIERS

IV. RECTIFIER INPUT IMPEDANCE MATCHING

In the simulations, we have seen that the input impedance of rectifiers using diode-connected transistor in FDSOI 28 nm is really high. Depending of the load and capacitance the value of the real part goes from some kΩ to a few dozen of kΩ. The imaginary part is always negative and goes above the MΩ. The proposed modified VCT reduces by half the input impedance compared to the original structure. To reduce further the input impedance we propose to cascade the proposed VCT structure to do multistage. The cascade wiring of a 2 stages proposed VCT is shown on FIGURE 4.

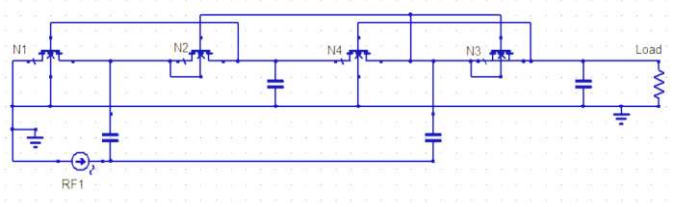

FIGURE 4. SCHEMATIC OF A 2 STAGES PROPOSED VCT RECTIFIER

The proposed cascade VCT links the two stages with the input but also with the gate control. The gate of the second transistor of stages is controlled by the input voltage and the output of the previous stage and keep therefore the connection as a diode-connected back biased to drain transistor. Real and imaginary impedance part of rectifiers are shown on FIGURE 5 according to the number of stage. Results show and input impedance reduced by 15 for a proposed VCT of 8 stages.

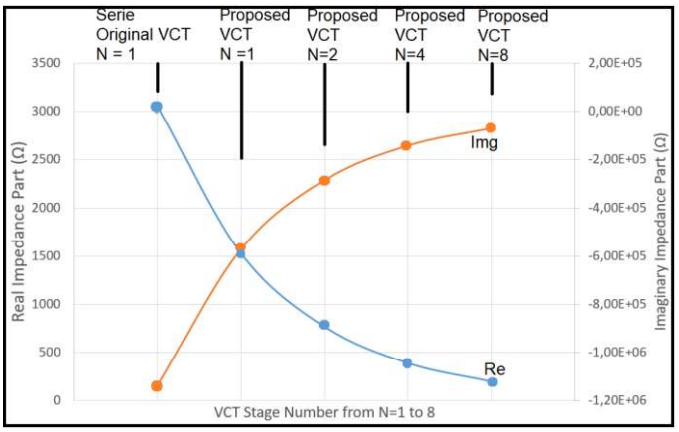

FIGURE 5. INPUT IMPEDANCE ACCORDING TO RECTIFIER STRUCTURE AND STAGE NUMBER N

V. CONCLUSION

This paper presents simulation results of the back gate biasing influence of a transistor on a series rectifier. Results shows a 14% improvement in output voltage of rectifier. A modified version of the VCT structure is presented and allow 43% more output voltage compared to a series rectifier. Finally, a method to reduce the input impedance of FDSOI rectifier is presented and show an input impedance reduction of a factor 15. We conclude that FDSOI 28 nm technology offers interesting compromises in terms of performances for RF energy harvesting.

ACKNOWLEDGMENT

The Author would like to thank Reunion Island Regional Council and the European Union – European Regional Development Fund (FEDER) PO 2014-2020 and the Auvergne Rhône-Alpes Regional Council for their financial support on this work.

REFERENCES

[1] M. Awad, P. Benech and J. Duchamp, "Design of Dickson rectifier for RF energy harvesting in 28 nm FD-SOI technology," *2018 Joint International EUROSOI-ULIS*, Granada, 2018, pp. 1-4.

[2] T. Paing, E. A. Falkenstein, R. Zane and Z. Popovic, "Custom IC for Ultralow Power RF Energy Scavenging," in *IEEE Transactions on Power Electronics*, vol. 26, no. 6, pp. 1620-1626, June 2011.

[3] D. H. Triyoso *et al.*, "Extending HKMG scaling on CMOS with FDSOI: advantages and integration challenges," *2016 ICICDT*, Ho Chi Minh, pp. 1-4 2016.

[4] E. Rochefeuille, F. Alicalapa, A. Douyère and T. P. Vuong, "Rectenna design for RF energy harvesting using CMOS 350nm and FDSOI 28nm," *2017 IEEE RADIO*, Cape Town, 2017, pp. 1-4..

[5] A. Hamani, Thesis "Design of an RFID Tag", *University Houari Boumediene*, Faculty of Electronics and Computers Sciences, 2017.

Vibration energy harvester based on a stainless steel cantilever with screen-printed PZT: SPS route.

Maria Isabel RUA-TABORDA[1,2*], Catherine ELISSALDE, U-Chan CHUNG[2], Alexis BRENES[3], Elie LEFEUVRE[4] and Hélène DEBEDA[1]

[1]*Université de Bordeaux, Laboratoire IMS, 33405 Talence, France*
[2] *CNRS, Université de Bordeaux, ICMCB, UMR-5026, 33600 Pessac, France*
[3] *ISEP, LISITE, 75006 Paris, France*
[4]*Université Paris-Saclay, C2N, 91120 Palaiseau, France*

*maria-isabel.rua-taborda@u-bordeaux.fr

***Abstract*—Piezoelectric thick films can be deposited on metallic supporting cantilevers to harvest higher power than thin films microstructured on Si wafers. Screen-printing process is a low-cost additive technology attractive for the PZT ($PbZrTiO_3$) films micro-structuration but the electromechanical properties are decreased because of residual porosity. Spark Plasma Sintering (SPS) route is here proposed to improve densification of supported PZT thick films on stainless steel (SS) substrate.**

I. Introduction

Attractive for piezoelectric MEMS, PZT films are often microstructured on silicon (Si) supporting platforms. Moreover, vibration energy harvester (EH) MEMS-based on piezoelectric thick films (1 to 100µm) lead to better energy densities than the thin layers and overcomes the assembly difficulties of bulk ceramics. Screen-printing process is an interesting option to microstructure these PZT films as it is a low-cost process for PZT-MEMS manufacturing. There is no need for thinning piezoelectric ceramics prior to electrodes deposition, and gluing step is not necessary [1]. Also, for vibration EH, metallic passive substrates are increasingly replacing Si substrates because of their higher flexibility [2-4]. Previous work proved the feasibility of a screen-printed energy harvester constituted of Au/PZT/Au/Stainless Steel (SS) multilayer structure [5]. But the co-sintering of such multilayer structure faces several issues including the use of sintering aids, the volatility of PbO and the presence of metals that significantly limit the temperature window for densification. However, highly densified PZT is mandatory to ensure performant electromechanical properties [6]. In order to avoid the use of sintering additives which decrease the firing temperature but also can modify the microstructure, we aim a two-fold strategy based on Spark Plasma Sintering. The objective is to improve PZT densification without any sintering aids while reducing the sintering temperature to a temperature suitable for the densification of the Au/PZT/Au/SS multilayer assembly in one step. This densification route of a multilayer for EH remains challenging. Only a few studies were reported on the use of SPS for electronic applications [7-9]. Issindou et *al* [7] sintered magnetostrictive ceramics for EH. Impact of copper particles addition into the PZT matrix was investigated for actuators application [8]. Multilayers stacking including two spiral copper coils was studied by Mercier et *al* for transformer application [9]. Here, the conventional screen printing process is first described. A simple cantilever based on the passive SS substrate covered with electroded PZT layer is used as a reference. The interfaces are thoroughly investigated and the generated power is measured with a shaker. The second part deals with the SPS process applied for the sintering of this cantilever structure.

II. Conventionnal Process

The fabrication of the PZT EH cantilever (Fig. 1) consists of subsequently screen-printing Au, PZT and Au layers on a SS substrate (SS301 10x2x0.250 mm^3), with a drying step at 120 °C between each deposition The layers are then isostatically pressed at 40 MPa before the co-firing of all the layers 2 hours at 900°C, in air. The pressure step improves the densification. The use of a sintering aid LBCu helps also improving the sintering [10] The final fired PZT thickness is approximately 50µm. The apparent porosity of the PZT printed layer is around 20%. EDS analysis shows that the interface layer (ca. 10 µm) contains elements coming from Au glass frit and SS substrate (Si, Al, Cd, Pb, Fe, Cr, Ni and, Mn).

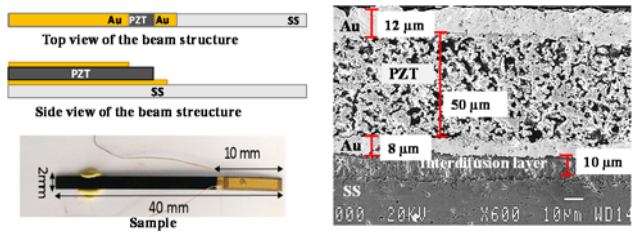

Fig 1. Cantilever (left) scheme and photograph and (right) SEM cross-section after co-sintering at 900°C.

After polarization of the layers at ~1 kV/mm and 280°C, the piezoelectric resonance can be checked by measuring the admittance. With a charge of 2.64 MΩ., a power of 1.3µW is produced by the harvester at 0.5 *g* amplitude with a natural frequency of 129.3Hz (Fig. 2). The harvested power is lower than those reported in the literature (Table 1). However, the substrate thickness and properties, the mass tip, the type of cantilever (i.e. unimorph or bimorph) and better piezoelectric properties represent several degrees of freedom to improve the performances. We focus on the last option in the next part.

Ref.	SS dimension / PZT thickness / Proof mass	Power/ frequency/ acceleration
[2], 2011	110µm/ Screen-printed PZT-5H/ 70µm (bimorph)/ Tungsten 3.1g	240µW/ 67Hz/ 0.4g
[3], 2013	300µm/ PZT RF Sputtering - 2.2µm/ Proof mass 25mg	6.7µW/ 367Hz/ 1g
[4], 2018	30µm/ PZT Aerosol 10µm (bimorph)/ Tungsten 0.46g	304µW/ 120Hz/ 0.5g
Our work	250µm/ Screen printed PZT + LBCu 50µm/ No proof mass	1.3µW/ 129.3Hz/ 0.5g

Table 1. Comparison with literature results.

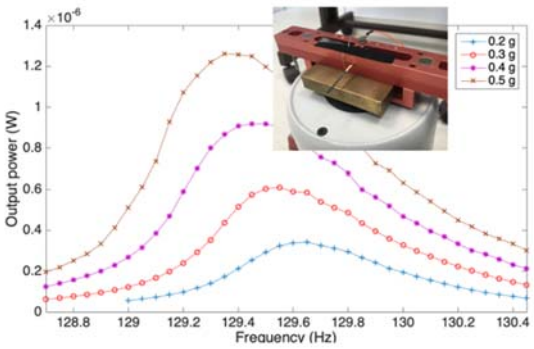

Fig. 2. Harvested power by the cantilever fabricated by the conventional process (2.64M load).

III. SPS PROCESS

SPS optimization of the PZT ceramics was first investigated under vacuum and 100MPa and at temperatures between 800°C and 900°C. Results show high densification close to 98%, even at 875°C. Also, a special protective layer based on $SrCO_3$ has been successfully tested (Fig. 3 and Fig. 4) to avoid the post-annealing treatment usually required to re-oxidize the PZT. With sputtered Au electrodes and after the poling step, a best electromechanical of 36% is measured. This encouraging result has led us to transfer SPS sintering on the simple multilayer Au/PZT/Au/SS cantilever. A modified graphite set-up has been designed for these experiments (Fig. 3) and the sintering temperature lowered down to 850°C.

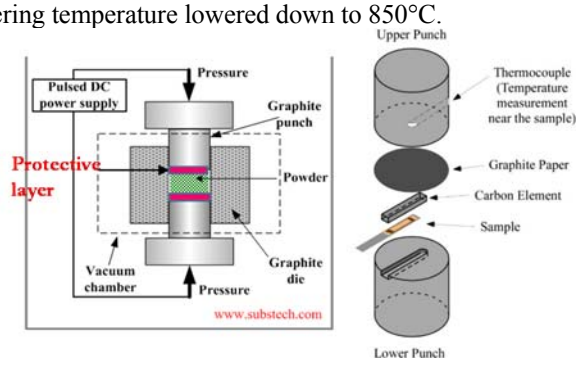

Fig. 3. (Left) Scheme of the SPS principle including the use of protective layer and (Right) Specific SPS designed mold.

Without sintering aid, a similar microstructure as for the conventional process is observed (Fig. 5a). Delamination between the Au bottom electrode and the PZT are nevertheless observed preventing the EH test. By reintroducing the LBCu sintering aid and hence reducing the co-sintering temperature down to 780°C, no delamination occurs. The PZT microstructure looks also more homogenous with a higher grain size (Fig. 5b) similar to that of the conventional process (Fig. 5c). In this case, instead of using the $SrCO_3$ protective layer, a carbon felt is placed on the Au layer. A post-thermal treatment step is nevertheless necessary, at 600°C during 2h, to remove the carbon contamination before the polarization.

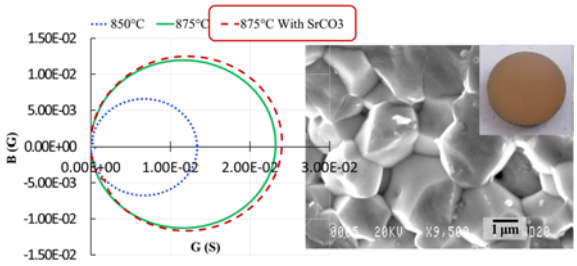

Fig. 4. (Left) Admittance B(G) circle for different SPS ceramics (Right) SEM image for ceramic sintered at 875°C (with $SrCO_3$).

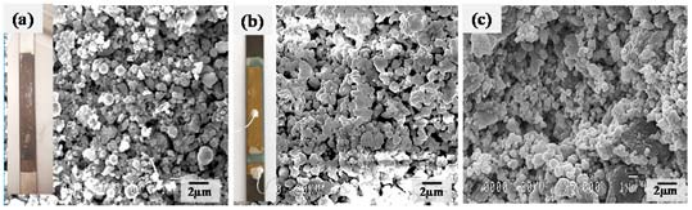

Fig. 5. PZT SEM microsections of cantilevers sintered (a) by SPS, 850°C, 5 min ($SrCO_3$ use + no LBCu) (b) by SPS 780°C, 5 min (LBCu use + no $SrCO_3$ (c) conventional firing at 900°C, 2h (LBCu).

CONCLUSION

For a simple cantilever constituted of a SS substrate where Au/{PZT + sintering aid} /Au are screen-printed and co-sintered at 900°C, harvested power at a µW level was measured, insufficient to envisage supply of MPTT power optimization circuit. Among the numerous options to improve such performances, we focused on the improvement of the PZT densification in one step by SPS. This allowed us to reduce the sintering temperature (<850°C). PZT microstructure with or without sintering aid appears to be similar to that of the conventional process. Further electromechanical tests are under progress to improve the cantilever performances.

REFERENCES

[1] M. Colinet *al*. J. Phys.: Conf. Ser. 476 (2013), 012133.
[2] D. Zhu et *al*. Sensors and Actuadors A, 169,317, 2011.
[3] Y Tsujiura et *al*, Transducers 2013, Barcelona, SPAIN, 16-20 June 2013
[4] W H Tang et *al* , Journal of Physics: Conf. Series 1052 (2018) 012038
[5] Fernandes et *al*., Smart Materials and Structures, 27(3), 2018
[6] R. Lou-Moelleret *al*, J. Electroceramics. 19, 333–338. 2007
[7]V. Issindou et *al*., Sens. Actuat. A 284 (1) (2018)
[8]M.H. Fang et *al*., Mater. Sci. Forum 423–425 (2003) 423–426.
[9] A. Mercier et *al*, IEEE Trans. Magn. 52 (5) (2016) 8400404.
[10] H. Debéda et *al*., Smart Mater. Struct. 24, 2015, 02

Processing and characterization of printed AgPd/PZT/AgPd microdisks for piezoelectric vibration energy harvesters

Onuma SANTAWITEE[1,*], Chanchana THANACHAYANONT[2], Jerome BERNARD[3], and Hélène DEBEDA[1]

[1] *Université de Bordeaux, IMS, UMR 5218, 351 Cours de la Libération, Bat A31, 33405 Talence Cedex, France*

[2] *National Metal and Materials Technology Center, 114 Thailand Science Park, Paholyothin Road, 12120 Pathumthani, Thailand*

[3] *Université de Caen Basse-Normandie (UCBN), LUSAC, EA 4253, Site Universitaire-60 rue Max Pol Fouchet, CS 20082, 50130 Cherbourg-Octeville, France*

*corresponding onuma.santawitee@u-bordeaux.fr

***Abstract*—Microdisks of $PbZr_{0.52}Ti_{0.48}O_3$ (PZT) are prepared by screen-printing associated with a polyester sacrificial layer. A printed disk sandwiched between printed AgPd electrodes can be totally released from substrates during sintering at 900°C. With a nanometric PZT powder, electromechanical and dielectric properties of the printed disk are improved. Piezoelectric vibration energy harvesters can be fabricated with these printed disks bonded on a resonant cantilever.**

I. INTRODUCTION

Common piezoelectric energy harvesters (EH) of millimeter size are cantilevers, unimorph or bimorph, with two pieces of bulk piezoelectric material sandwiching a metallic stainless substrate [1]. One option for reducing the size of these EH while keeping a good level of harvested power is a thinning of the bulk ceramic. Once thinned, this bulk ceramic can be bonded on metallic supports [2], but also on silicon substrates [3]. For instance, a power of 3 µW at 15 Hz and 10 mg was measured with two PZT layers (50 µm thick each) of the thinned bulk ceramic reported on a stainless substrate (bimorph type) [2]. Here, we propose a process to achieve performing thin PZT (≈100 µm) micro-ceramics obtained by successive layer printing. Compared with a previous process developed in our lab [4], a low cost AgPd (90:10) electrode, a nanometric PZT powder size and a new sacrificial layer are used to improve the electromechanical properties of the disks.

II. METHODOLOGY

A. Sample preparation

Screen-printing pastes used in this work are shown in TABLE 1. Electrode and sacrificial layer pastes are commercial whereas a PZT paste is home-made. It is prepared by mixing of milled PZT powder (by an attritor) with particle size of under 1 µm, 3 wt% LBCu sintering aid (26.7 wt% Li_2CO_3, 40.0 wt% Bi_2O_3 and 33.3 wt% CuO) and a suitable mass of organic binder (ESL V400) to form the printable PZT paste. Each paste is screen-printed on a ceramic AlN substrate with sequences in TABLE 1. A mask's diameter of PZT disks is 9 mm and masks' thicknesses of sacrificial layer, electrode and PZT layer are 50, 15 and 150 respectively. After screen-printing, each layer is dried at 120°C for 30 minutes except the PZT layer which is dried at 120°C for an hour with slow heating up. Then, printed disks are pressed with isostatic pressure before co-firing at 900°C for 2 hours. This co-firing leads to PZT sintering and elimination of the sacrificial layer at the same time (FIGURE 1).

TABLE 1. SCREEN-PRINTING LAYERS AND SEQUENCES OF SCREEN PRINTING

Order	Layer nature	Active element	Commercial name	Manufacture
1	Sacrificial layer	Polyester	ESL 244-T	ElectroScience Laboratory
2	Bottom electrode	AgPd	-	EXXELIA
3	Piezoelectric material	PZT	Pz26 and ESL V400	Ferroperm and ElectroScience Laboratory
4	Top electrode	Ag/Pd	-	EXXELIA

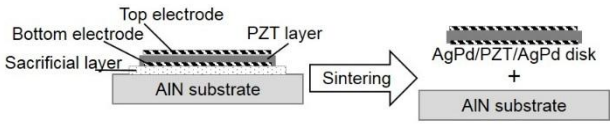

FIGURE 1. DRAWING OF SEPARATION BETWEEN A SINTERED DISK AND A SUBSTRATE AFTER DECOMPOSITION OF SACRIFICIAL LAYER

B. Characterization

For the printed AgPd/PZT/AgPd disks, diameter changes (before and after sintering) of the PZT layer and its electrodes are observed by an optical microscope (OM). The lateral shrinkage percentage is then calculated. Next, sintered AgPd/PZT/AgPd disks are cross-sectioned in order to observe thicknesses and microstructures by OM and SEM respectively. The porosity percentage is analyzed by ImageJ. Density of sintered PZT disks without electrodes are measured by a gas pycnometer. The sintered AgPd/PZT/AgPd disks are polarized at 280°C for 10 minutes under a nitrogen atmosphere. An Agilent E5063B network analyzer is used to measure the capacitance (C_p) at 1 kHz for calculation of the relative permittivity (ε_r). Impedance spectrum for the planar vibration mode is also investigated with this network analyzer.

III. Results and Discussion

A. Microstructures

Top and bottom sides of the sintered AgPd/PZT/AgPd disk are shown in FIGURE 2(a) and (b). Bottom electrode displays uniform releasing from a substrate. The thicknesses of top electrode, PZT layer and bottom electrode are around 12, 115 and 12 µm respectively. The disk's diameter is approximately 7500 µm. Pores within the disk are presented in FIGURE 2(c) and (d). The porosity percentage, the lateral shrinkage percentage, and density of the disk are around 6%, 14%, and 7.5 g/cm^3 respectively. The density is clearly improved compared to a previous printed disk [4], as it can see in TABLE 2.

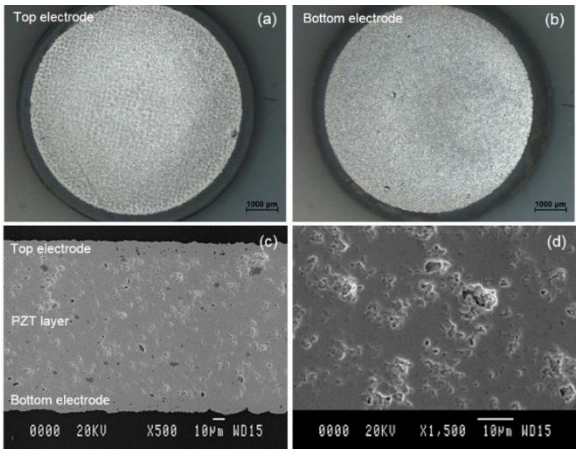

FIGURE 2. OM IMAGES OF THE SINTERED DISK (A) TOP, (B) BOTTOM ELECTRODES; AND SEM IMAGES OF CROSS-SECTIONAL AREAS OF SINTERED DISK AT (C) X500, (B) X1500 MAGNIFICATION

B. Electromechnical and dielectric properties

Impedance modulus and phase angle as a function of frequency for the AgPd/PZT/AgPd disk are plotted in FIGURE 3(a). The effective electromechanical coupling coefficient (k_{eff}) is calculated from Eq. (1).

$$k_{eff} = \sqrt{\frac{f_a^2 - f_r^2}{f_a^2}} \quad (1)$$

where f_a and f_r are anti-resonance and resonance frequencies measured from the impedance spectra respectively.

Maximum phase angle θ of the disk are around 88° (FIGURE 3(a)). This value is slightly lower than the ideal value (90°). It means that the disk has small energy loss. FIGURE 3(b) shows that the abscissas of the left part of an admittance circle of the disk reach to zero. This implies that the dielectric loss is very low. According to TABLE 2, the $\%k_{eff}$ of the disk is increased compared to the previous printed disk [4]. Furthermore, the ε_r of the disk is very close to the value of a Pz26 ceramic co-fired at 1200-1300°C. The improvements of electromechanical and dielectric properties of the disk are related to an increase of densification in PZT microstructure and electrode materials. The nature of the sacrificial layer is also an important parameter improving the densification.

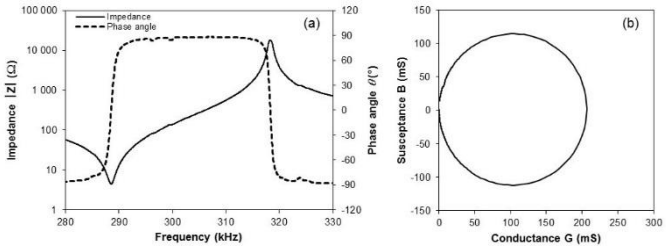

FIGURE 3. (A) IMPEDANCE MODULUS AND ANGLE AS A FUNCTION OF THE FREQUENCY AND (B) ADMITTANCE CIRCLE FOR THE PRINTED DISK

TABLE 2. DENSITY AND ELECTROMECHANICAL PROPERTIES OF THE PRINTED DISK COMPARED WITH OTHER DISKS OF PREVIOUS RESEARCH

Sample	**Density (g/cm^3)**	**$\%k_{eff}$**	**ε_r**
Printed disk *(polyester sacrificial layer + AgPd electrodes)*	7.5	42	1200
Previous printed disk [4] *($SrCO_3$ sacrificial layer + Au electrodes)*	5.0	15	-
Pz26 ceramic [5]	7.7	57	1300

IV. Conclusion

The printed AgPd/PZT/AgPd microdisks (with the PZT layer is about 100 µm thick) are successfully fabricated by the screen-printing associated with sacrificial layer technique. The electromechanical coefficient higher than 40% is obtained. In the future, these microstructures will be bonded to a cantilever structure designed for an ambient energy harvesting application. The process could be also adapted to free lead materials such as KNN.

Acknowledgment

The authors would like to thank the Royal Thai Government for a scholarship and Mr. X. Hochart (EXXELIA) for AgPd paste supporting and the isostatic pressure step.

References

[1] S. Round and P. K. Wright, "A Piezoelectric Vibration Based Generator for Wireless Electronics," *Smart Materials and Structures*, vol. 13, pp. 1131-1142, 2004.

[2] M. Colin, S. Basrour, C. Bantignies and A. Nguyen-Dinh , "Highly Efficient Low-frequency Energy Harvester Using Bulk Piezoelectric Ceramics," *Journal of Physics: Conference Series*, Vols. 476, No. 1, p. 012133, 2013.

[3] E. E. Aktakka, R. L. Peterson and K. Najafi, "Thinned-PZT on SOI process and design optimization for piezoelectric inertial energy harvesting," *Transducer's 11 (Beijing)* , pp. 1649-1652, 2001.

[4] H. Debéda, M. Maglione, V. Pommier-Budinger , X. Hochart, W. Sourbe and C. Lucat, "Feasibility of screen-printed PZT microceramics for Structural Health Monitoring applications," *International Journal of Applied Ceramic Technology*, Vols. 11, No. 3, pp. 413-421, 2014.

[5] *https://www.meggittferroperm.com* (last viewed:12/04/2019)

Characterization of the Solar Cells Under the Real Conditions

Jakub SVATOS[1,*], Jan HOLUB[1]

[1] *Department of Measurement, Czech Technical University in Prague*
Prague 166 27, Czechia

*svatoja1@fel.cvut.cz

***Abstract*—With an increasing number of wearable devices of all shapes and forms, which are equipped with new types of sensors to count steps, measure heart rate or even detect a fall, there is a requirement for more energy. Energy harvesting is one of the possible ways to increase the energy capability of such devices. The solar cells offer a renewable green source of energy to increase the power of wearable devices. At present, there is no binding uniform methodology for Solar Cell characterization under real light conditions of everyday life. The article presents a daily generation of energy in various daily life activity such as walking, car driving or office working with indoor illuminating. The solar cell, working in Maximum Power Point Tracking, attached to the hand of the person has been used. The presented results show expected amounts of generated energy in everyday life activities, which could be used for a better characterization of solar cells in the future.**

I. Introduction

The world market for wearable electronic, such as smart watches, fitness bracelets or wearables for medical application, such as Smart patches, continue very fast with its growth [1]. With an increasing number of wearable electronics also new functions of such devices increases. New types of sensors offer new functions such as monitoring of the wearer heart rate, stress level or, for example, can detect a fall of the wearer. On the other hand, with increasing number of functions there is a need to increase the energy capability of these devices [2] and [3]. One of the possible ways to increase the energy capability is energy harvesting. The energy harvesters generate a small amount of usually renewable green energy in form of solar power, thermal energy, wind energy or potential gradients to power low-energy devices. Solar cells energy finds its use in various wearable applications such as watches, bags, clothes or even sunglasses. At present, to characterize these solar cells under the real light conditions of everyday life, there is no any binding uniform methodology. The performance of solar cells and panels is given in Wp (watt peak). The performance depends strongly on the illumination and on the angle of the incident light. Therefore, the performance of the cells is measured under the defined conditions: energy density of solar radiation 1000Wm^{-2}, Air mass AM1.5 and temperature of 25°C. In practice, most of the time, the performance of the solar cell lower is lower due to orientation of the cell to the sun or others sources of light. In addition, the light goes through different layers of atmosphere depending on the time of day and amount of incident solar radiation is heavily dependent on the cloud. This article presents the expected performance of solar cell under the ordinary daily life activities such as driving, office working or walking in the shopping mall. The SOLEMS solar cell working in Maximum Power Point Tracking (MPPT) regime [4], attached to a hand of a test person has been used to measure the expected values of average power supply. The measured values could be used for better characterization of the cells performance used for the wearable devices in real conditions (i.e. indoor and outdoor illumination).

II. Methods

The SOLEMS solar cell of size 50 mm x 50 mm with 10 stripes has been used for the experiment. The cell has been attached to the arm above the elbow of the person, see Fig. 1.

FIGURE 1. Measured solar cell attached to the arm of the person

Since the efficiency of the solar cell power depends on both the amount of light falling on the solar panels and the electrical characteristics of the load, measured power of the cell has been optimized using MPPT. The P-V characterization of the SOLEMS cell is in Fig. 2.

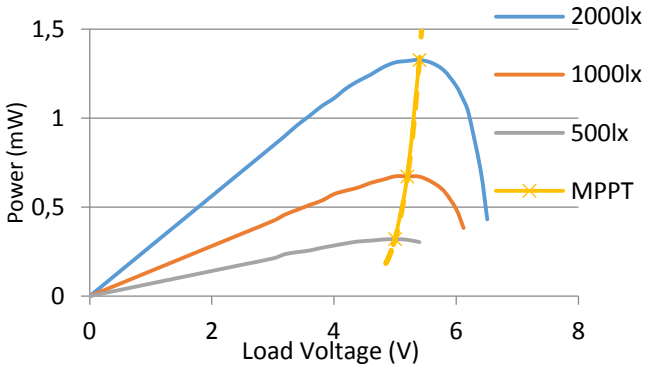

FIGURE 2. The MPPT of the measured solar cell

The load has been simulated according to measured MPPT by passive non-linear circuit that input impedance has been optimized to track the yellow line in Fig. 2 (MPPT). Various

daily life scenarios have been performed to measure the accumulated energy. Having a breakfast, a lunch, driving a car, working in offices under different scenarios (close to the window, or without direct sunlight) and walking in a shopping mall has been acquired.

III. Results

Examples of operational measurement with optimal MPPT simulators are presented in next figures. Fig. 3 show example of recorded values correspond to current (blue) and voltage (red) generated by Solems solar cell during a three hour car drive. The measured data showed the overall accumulated energy recalculated to one hour is approx. 4.6 Ws, which corresponds to the mean power delivery of 1,25 mW.

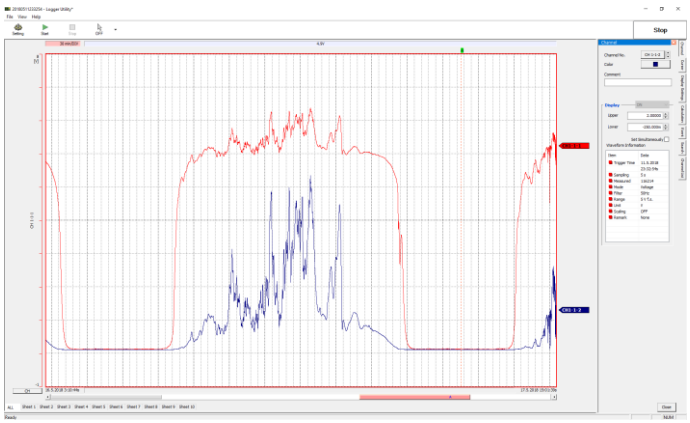

FIGURE 3. TYPICAL MEASURED VALUES GENERATED BY SOLEMS SOLAR CELL CORRESPOND TO CURRENT (BLUE) AND VOLTAGE (RED) DURING A CAR DRIVING

Another example of energy generation in an office with two different scenarios through five consecutive days is in Fig. 4 and Fig. 5. Fig. 4 presents the overall daily energy generation in an office when the solar cell has been located in a place with no direct sunlight.

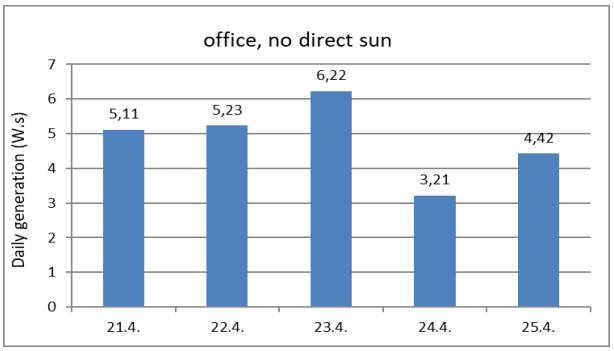

FIGURE 4. DAILY GENERATION OF ENERGY, OFFICE WITH NO DIRECT SUN

Fig. 5 shows the same office and the same solar cell but this time oriented close to the windows.

The overview of accumulated energy and equivalent mean power delivery during the daily life scenarios are shown in Table 1.

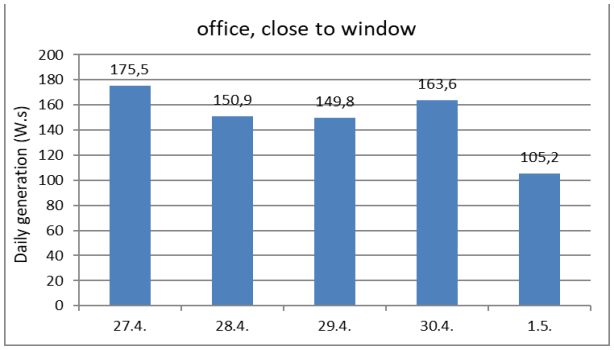

FIGURE 5. DAILY GENERATION OF ENERGY, OFFICE, CLOSE TO WINDOWS

TABLE 1. SOLEMS SOLAR CELL DAILY LIFE SCENAIROS MEASUREMENT

Activity	Accumulated Energy (mWs)	Equivalent Mean Power Delivery (mW)
15 min Breakfast	59,983	0,066
45 min Car Driving	3449,174	1,250
60 min Shopping mall walk	2197,505	0,600
30 min Sitting in Car (Direct Sun)	6751,285	3,630
70 min Restaurant Lunch	210,875	0,050

IV. Conclusion

The article presents amount of accumulated energy of Solems solar cell, working in optimal MPPT load, during the common daily life scenarios. Measured values could help with better characterization of solar cells used for example for wearable devices.

Acknowledgment

This research was supported by the "Energy for Smart Objects" grant provided by Electronic Components and Systems for European Leadership Joint Undertaking in collaboration with the European Union's H2020 Framework Programme (H2020/2014-2020) and National Authorities, under grant agreement n° 692482.

References

[1] International Data Corporation (IDC), https://www.idc.com/cee (last viewed:04/01/2019).

[2] A. Pantelopoulos and N. G. Bourbakis, "A Survey on Wearable Sensor-Based Systems for Health Monitoring and Prognosis," *IEEE Transactions on Systems*, Man, and Cybernetics, Part C (Applications and Reviews), vol. 40, no. 1, pp. 1-12, Jan. 2010.

[3] C. Yang and Y. Hsu, "A Review of Accelerometry-Based Wearable Motion Detectors for Physical Activity Monitoring" *Sensors*, vol. 10 no. 8, pp. 7772 – 7788, 2010.

[4] M. A. G. de Brito, L. Galotto, L. P. Sampaio, G. d. A. e Melo and C. A. Canesin, "Evaluation of the Main MPPT Techniques for Photovoltaic Applications," *IEEE Transactions on Industrial Electronics*, vol. 60, no. 3, pp. 1156-1167, 2013.

Nanostructuration and thermoelectricity

Konstantinos TERMENTZIDIS[1,*]
[1] *CNRS, CETHIL-UMR 5008, INSA Lyon, 9 Rue de la Physique*
69100 Villeurbanne, FRANCE

*konstantinos.termentzidis@insa-lyon.fr

Abstract

Nanostructures and nanostructured materials as 2D and 3D nanowire networks or phononic crystals are potential metastructures for nanoelectronics and thermoelectric applications. This new class of nanoarchitectured materials have interesting physical properties due to their low mass density and their high surface-to-volume ratio. Here, we report on thermal transport properties in 2D and 3D interconnected nanowire networks as well in phononic crystals taking into account the existence of native oxides.

I. INTRODUCTION

With the rapid development of new fabrication techniques, new classes of materials with particular physical properties have emerged. For example, ultrathin membranes with or without holes or pillars are interesting candidates to tune heat transport. Among them, the so-called phononic crystals (PnC) are structures with periodic or not hole patterning, which have attracted scientific interest these past years due to new physical phenomena but also for their potential applications in several applications. Concerning, 2D or 3D nanowires networks, they are proposed as optoelectronic or biological devices and sensors due to their mechanical strength and flexibility. These networks ordered or disordered migh be useful for complex integrated nanoelectronic circuits [1]. The characteristic sizes of phononic crystals or nanowire neteworks are now of the order of some tens of nanometers.

The thermal properties of such nanostructures or nanostructured materials is known to diverge from classical physics [2], especially in semiconductors where heat is mostly carried by lattice vibrations (phonons). Interestingly, nanostructuration usually reduces the thermal conductivity due to boundary or interface scattering, while the electrical properties could be preserved [3]. The design of nanostructured materials with ultra-low TC, sometimes sub-amorphous while keeping a large crystalline fraction, is now possible [4,5]. Nanoporous materials may have even lower thermal conductivity because of the removal of material [6,7].

Two model systems are presented here: phononic crystals and 2 and 3D nanowire networks. For the first group, several systems are modeled to investigate the impact of amorphous shells around the holes and amorphous edges at top and bottom surfaces of the membrane on the thermal conductivity. The shell contains either amorphous silicon (a-Si) and/or silica (a-SiO_2). Concerning the nanowire networks, the networks are consisting of interconnected silicon nanowires with a square cross section forming a 2D or 3D network (figure-1).

II. SIMULATION METHODOLOGY AND RESULTS

A. Molecular Dynamics

All simulations were performed with LAMPPS open source software [8], using the Stillinger-Weber potential for silicon with modified coefficients [9]. The structures are built from a slab of bulk crystalline silicon, deleting atoms of certain regions to obtain the desired nanostructuration. Periodic boundary conditions are applied along two or three directions to model an infinite phononic crystal or 2D or 3D nanowire network, respectively. Then a conjugate gradient minimization is done and the structures are relaxed at 300 K under NVT ensemble during 200 ps. Finally, the thermal conductivity at room temperature is extracted thanks to Green-Kubo formalism, estimating the correlation of flux fluctuations during 10 ns with a time window of 40 ps.

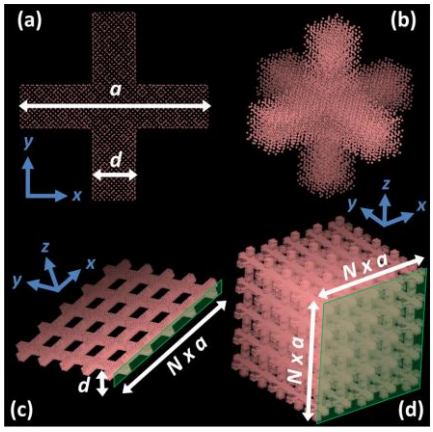

FIGURE 1. VISUALISATION OF 2D AND 3D NANOWIRE NETWORKS (UPPER ONE SIMULATION CELL, DOWN AFTER PERIODIC BOUNDARY CONDITIONS)

B. Results

The impact of amorphous phases around the holes and at the upper and lower free surfaces on thermal transport in silicon phononic membranes is depicted in figure-2 [10]. The reduction of the TC due to silicon dioxide (yellow shells) is greater than that due to amorphous silicon (red shells). Increasing the thickness of the amorphous shells of holes or edges of membranes (exposure of the membranes to nonprotective conditions) leads to an important decrease of the thermal conductivity, even to ultralow subamorphous thermal conductivity keeping a large fraction of crystalline material.

We found also that, when an amorphous phase is added, the key parameter to control heat transfer is the crystalline neck distance and not the distance between the two voids. Decreasing the neck distance between holes varying their diameter or their period results in a sharp decrease of their effective thermal conductivity. This effect is more pronounced for phononic crystals with small dimensions, particularly when the neck is small. We have shown that external amorphous surfaces of membranes reduce further the TC for both plain membranes and phononic crystals ones. Interestingly, when the crystalline thickness of the membrane is kept constant and thicker external amorphous layers are added, the thermal conductivity decreases sharply. That means that phonons become more confined in the same crystalline volume when amorphous material is added around them. Subamorphous TC appears in several studied systems, making phonon engineering possible upon controlling the native oxides.

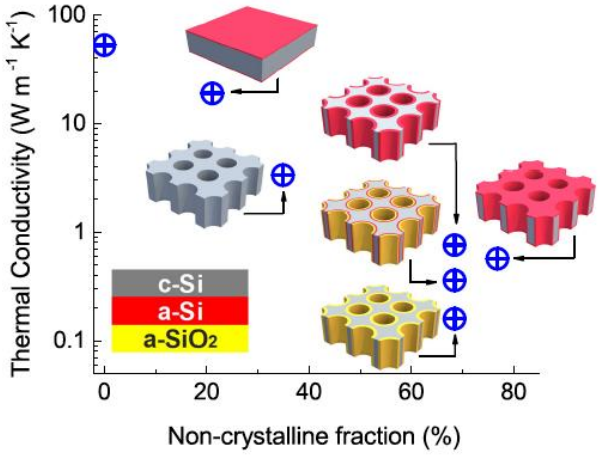

FIGURE 2.THERMAL CONDUCTIVITY OF PLAIN MEMBRANE AND PHONONIC CRYSTALS WITH AND WITHOUT AMORPHOUS SHELLS AND EDGES AS A FUNCTION OF THE NON-CRYSTALLINE FRACTION.

Concerning the 2D and 3D nanowire networks, the reduction of the thermal conductivity compared to the bulk crystalline silicon (at 300 K, 150W/mK) can reach 3 or 4 orders of magnitude in 2D and 3D networks, respectively [11]. Such low values seem surprising but can be explained by the extremely high porosity, which reaches 81% for 2D networks and 97% for 3D networks studied here. The lowering of thermal transport is more pronounced in the 3D networks than in the 2D networks, because 3D structures have higher porosity and their nodes have more branches, which leads to increased backscattering and larger thermal resistance in such nodes. A model based on equivalent thermal resistances reproduces the main trends of the molecular dynamics results and confirms these interpretations.

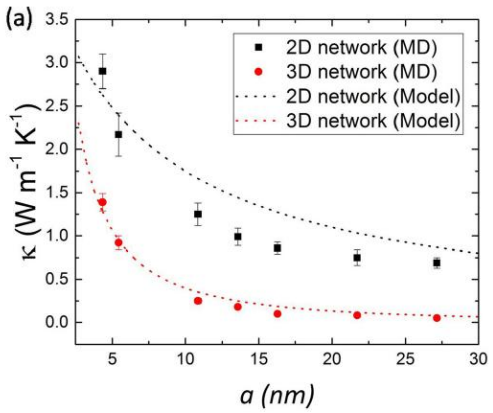

FIGURE 3.THERMAL CONDUCTIVITY OF 2D AND 3D NANOWIRE NETWORKS AS A FUNCTION OF THE PERIOD OF NODES WITH A CONSTANT NANOWIRE DIAMETER OF ~3NM AT ROOM TEMPERATURE.

III. CONCLUSIONS

The hierarchy of the impact of the orientation and the nature of interfaces on the reduction of the thermal conductivity of phononic crystals and the dimensionality of nanowire networks is studied here. A crucial parameter is the porosity but also the orientation of the surfaces in respect to the heat flux. Surfaces perpendicular to the heat flux impact greater the thermal transport, while native oxides lead to the further reduction of the effective thermal conductivity.

ACKNOWLEDGMENT

I would like to thank the coauthors of references [10] and [11] and specially the excellent PhD work of Maxime VERDIER.

REFERENCES

[1] J. M. Romo-Herrera, M. Terrones, H. Terrones, S. Dag, and V. Meunier, "Covalent 2d and 3d networks from 1d nanostructures: Designing new materials", *Nano Lett.* 7, 570, 2007

[2] D. G. Cahill, P. V. Braun, G. Chen, D. R. Clarke, S. Fan, K. E. Goodson, P. Keblinski,W. P. King, G. D. Mahan, A. Majumdar, H. J. Maris, S. R. Phillpot, E. Pop, and L. Shi, "Nanoscale thermal transport, II". 2003–2012, *Appl. Phys. Rev.* 1, 011305, 2014.

[3] J.-H. Lee, G. A. Galli, and J. C. Grossman, "Nanoporous Si as an efficient thermoelectric material", Nano Lett. 8, 3750, 2008.

[4] H. Mizuno, S. Mossa, and J.-L. Barrat, "Beating the amorphous limit in thermal conductivity by superlattices design", *Sci. Rep.* 5, 14116, 2015.

[5] M. Verdier, K. Termentzidis, and D. Lacroix, "Crystalline-amorphous silicon nano-composites: Nano-pores and nanoinclusions impact on the thermal conductivity", *J. Appl. Phys.* 119, 175104, 2016.

[6] R. Dettori, C. Melis, X. Cartoixà, R. Rurali, and L. Colombo, "Model for thermal conductivity in nanoporous silicon from atomistic simulations", *Phys. Rev. B* 91, 054305, 2015.

[7] X. Cartoixà, R. Dettori, C. Melis, L. Colombo, and R. Rurali, "Thermal transport in porous Si nanowires from approach-toequilibrium molecular dynamics calculations", *Appl. Phys. Lett.* 109, 013107, 2016.

[8] S. Plimpton, Fast parallel algorithms for short-range molecular dynamics, J. Comput. Phys. 117, 1, 1995.

[9] R. L. C. Vink, G. T. Barkema, W. F. van der Weg, and N. Mousseau, Fitting the Stillinger–Weber potential to amorphous silicon, J. Non-Cryst. Solids 282, 248 (2001).

[10] M. Verdier, D. Lacroix, S. Didenko, J-F. Robillard, E. Lampin, T-M. Bah and K. Termentzidis, , "Influence of amorphous layers on the thermal conductivity of phononic crystals", *Phys. Rev. B* 97, 115435, 2018.

[11] M. Verdier, D. Lacroix and K. Termentzidis, "Thernal Transport in two and three-dimensional nanowire networks", *Phys. Rev. B* 98, 155434,

A new DC-DC piezoelectric Converter

Mustapha TOUHAMI [1*], Benjamin POLLET[1,2], Ghislain DESPESSE [1] and François COSTA[2]
[1] CEA, LETI, Minatec Campus, Université Grenoble Alpes, 17 Rue des Martyrs, 38054 Grenoble, France
[2] Système et Application des Technologies de l'Information et de l'Energie, 61 avenue du président Wilson 94320 Cachan, France
[2]Université Paris Est Créteil, ESPE, place du 8 mai 1945, 93000 St Denis, France
*mustapha.touhami@cea.fr

***Abstract*— In this paper a new topology of step down DC-DC converter using a piezoelectric component as storage element is presented. DC-DC conversion process is based on electrical-mechanical-electrical transducer with Zero Voltage Switching (ZVS) for reducing losses. The experimental results in open loop operation are presented and it validates the converter operation principle for 30V to 10V at 2W power conversion.**

I. INTRODUCTION

Today DC-DC converters are widely used in various area of power supply and energy interfaces such as computer power supplies, mobile phones, lightning applications … etc. In these applications, high efficiency with best integration of converters are very important requirements. Several solutions are proposed in the literature to fulfill these requirements. These solutions include inductor based and switched capacitors based converters. The first converters are most commonly used, however, they are difficult to integrate on silicon. The second converters are easily integrated on silicon but they need high area [1]-[2]. To overcome these drawbacks, a new inductor-less DC-DC converter based on piezoelectric components with high efficiency is proposed in [3]. Piezoelectric components have small sizes, they are easily integrated on silicon. In addition, efficiency of this new converter can be improved from coupling and quality factor of piezoelectric components [4]. These converters are based on electrical-mechanical-electrical transductions. Indeed, during the resonance, piezoelectric component takes energy from the DC source and stored as mechanical deformation. After that, it transmits this stored energy to the DC output as load. A dead-time between each exchange energy phase allows operating in Zero Voltage Switch (ZVS) mode for minimal switching losses. Consequently, a further improvement of efficiency is reached [4]. Moreover, a variable resonant frequency can achieve large amplitude of oscillation.
In this paper, a new topology of DC-DC resonant converter is presented based on the same main process but dedicated for large input/output voltage ratio. This new topology enables to transfer power to the output at each constant voltage phases. Finally, it enables a higher power capability compared to the topology given in [5].

II. CIRCUIT DISCRIBTION

The topology of DC-DC converter is shown in Fig.1. This converter is composed of one piezoelectric component P, four diodes D_1, D_2, D_3, D_4 and two NMOS FET switches S_1 and S_2. At the resonant frequency of piezoelectric P, switches S_1 and S_2 are operating in ZVS mode in order to improve the efficiency. Indeed, in steady state resonance mode of piezoelectric P, the conversion is carried out with six phases:

- *Phase 1, $t \in [t_0, t_1]$:* S_1 and D_4 are turned on and S_2 is turned off. During this phase, piezoelectric P is connected between V_{in} and V_{out}. P takes electrical energy from V_{in} and stores it as mechanical deformation. This phase ends by turning off S_1. The energy acquired by the piezoelectric is controlled by t_1 duration.
- *Phase 2,$t \in [t_1, t_2]$:* All switches are turned off, the piezoelectric P is insulated. Its voltage V_p decreases from V_{in}-V_{out} to $-V_{out}$ as shown in Fig.2.This phase ends when V_p is equal to $-V_{out}$.
- *Phase 3, $t \in [t_2, t_3]$:* D_1 and D_4 are turned on, piezoelectric P is connected in reverse voltage to the output voltage to restore part of the mechanically stored energy. In this phase, ZVS mode for S_2 is ensured thanks to diodes operation. The phase ends at half of period.
- *Phase 4, $t \in [t_3, t_4]$:* All switches are turned off, the piezoelectric P is disconnected. During this phase, the voltage V_P increases from $-V_{out}$ to V_{out}.
- *Phase 5, $t \in [t_4, t_5]$:* S_2, D_2 and D_3 are turned on. The piezoelectric is connected to the output voltage to restore a second part its stored energy.
- *Phase 6, $t \in [t_5, t_6]$:* All switches are turned off. Piezoelectric P is insulated. Its voltage V_P increases from V_{out} to V_{in}-V_{out} (i.e. Fig.2). Time t_5 should be determined to ensure turn on S_1 in ZVS mode when the resonant period ended.

Basically, 1st, 3rd and 5th phases are used for storing and restoring the energy in piezoelectric P. The 2nd, 4th and 6th phases are used to apply the ZVS mode.

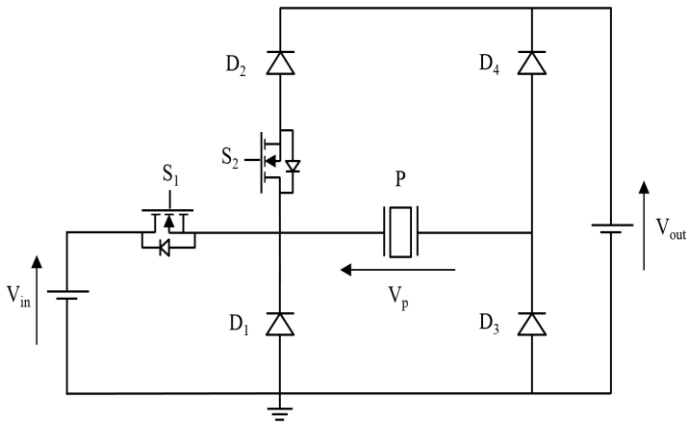

FIGURE 1. PROPOSED TOPOLOGY OF DC-DC CONVERTER

To ensure the proper operating cycle with high efficiency, the operation is governed by the balance equations of electrical charges and energy:

$$Q_{t_1\to t_2} + Q_{t_3\to t_4} + Q_{t_5\to t_6} = 0 \quad (1)$$

$$E_{t_0\to t_1} + E_{t_2\to t_3} + E_{t_4\to t_5} = 0 \quad (2)$$

And by the ZVS mode equations:

$$t = t_3 \quad then \quad V_P = -V_{out} \quad (3)$$

$$t = t_6 \quad then \quad V_P = V_{in} - V_{out} \quad (4)$$

$$V_{in} \geq 2 * V_{out} \quad (5)$$

Where $E_{t_0\to t_1}$ is the stored energy in the piezoelectric material during the 1st phase, $E_{t_2\to t_3}$ and $E_{t_4\to t_5}$ are the restored energy during the 3rd and the 5th phases respectively. $Q_{t_1\to t_2}$ is the accumulated algebraic charges in piezoelectric during the 1st phase. $Q_{t_3\to t_4}$ and $Q_{t_5\to t_6}$ are the transferred charges to V_{out} during the 4th and 6th phases respectively. Using theses equations and the equivalent electrical model of the piezoelectric material (see Fig. 3) enable to determine the closing duty cycle of S_1 and S_2. The electrical model is described in [4]-[5].

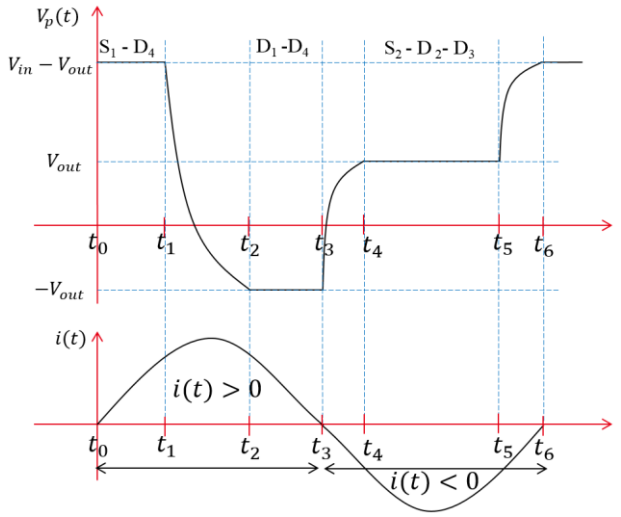

FIGURE 2. VOLTAGE AND INTERNAL CURRENT OF PIEZOELECTRIC

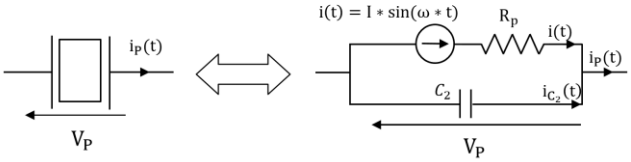

FIGURE 3. ELECTRICAL MODEL OF PIEZOELCTRIC

III. EXPERIMENTALE VALIDATION

A DC-DC converter circuit was designed and fabricated for experimental validation. The characteristics of used piezoelectric are given in [5]. The output load is represented by a bulk capacitor of 10µF in parallel with one resistance of 50Ω. These components are chosen in order to get 100mV of oscillation voltage and an electric power of 2W under 10V. For this operating point, the resonance frequency is 99.4 kHz.

Figure 4 presents the experimental results in open loop operation. The experimental waveforms match with the theoretical waveforms. The green curve in figure 4 represents the input current.

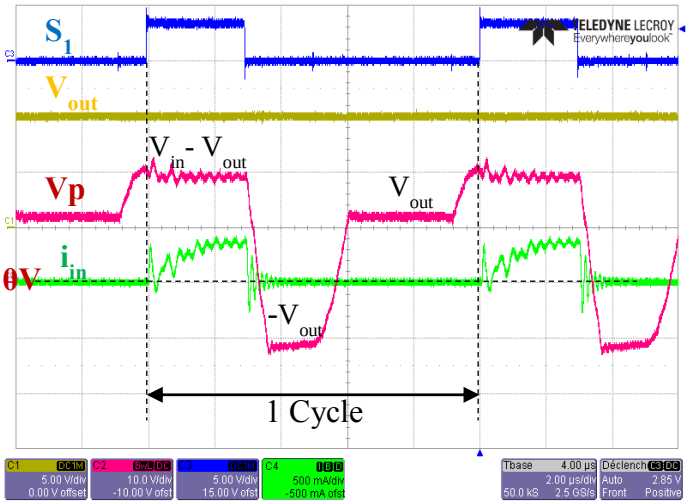

FIGURE 4. EXPERIMENTAL WAVES FORMES OF DC-DC CONVERTER

IV. CONCLUSION

This paper presents a new topology of DC-DC converter using piezoelectric device as storage element and maximizing the output current in the case of a high ratio between the input and output voltages. An experimental test in open loop validates the converter process for a 30V to 10V at 2W power conversion. This converter will be modeled and simulated in Matlab Simulink software to analyze the performances in closed loop at transient and steady state. Results will be presented in the final paper.

REFERENCES

[1] S. V. Cheong et al., "Inductorless DC-to-DC Converter with High Power Density", IEEE Trans. Ind. Electronics, vol. 41, no.2, 1994.

[2] S. Ghandour, G. Despesse and S. Basrour, "Design of a new MEMS DC/DC voltage step-down converter," *Proceedings of the 8th IEEE International NEWCAS Conference 2010*, Montreal, QC, 2010, pp. 105-108.

[3] Benjamin Pollet, Ghislain Despesse, François Costa. A new inductorless DC-DC piezoelectric flyback converter. ICIT IEEE 2018, Feb 2018, Lyon, France.

[4] D. Vasic and F. Costa, "Applications des éléments piézoélectriques en électronique de puissance," Tech. L'ingénieur Compos. Act. En Électronique Puissance Tech. L'ingénieur, pp. 235–24, 2011.

[5] Benjamin Pollet, Francois Costa, Ghislain Despesse. Inductor-less DC-DC converter using a piezoelectric transducer. 7 èmes Journées sur la Récupération et le stockage d'Energie, May 2017, Lyon, France. 2017.

Hybrid Ni-free 3D graphene/polyporphyrin with improved electron-transfer for light-harvesting

Martina USSIA [1,2*], Mario URSO[1,2], Maria MIRITELLO[2] & Sabrina Carola CARROCCIO[2]

[1] University of Catania, Department of Physics and Astronomy "Ettore Majorana", Via Santa Sofia 64, 95123, Catania, Italy

[2] CNR-IMM Catania Unit, Via Santa Sofia 64, 95123, Catania, Italy

*corresponding author: martina.ussia@ct.infn.it

***Abstract*— A novel hybrid material based on 3D graphene coupled with porphyrin-based polymer was formulated by using a time-saving procedure to remove Nickel from the final device. Specifically, a copolyformal was synthetized and characterized, serving also as protective coating during Nickel etching. The assembly between the organic semiconductor and graphene was achieved by the effective formation of non-covalent interactions at the material interface by a simple spin-coating deposition. The characterization of 3D graphene/copolyformal was assessed by using Scanning Electron Microscopy (SEM) and X-ray Photoelectron Spectroscopy (XPS). Photoluminescence (PL) analysis was used to investige the the electron-transfer process. Finally, we reported the calculation of copolyformal HOMO and LUMO energy levels measured by electrochemical techniques. The obtained results show potential in many application among which light harvesting.**

I. Introduction

Efficient production of clean and sustainable energy is the most formidable scientific challenge in the next half-century. In fact, the demand for energy is increasing with growing global population. Moreover, limited resources of fossil fuels and the climate changes due to combustive carbon emissions induced researchers to find environmental-friendly energy sources. In particular, sunlight is the most abundant and cleanest source of energy. Therefore, the utilization of solar energy has attracted much attention by the scientific community. In this context, porphyrins as organic semiconductors are particularly interesting due to appropriate LUMO and HOMO energy levels and very strong absorption of the Soret band in the 400–450 nm region, as well as the Q-bands in the 500–700 nm region. However, their application is strongly limited by a rapid electron-hole recombination process between LUMO and HOMO due to aggregation phenomena. To overcome this, we properly combined the copolyformal with a high surface area electron acceptor such as 3D graphene prepared by Chemical Vapor Deposition (CVD) on a Nickel foam substrate. Also, to improve the electron transfer process between copolyformal and graphene, we removed Nickel from our samples through a novel and time-saving method which preserved the 3D structure [1].

II. Results And Discussion

Random cyclic copolymer was synthesized by interfacial etherification reaction by using 5,10-bis(p-hydroxyphen- yl)-15,20-bis(p-dodecanoxyphenyl)porphyrin as porphyrin monomer and di(bisphenoxy-A)eicosane as co-monomer (Figure 1).

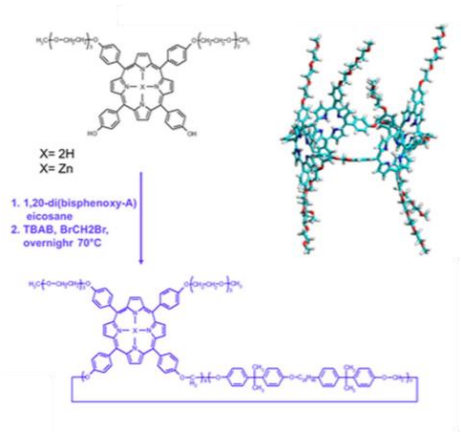

FIGURE 1. Preparation of the copolyformal

Nickel foam was used as 3D scaffold template for the CVD growth of 3D graphene. A suitable copolyformal deposition was obtained by spin-coating on the 3D graphene. Then, Nickel was removed for the first time via a one-step etching process in 1 M HCl where copolyformal served also as protective coating. This treatment avoided the collapse of the 3D structure. The schematic illustration of the Ni-free system fabrication is reported in Figure 2.

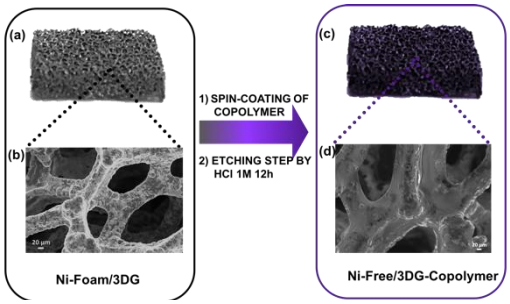

FIGURE 2. Preparation of the Ni-free copolyformal-graphene hybrid system.

To gain a better insight into the electronic properties of the copolyformal (i.e. HOMO and LUMO levels) cyclic voltammetry (CV) measurements were performed (Figure 3). From the high and irreversible reduction peak at -0.6 ± 0.2 V vs Fc/Fc^+ a LUMO energy level of -4.2 ± 0.2 eV was estimated as E_{LUMO} = -($E_{red.}$ vs Fc/Fc^+ + 4.8) eV. Since no oxidation peak of copolyformal was observed in the CV, to evaluate the HOMO energy level UV-Vis absorption measurement were performed, finding an energy gap of E_g = 2.2 eV. The HOMO energy level was finally determined as $E_{HOMO} = E_{LUMO} - E_g$ = -6.4 ± 0.2 eV.

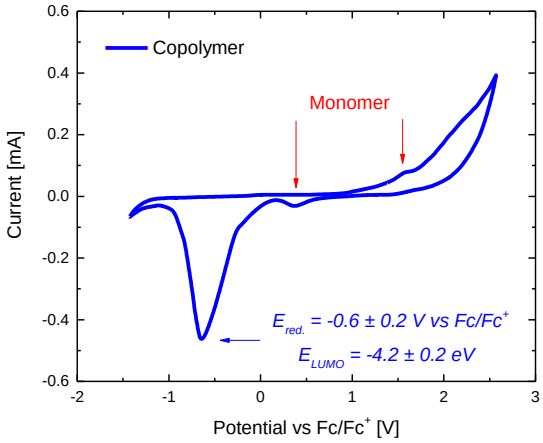

FIGURE 3. CYCLIC VOLTAMMETRY OF COPOLYFORMAL

In this work, graphene was used to avoid the recombination of the photogenerated electron-hole pair from LUMO to HOMO. In particular, we evaluated the influence of graphene on the optical emission of the copolyformal. Figure 4 compares the photoluminescence (PL) emission (325 nm excitation) of copolyformal coated Ni foam (Ni-foam/Copolymer), copolyformal coated 3D graphene on Nickel foam (Ni-Foam/3DG-Copolymer) and copolyformal coated Ni-free 3D graphene (Ni-free/3DG-Copolymer). In all cases the PL emission exhibits a broad band composed by two peaks centered at 660 and 720 nm, related to their $Q_X(0–0)$ and $Q_X(0–1)$ transitions respectively. However, it is evident a very effective quenching in the case of Ni-foam/3DG-Copolymer and a quasi-total disappearance of characteristic emission band for the Ni-Free/3DG-Copolymer with a slightly blue-shift of the signals. This key result validates that interactions between porphyrin aromatic moieties and graphene take place, allowing a remarkable electron transfer at the copolyformal interface. Different phenomena could justify the further PL quenching after nickel removal, such as the change in graphene electronic structure as well as an enhanced graphene π-delocalization after electron injection.

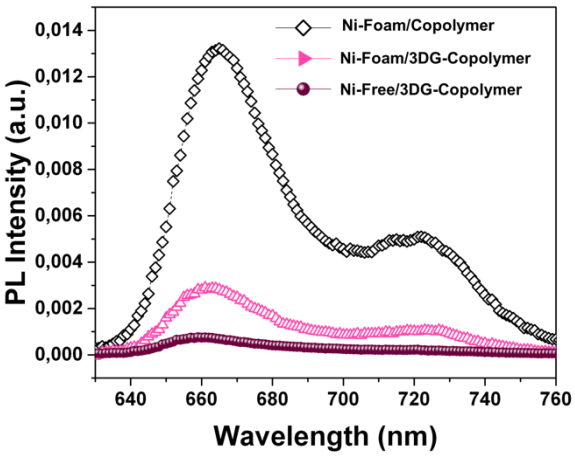

FIGURE 4. COMPARISON OF THE PHOTOLUMINESCENCE SPECTRA OF COPOLYFORMAL-BASED HYBRID SYSTEMS.

III. CONCLUSION

We reported a novel hybrid material based on 3D graphene and a porphyrin-based polymer (copolyformal) by using a time-saving procedure to remove Nickel. HOMO and LUMO energy levels of the copolyformal were measured, finding E_{HOMO}= -6.4 ± 0.2 eV, E_{LUMO}= -4.2 ± 0.2 eV and E_g= 2.2 eV. Photoluminescence measurements proved the superior electron transfer process from copolyformal to graphene, avoiding the recombination of the photogenerated electron-hole pairs from LUMO to HOMO. The obtained results are particularly promising for light harvesting.

REFERENCES

[1] M. Ussia, M. Urso, M. Miritello, E. Bruno, D. Vitalini, G. Condorelli, V. Privitera and S.C. Carroccio. Hybrid Nickel-free graphene/polyporphyrin photocatalyst: a time-saving formulation. Under review on *ACS Applied Materials & Interfaces*.

Optimize the output power of an electret kinetic energy harvester through adjusting the waiting time

Hanlu ZHANG, Shan FENG, Delong HE* and Jinbo BAI*

Laboratoire Mécanique des Sols, Structures et Matériaux (MSSMat), CNRS UMR 8579, CentraleSupélec, Université Paris-Saclay, 8-10 rue Joliot-Curie, 91190 Gif-sur-Yvette, France

*delong.he@centralesupelec.fr; jinbo.bai@centralesupelec.fr

***Abstract*—In this article, we investigated the influence of the waiting time on the output power of an electret kinetic energy harvester (electret-KEH) working in the contact-separation mode and with a high resistance load. By adjusting the time duration of the contact status, the average output power of the was improved from ~150 μW to ~197 μW. This work might be inspirational in designing electret-KEHs in accordance with their kinetic energy sources and load circuits.**

I. Introduction

Electret kinetic energy harvesters (electret-KEHs), which usually have compact structures in comparison with electromagnetic generators, are applicable in harvesting energy from weak low-frequency vibrations, especially in micro scales. Like piezoelectric kinetic energy harvesters (piezo-KEHs), electret-KEHs work based on electrostatic inductions. For piezo-KEH, the electrostatic induction is caused by the strain-induced dipole moment in piezoelectric materials, while for e-KEH it is caused by preserved electrostatic charges on the electret materials, both have capacitance characteristics. Electret-KEHs basically can be regarded as a voltage source connected in series with a variable capacitor [1]. If an electret-KEH is used to power a resistive load, a resistor-capacitor (RC) circuit is formed. And if the time constant of this RC circuit is too large, it will take considerable time to complete the charge transfer process which determines the output power of the electret-KEH. In this article, we reveal how the waiting time influences the output power of an electret-KEH connected with a high load resistance of 100 MΩ for the first time, which might be inspirational in designing electret-KEHs in accordance with their kinetic energy sources and load circuits.

II. Experiment and Theory

A. Material and structure of the electret-KEH

A piece of 4 cm × 4 cm sized 55 μm-thick skived polytetrafluoroethylene (PTFE) film was used as the electret material in the electret-KEH. Since PTFE has an excellent insulating property and the strongest attraction to electrons in known solid materials during contact-electrification [2], it naturally possesses some negative charges after fabrication. The cross-section structure of the electret-KEH is shown in FIGURE 1(A), where $-Q_E$ represents the effective preserved surface charge amount on the top side of the PTFE electret film, Q(t) is the time-dependent charge amount on the back electrode, and R is the load resistance in the external circuit. Conductive copper adhesive tape was attached on one side of the PTFE film to work as the back electrode, and a 4 cm × 4 cm sized alumina foil was used as the counter electrode.

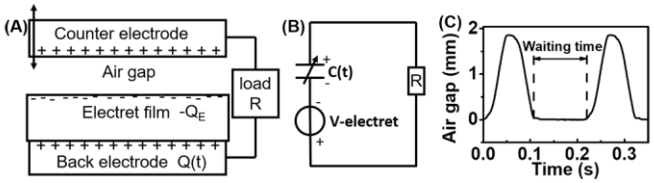

FIGURE 1. (A) Cross-section strucutre of the electret-KEH. (B) Equivalent circuit of the electret-KEH. (C) An example of the time-variable air gap curve during the test of the electret-KEH.

B. Working principle

FIGURE 1(B) shows the equivalent circuit of the electret-KEH, where the electret film and the back electrode is considered to form a constant voltage source if we consider Q_E and the thickness of the PTFE film as time-independent, while the electret film and the variable air gap is considered to form a variable capacitance C(t) between the two electrodes [1][3]. When the counter electrode is driven by a force to approach to or separate from the electret film, the variation in the air gap leads to the variation of C(t), resulting in charges transfer between the two electrodes through the load resistance to get electric equilibrium.

C. Measurement

In our measurements, the relative movement between the counter electrode and the electret film was controlled by a linear motor system (Afag Electro slider ES20-100 with LinMot servo drive and controlling software), and R is 100 MΩ from the oscilloscope (Wavejet 354A, Lecroy) with the high impedance probe for recording the output voltage of the electret-KEH. The transferred charge amount was measured with a Keithley 6514 electrometer.

D. Waiting time

To output more energy, the electret-KEH need to transfer more charge during one contact-separation cycle. For an RC series circuit, the charge or discharge of the capacitor takes time depending on the time constant ($\tau=R\times C$) of this circuit. With a larger τ, the charge or discharge takes longer time. For the electret-KEH, C(t) reaches the maximum when the counter electrode fully contacts the electret film due to the elimination of the air gap. Therefore, it takes a longer time for the electret-KEH to complete the charge transfer when the air gap is 0 than larger air gap. We call the duration of that air gap is 0 in one

contact-separation cycle as the waiting time. FIGURE 1(C) is a representative air gap-time curve with a waiting time of 112 ms. To investigate the influence of waiting time on the output voltage and power of the electret-KEH, the same maximum air gap of 1.82 mm, same motion speed, acceleration, and deceleration were used during measurements unless otherwise specified in following results.

III. Results and Discussion

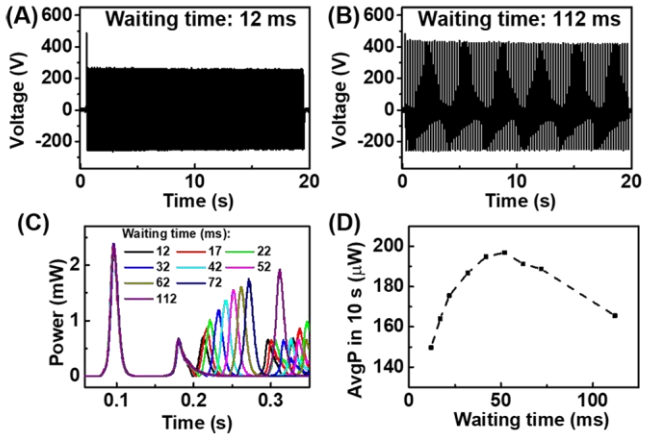

FIGURE 2. The output voltage of the electret-KEH measured with a waiting time of (A) 12 ms, and (B) 112 ms, respectively. (C) The time-dependent output power of the electret-KEH measured with the different waiting time. (D) The average output power (AvgP) of the electret-KEH in 10 seconds with different waiting time

As shown in FIGURE 2, positive voltage peaks appear when the counter electrode separates from the electret film and negative voltage peaks appear when it approaches the electret film. With waiting time of 12 ms, except that the first positive voltage peak is high as near 480 V, all other positive voltage peaks have a stable amplitude of about 260 V, and negative voltage peaks have a stable amplitude of about -250 V during measurements in 20 seconds. While with waiting time of 112 ms, the first positive voltage peak is also near 480 V, other positive voltage peaks slightly decrease from about 440 V to about 420 V, and negative voltage peaks have a stable amplitude of about -250 V.

The output power of the electret-KEH was calculated from the measured output voltage simply by Ohm's law. As shown in FIGURE 2(C), with waiting time from 12 to 112 ms, all the first power peaks are almost the same since they all come from the first separation of the counter electrode from the electret film. While for the second power peak coming from the first contact of the counter electrode with the PTFE film after the separation, peak values are almost the same but the shape of the peak changes with waiting time, meaning the transferred charge amount is influenced by the waiting time. Therefore, the amplitude of the third power peak corresponding to the second separation shows a monotone increasing trend with increasing waiting time. FIGURE 2(D) shows the average output power (AvgP) of the electret-KEH in 10 seconds, with the different waiting time. With the waiting time increasing from 12 ms to 52 ms, the AvgP increases from ~150 μW to ~197 μW. With the waiting time further increasing to 112 ms, the AvgP decreases to ~165 μW. This is because that though longer waiting time is beneficial for the KEH to transfer more charge and therefore convert more energy into electricity in per contact-separation cycle, it also decreases the number of the contact-separation cycle during the given period.

To verify the that the variation of the output power is not caused by the variation in the surface charge amount on the PTFE film, we recorded the transferred charge amount of the electret-KEH before and after all the voltage measurements. In these measurements, the maximum air gap was set at 20 mm, the waiting time was set as 1s, and the maximum air gap was also kept for 1s in one contact-separation cycle. With these conditions, the transferred charge amount approximates the charge amount on the electret film [4]. As shown in FIGURE 3, there is no apparent change in the charge amount, excluding the influence of the surface charge amount on the PTFE film.

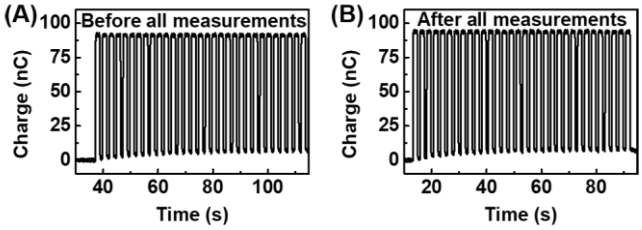

FIGURE 3. The transferred charge amount of the electret-KEH (A)before and (B) after all measurements

IV. Conclusion

In summary, in the case that the electret-KEH is connected to a high resistance load, the waiting time has an influence on the output power of the KEH. If the waiting time is too short, the charge transfer during the contact status is far from complete, resulting in lower output voltage and power than those with the appropriate waiting time. If the waiting time is too long, the input kinetic power is too low, also leading to the lower output voltage and power than those with the appropriate waiting time.

Acknowledgment

Hanlu Zhang and Shan Feng acknowledge the financial support from the China Scholarship Council (CSC) during their study in France. Authors also give thanks to Mr. Éric Perrin for his help in setting up the linear motor system.

References

[1] S. Boisseau, G. Despesse, T. Ricart, E. Defay, and A. Sylvestre, "Cantilever-based electret energy harvesters", Smart Mater. Struct., 20 (2011) 105013.

[2] Z.L. Wang, "Triboelectric Nanogenerators as New Energy Technology for Self-Powered Systems and as Active Mechanical and Chemical Sensors", ACS Nano, 7 (2013) 9533-9557.

[3] Y. Lu, E. O'Riordan, F. Cottone, S. Boisseau, D. Galayko, E. Blokhina, F. Marty, P. Basset, "A batch-fabricated electret-biased wideband MEMS vibration energy harvester with frequency-up conversion behavior powering a UHF wireless sensor node", J. Micromech. Microeng., 26 (2016) 124004.

[4] Y. Zi, S. Niu, J. Wang, Z. Wen, W. Tang, Z.L. Wang, "Standards and figure-of-merits for quantifying the performance of triboelectric nanogenerators", Nat. Commun., 6 (2015) 8376.